**Mechatronics Methods for Mitigating Undesirable Effects of Pre-motion Friction in Nanopositioning Stages with Mechanical Bearings**

by

Xin Dong

A dissertation submitted in partial fulfillment
of the requirements for the degree of
Doctor of Philosophy
(Mechanical Engineering)
in the University of Michigan
2020

Doctoral Committee:

Associate Professor Chinedum E. Okwudire, Chair
Assistant Professor Al-Thaddeus Avestruz
Associate Professor Shorya Awtar
Professor Kenn Oldham

Xin Dong

terrydx@umich.edu

ORCID iD: 0000-0001-7872-6846

## DEDICATION

*To my parents and Yunlu who always support me.*

## ACKNOWLEDGEMENTS

I did not know that I would be pursuing a doctorate degree when I first joined the University of Michigan as a master's student in 2014. While working towards my M.S. degree, I had the opportunity of working on an independent research project which brought me into this exciting and challenging field. The more I dug into the topic, the more I realized its importance and great potential, which eventually hooked me into the Ph.D. program. Looking back the past five and half years, I can certainly tell this is a wonderful journey that I really enjoyed. There are so many people who have helped me, and I would like to express my sincerely gratitude to all of them.

Firstly, I want to thank my advisor, Professor Chinedum Okwudire, who has given me the opportunity and provided excellent guidance throughout my entire Ph.D. study. Without him, I would not be able to accomplish what I have so far. When I arrived at the school in 2014, I started working with him on this research project. With his patient guidance, valuable feedback and encouragement, the project became funded which made my Ph.D. possible. I am always fascinated by his brilliant ideas, and the right amount of balance between academic advancement and industrial practicality. By always keeping these two things on my minds, the works presented in this dissertation have been appreciated by people from both academia and industry. Our relationship has grown far beyond research. From him, I learned the optimistic attitude and how to find the balance between work, life and family. I am truly grateful for the past 5 years we have been working together.

I also want to thank my committee members: Professor Al-Thaddeus Avestruz, Professor Shorya Awtar and Professor Kenn Oldham, for their valuable feedback and guidance. Their constructive inputs have greatly improved the quality of my research. Professor Al-Thaddeus Avestruz provided great ideas on improving the current prototype designs. The valuable suggestions from Professor Shorya Awtar and Professor Kenn Oldham have helped me combining and presenting different pieces of my works, into this coherent dissertation.

I want to thank my collaborators, Jiamin Wang and Professor Oumar Barry from Virginia Tech, for their insight knowledge on the nonlinear analysis. Their hard work and constructive

feedback have complemented my research from the theoretical aspect. I would also like to express my thanks to Dongwoo Kang from Korea Institute of Machinery & Materials (KIMM). I truly enjoyed the collaboration with him.

I want to thank my former lab mate Deokkyun Yoon for his supports and inputs to my research. A lot of the ideas in this dissertation originated from our discussions. Many thanks to other lab members that I have interacted with during my time at the Smart and Sustainable Automation Lab: Molong Duan, Jihyun Lee, Keval Ramani, Nosa Edoimioya, Wami Ogunbi, Xiang Lu, Xingjian Liu, Bowen Zeng, Ding Zhang, Xiaowen Zhang.

Finally, I would like to thank my parents and Yunlu for their unwavering support.

## TABLE OF CONTENTS

## LIST OF TABLES

## LIST OF FIGURES

## LIST OF APPENDICES

## ABSTRACT

Nanopositioning (NP) stages are used to for precise positioning in a wide range of nanotech processes, ranging from substrate patterning to micro additive manufacturing. They are often used for point-to-point (P2P) motions, where the stage is commanded to travel to and settle within a pre-specified window of the target position, and for tracking motions, where the stage is commanded to follow a reference trajectory. The settling time, in-position stability and tracking accuracy of NP stages directly affects the productivity and quality of the associated processes or manufactured products.

NP stages can be constructed using flexure, fluidic, magnetic or mechanical bearings (i.e., sliding and, especially, rolling-element bearings). Of these choices, mechanical bearings are the most cost-effective, and are currently the only commercially viable option for a growing number of NP applications that must be performed in high vacuum environments. However, mechanical-bearing-guided NP stages experience nonlinear pre-motion (i.e., pre-sliding/pre-rolling) friction which adversely affects their precision and speed. Control-based compensation methods, commonly used to address this problem, often suffer from poor robustness and limited practicality due to the complexity and extreme variability of friction dynamics at the micro scale. Therefore, this dissertation proposes three novel mechatronics methods, featuring a combination of mechanical design and control strategy, as more effective and robust solutions to mitigate the undesirable effects of pre-motion friction.

The first approach is vibration assisted nanopositioning (VAN), which utilizes high frequency vibration (i.e., dither) to mitigate the low speed (slow settling) of mechanical-bearing-guided NP stages during P2P motions. VAN allows the use of dither to mitigate pre-motion friction while maintaining nanometer-level positioning precision. P2P positioning experiments on an in-house built VAN stage demonstrates up to 66% reductions in the settling time, compared to a conventional mechanical bearing NP stage.

A major shortcoming of VAN is that it increases the cost of NP stages. To address this limitation, a friction isolator (FI) is proposed as a simple and more cost-effective method for

mitigating pre-motion friction. The idea of FI is to connect the mechanical bearing to the NP stage using a joint that is very compliant in the motion direction, thus effectively isolating the stage from bearing friction. P2P positioning tests on a NP stage equipped with FI prototypes demonstrate up to 84% reductions in the settling time. The introduction of FI also enables accurate and robust reductions of motion errors during circular tracking tests, using feedforward compensation with a simple friction model.

One pitfall of FI is that it causes increased error of the stage during in position. Therefore, a semi-active isolator (SAI) is proposed to mitigate the slow settling problem using the FI, while maintaining the benefits of friction on in-position stability. The proposed SAI, which connects the bearing and NP stage, is equipped with solenoids to switch its stiffness from low, during settling, to high once the stage gets into position. P2P experiments demonstrate up to 81% improvements in the settling time without sacrificing in-position stability.

The proposed mechatronics methods are compared and FI stands out as a result of its simplicity, cost-effectiveness and robust performance. Therefore, the influence of design parameters on the effectiveness of FI are investigated to provide design guidelines. It is recommended that the FI should be designed with the smallest stiffness in the motion direction, while satisfying other requirements such as in-position stability and off-axis rigidity.

# Chapter 1

# Background and Motivation

## 1.1 The need for more precise, faster and cheaper nanopositioning stages

The National Nanotechnology Initiative defines nanotechnology as science, engineering, and technology conducted at the nanoscale [1]; it comprises technologies that create and use materials, devices and systems through the manipulation of matter at scales of less than 100 nm [2]. It is believed to be one of the most promising areas of technological development, and among the most likely to deliver substantial economic and societal benefits to the U.S. in the 21st century [3].

Nanopositioning (NP) stages are mechanical positioning devices capable of developing displacements with nanometer-scale resolution [4]. They fall under the market category of nanodevices and nanomachines, which is expected to grow from $736.1 million in 2018 to $1.3 billion in 2023 and then to $2.7 billion in 2028 [5]. NP stages are indispensable in a wide range of nanotech processes, such as substrate patterning, scanning probe microscopy, spectroscopy, MEMS inspection, micro/nano machining, micro/nano 3D printing, optical fiber alignment, data storage, mapping of photovoltaic cells, to mention a few [6]-[12]. Because they directly control the relative motion between tool (e.g., laser beam, optics and probe) and workpiece (e.g., silicon wafer, flat panel display and substrate), the positioning accuracy and speed of NP stages determine the quality and productivity of the associated processes or manufactured products [11][13].

NP stages are mainly used for two types of motions: point-to-point positioning motions and tracking motions. In point-to-point motions, the stage is commanded to travel to and stay at a desired position as fast as possible [13][14]. The manufacturing or metrology-related nanotech process is then performed after the stage settles within a pre-specified vicinity (also known as the settling window) of the target position. Figure 1.1 shows an example of the semiconductor inspection system where the NP stage moves the wafer to the focused area of the electron beam one die at a time through point-to-point motions. The pattern on the die is then captured and

compared to the pattern obtained from the adjacent die for defect detection [15]. The time taken for the stage to settle within the pre-defined window after each point-to-point motion is crucial to the throughput of the machine. Note that the NP stage still displays certain noise even when it is commanded to stay stationary; this is often known as in-position stability or jitter [14]. The level of in-position error also plays an important role on the quality of the processes. For instance, relative motion between the electron beam and a patterned die, while the stage stays in-position, affects the minimum size of the identifiable defect.

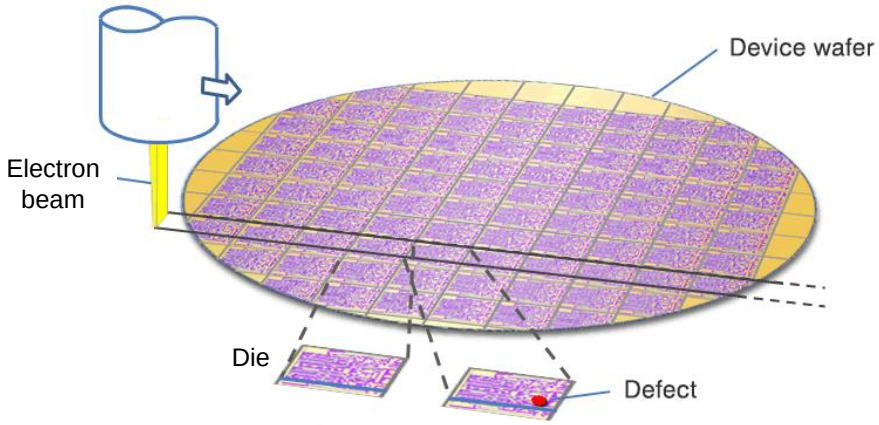


Figure 1.1 Principles of wafer defect inspection system [15]. Note that the process is carried out in high vacuum environment.

During tracking motions, the stage is commanded to follow a reference trajectory as closely as possible. According to ISO 230 [16], circular tracking tests are typically used to validate the accuracy of ultra-precision machine tools. Alternatively, triangular scanning commands are also used in a wide range of advanced manufacturing and metrology-related processes, such as scanning probe microscopy [17] and semiconductor photolithography [18]. As shown in Figure 1.2, during photolithography, the reticle stage that carries the photomask and the wafer stage that carries the silicon wafer are operated synchronously to scan the entire area [19]. As the process is repeated tens of times, it is critical that the silicon wafer and photomask are aligned with great precision each time. Due to the limited ability of motion controller, the actual position of the NP stage may deviate from the reference command during tracking motions and the difference is called (position) tracking error. The peak error (i.e., largest in absolute value) is often used to evaluate the accuracy of the machines. For instance, in micro milling, whether the part is within the desired

tolerance is determined by the peak error. In addition, the root-mean-square (RMS) value of the tracking errors during the entire motion is also widely adopted to measure the quality of the manufacturing processes [20].

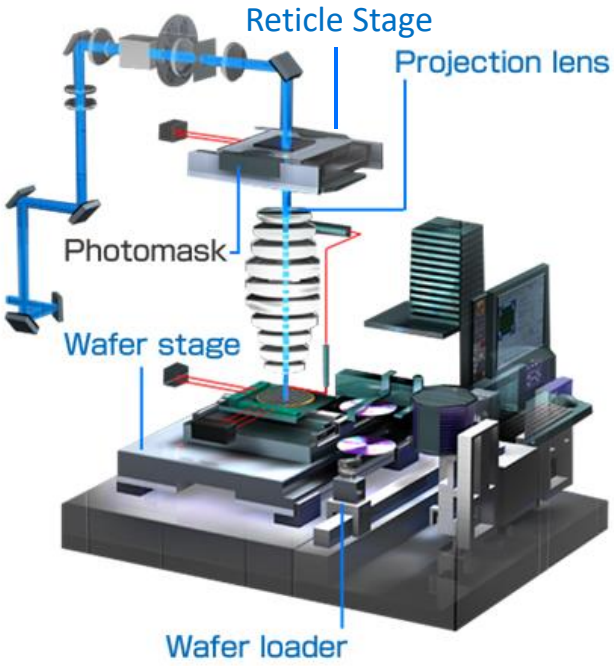


Figure 1.2 Semiconductor lithography system showing reticle stage, wafer stage and wafer loader [18].

Precision requirements for NP stages are becoming more stringent, with many now comfortably in the sub-micrometer range, and others even tighter, down to single-digit nanometer levels [21]. At the same time, there is a push for higher throughput and lower cost of NP stages. The semiconductor industry, for instance, has adopted the mantra, “smaller, faster, cheaper” to highlight its emphasis on all three criteria [22]. Culpepper and Anderson have remarked that better cost-performance characteristics will be needed to improve the commercial feasibility of emerging nanoscale technologies [23]. Physik Instrumente, a leading manufacturer of NP stages, has emphasized that, because “time is money,” the nanotech industry “needs not just better nanometers but faster nanometers.” [24].

## 1.2 Classification of nanopositioning stages

NP stages can be grouped into four broad categories based on the types of bearings they use: 1) flexure, 2) magnetic, 3) fluidic, and 4) mechanical bearing NP stages.

A flexure-based NP stage consists of a moving platform that is suspended by several compliant mechanisms, or flexures [4][25]. Flexure-based stages are compact, low cost and friction-free, allowing them to be extremely precise [26]. However, they often have small payload and short stroke (typically < 1 mm) due to their inherent flexure elements [25][27]. Increasing their payload or motion range lowers their fundamental natural frequency or significantly enlarges the footprint of the system, thereby reducing their speed accordingly [28][29]. Therefore, for long range NP applications (e.g., lithography, optical inspection, wafer inspection and micro machining), the choice is generally between magnetic, fluidic and mechanical bearings.

In magnetic bearing NP stages, the motion platform is levitated by a set of embedded planar motors [7][19]. This guideway-free architecture allows the stage to move freely in the work space with all six degree-of-freedoms [30]. Magnetic bearing NP stages are friction-free, allowing them to be very fast and precise [31]. However, the need of actuation and control-related hardware to cover the entire motion area and the demand of a high performance forced cooling system to avoid thermal issues make them extremely expensive. Therefore, magnetic bearing NP stages are currently only used in the highest end, multi-million-dollar systems for which their cost is justifiable, such as the wafer scanners for photolithography [20][32]. They have not gained commercial acceptance for most other applications of NP stages due to their high costs and complexities.

Fluidic bearings can either be hydrostatic or aerostatic [11]. Hydrostatic bearings employ pressurized oil to reduce the friction between sliding surfaces, providing desirable friction characteristics with excellent damping [33]. However, they are not suitable for cleanroom environments, where many NP stages are used [34][35], because oil can easily create contaminants as a result of leakage. Aerostatic (or air) bearings feed a thin film of pressurized air between the sliding surfaces such that the resulting friction is negligible [11][36]. Furthermore, they are cleanroom-compatible and are relatively cheaper than magnetic bearings [37]. However, aerostatic bearings are not vacuum compatible, which makes them unsuitable for the growing number of next-generation NP applications that must be performed in high or ultra-high vacuum, e.g., E-

beam inspection, scanning electron microscopy, spectroscopy and focused ion beam technology [38]-[40].

Mechanical bearings (i.e., sliding and, especially, rolling-element bearings) are the most cost-effective of the bearing types – see Figure 1.3 for a few examples. Sliding bearings suffer from large friction and wear, therefore, are not typically used for NP applications. Rolling-element bearings with re-circulating or stationary balls (or rollers) inside the carriages are commonly used in NP stages [11]. They can provide accuracies comparable to air bearings for motion ranges up to a few hundred millimeters (see Figure 1.4). When lubricated with small amounts of low vapor pressure grease, mechanical-bearing-guided NP stages can be used in cleanroom environments [41]. Therefore, they are very attractive as a lower cost alternative to aerostatic bearing stages for a wide range of NP applications. Moreover, they are currently the only commercially viable alternative to magnetic bearing stages for majority of the NP applications that require vacuum compatibility, such as optics polishing, E-beam inspection, scanning electron microscopy, and focused ion beam technology [38]-[40]. However, mechanical bearing NP stages experience nonlinear friction which adversely affects both their positioning precision and speed, as explained in Section 1.3.

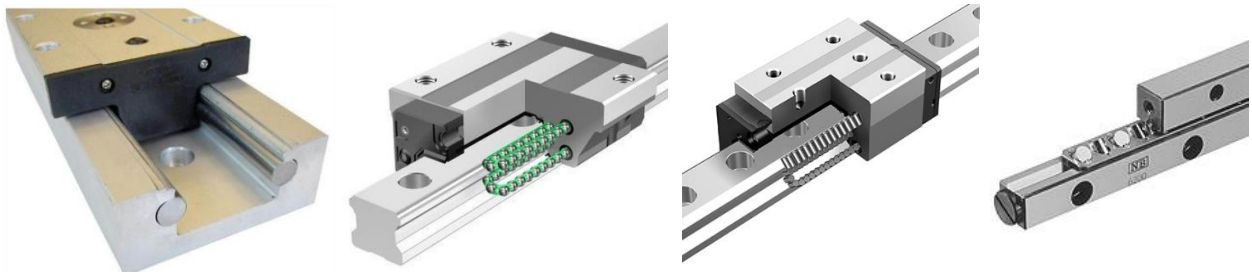

(a) (b) (c) (d)

Figure 1.3 (a) Sliding bearing [42], (b) re-circulating ball bearing [43], (c) re-circulating roller guide [43], and (d) cross roller bearing [44].

Figure 1.4 Planar NP stage guided by mechanical bearings [45].

## 1.3 Pre-motion friction and its adverse effects on mechanical-bearing-guided nanopositioning stages

Friction behavior of mechanical bearings can be divided into two regimes: the macro- and the micro-displacement regimes [13][46]-[56]. They are sometimes referred to as the gross motion and pre-motion friction regimes, respectively, where "motion" implies rolling and/or sliding [13][51][54][55]. In the gross motion regime, friction is a function of the relative velocity between the two objects moving against each other [52][56]-[58]. Variations of the gross motion friction affect the precision of the mechanical bearing stages [59]. However, the high bandwidth controller, commonly used to control the NP stage, is capable of suppressing the slow change of frictional disturbance, delivering relatively high performance.

On the other hand, in the pre-motion regime, friction is primarily a function of displacement rather than velocity. Accordingly, pre-motion friction behaves as a nonlinear spring due to elastoplastic deformations and micro-slip of the rolling elements and seals/wipers [13][48][50]-[52][56]. Dahl [46][47] was the first to describe this phenomenon using a mathematical model given by

$$\frac{dF_f}{dx} = k_\sigma \left(1 - \frac{F_f}{F_C} \operatorname{sgn} \dot{x}\right)^{\upsilon} \tag{1.1}$$

where $F_f$ represents the force of friction and $x$ is the relative displacement between the bearing surfaces; $k_\sigma$ is the initial contact stiffness of pre-motion friction, and $F_C$ is a measure of the Coulomb force; $\upsilon$ is a shape factor which is often set equal to one. As seen in Figure 1.5, the Dahl model predicts the smooth transitions of bearing friction from pre-motion to gross motion regime [54][60][61]. It also captures the nonlinear hysteretic behavior that is well-known to characterize pre-motion friction [51][52].

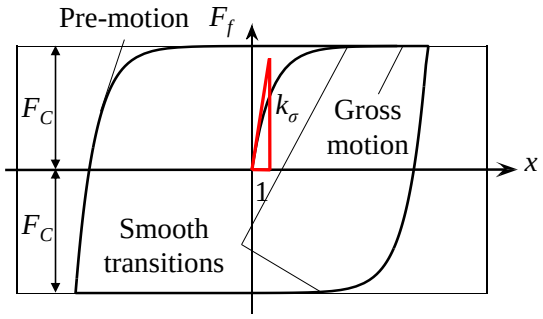


Figure 1.5 Dahl friction model showing smooth transitions of bearing friction from pre-motion to gross motion regime [60][61].

Figure 1.6 illustrates the schematic of a typical mechanical-bearing-guided NP stage, in which a bearing is rigidly attached to the moving table. Before gross motion begins, the stage experiences pre-motion friction due to its inherent rolling-elements. According to the Dahl model and Eq. (1.1), pre-motion friction can be modeled as a nonlinear spring of stiffness $dF_f/dx = k_f$, connecting the table to the ground [48]-[50][55][56]. Referring to Figure 1.5, at the start of motion (or after motion reversals), $k_f = k_\sigma$ is initially very large. As more servo force is applied to counteract friction, $k_f$ rapidly reduces and eventually becomes zero, allowing gross motion of the stage [46][49][52]. This leads to a highly nonlinear time-varying system which is very hard to control. In particular, PID-type feedback controllers (e.g., PID, P-PI, etc.), commonly used in practice, often have difficulties in overcoming the initially large value of frictional stiffness $k_f = k_\sigma$, leading to significantly worsened speed and precision. [48][49][62]-[65].

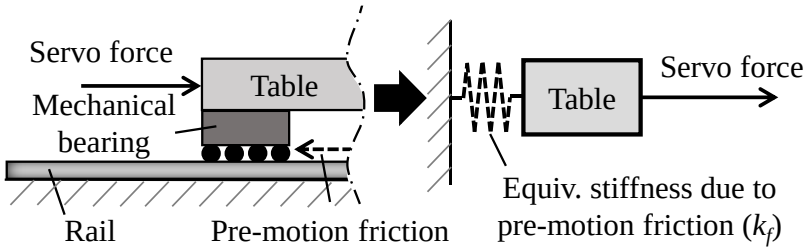


Figure 1.6 Schematic of a conventional mechanical-bearing-guided NP stage under the influence of pre-motion friction.

During point-to-point positioning, pre-motion friction dominates with its large stiffness as the stage approaches the target position, leading to very sluggish settling as seen from Figure 1.7(a) [13][53][54][61]. As a result, the mechanical-bearing-guided NP stage typically takes 5-10 times longer to settle with nanometer-level precision, compared to an equivalent frictionless stage [54][61]. Such long settling times severely hamper the throughput of the manufacturing processes for which the NP stages are used. During tracking motions, large tracking errors (e.g., glitches) often occur as the feedback controller having difficulties to compensate the large frictional stiffness at motion reversals – see Figure 1.7(b) for an example of quadrant glitch during circular tracking motion [55][56][66]-[68]. Accordingly, the tracking accuracy of the machine is severely jeopardized, leading to products with poor quality. These undesirable effects of pre-motion friction significantly jeopardize the performance of the mechanical-bearing-guided NP stages.

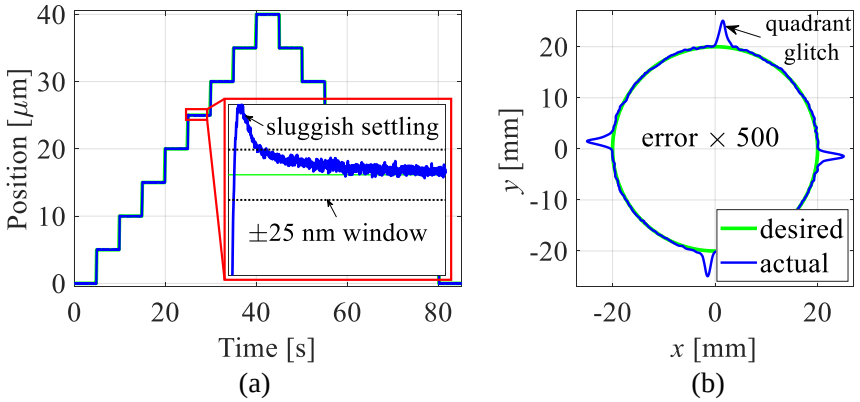


Figure 1.7 (a) Sluggish settling behavior during point-to-point motion, and (b) quadrant glitch during circular tracking motion using a conventional mechanical-bearing-guided NP stage.

## 1.4 Outline of dissertation

Motivated by the aforementioned challenges faced by the presence of pre-motion friction, this dissertation proposes three practical mechatronics solutions to mitigate the undesirable effects of pre-motion friction, thus, improving the performance of mechanical-bearing-guided nanopositioning (NP) stages during point-to-point positioning and tracking motions. Specifically, each method is evaluated experimentally with respect to its performance (i.e., settling time, in-position stability and tracking accuracy) and practicality (i.e., cost-effectiveness, simplicity and robustness), as described in Figure 1.8.

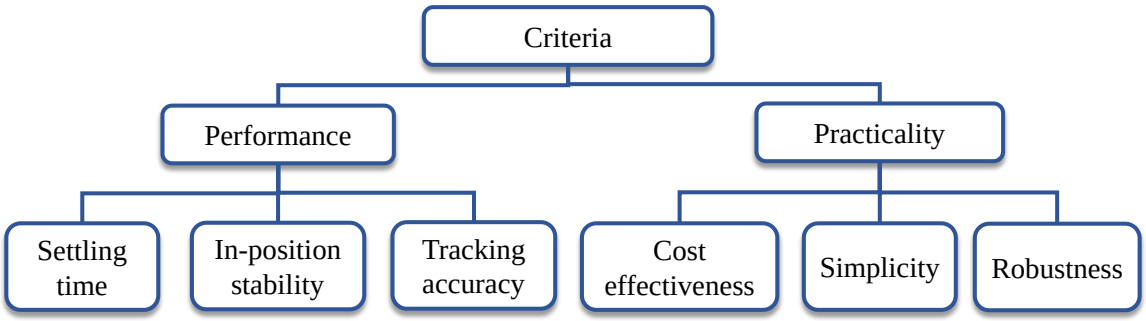


Figure 1.8 Evaluation criteria of the proposed methods.

In Chapter 2, a literature review on the state-of-the-art friction mitigation methods is carried out to illustrate the deficiencies of existing control-based and mechatronics-based friction compensation approaches regarding the evaluation criteria. In Chapter 3, vibration assisted nanopositioning (VAN) is proposed to improve the settling time of mechanical-bearing-guided NP stage using high frequency vibration (i.e., dither). Different from the traditional dithering techniques which jeopardize the motion precision by directly vibrating the stage or guideway, VAN is able to reduce settling time while maintaining nanometer-level positioning precision. In Chapter 4, friction isolator (FI) is proposed as a simple, low cost and robust method to mitigate the undesirable effects of pre-motion friction. FI makes a feedback controller to deliver high performance and robustness without the need for very high gains, leading to significantly reduced settling times during point-to-point motions. Moreover, the addition of FI enables accurate and robust feedforward compensation of pre-motion friction using a simple model, resulting in large

and robust reductions of errors during tracking motions. In Chapter 5, semi-active isolator (SAI) is proposed to mitigate the undesirable effects of pre-motion friction during motion transients using the FI, while maintaining the benefits of bearing friction on in-position stability. The stage with the SAI simultaneously achieves fast settling and excellent in-position stability. These three mechatronics methods are compared in Chapter 6 and the FI rises to the top of the list, because of its excellent performance and practicality. The influence of design parameters on the effectiveness of FI is then investigated to provide design guidelines for FI. This is followed by conclusions and future work in Chapter 7. Although the proposed methods are discussed in the context of linear NP stages in this dissertation, they can be broadly applied to other precision motion applications. For instance, in the Appendix, an implementation of a rotary FI on the high precision roll-to-roll machine to mitigate the undesirable effects of friction during constant velocity tracking motions is demonstrated.

# Chapter 2

# Literature Review

Armstrong-Hélouvry et al. have conducted an exhaustive survey of methods for mitigating friction in machines [49]. Their survey includes 280 academic articles as well as inputs from engineers with 23 different companies in Europe, Japan and the U.S., and several government laboratories. The literature review of friction mitigating techniques presented in this chapter draws extensively from their work, and also from a large number of more-recent articles, especially on the compensation of pre-motion friction in mechanical-bearing-guided nanopositioning (NP) stages. Avoidance techniques to reduce the level of friction are discussed in Section 2.1. In Section 2.2, control-based compensation approaches for mitigating friction are presented. These methods often suffer from robustness problems due to the nonlinear changes and large variations of on machine friction dynamics, especially at the micro scale. Therefore, mechatronics-based approaches (i.e., design modification combined with control strategy), which are generally more robust, are summarized in Section 2.3. However, significant increases in cost and complexity are generally associated with existing mechatronic-based methods. The key contributions of this dissertation in developing low cost mechatronics solutions for mitigating pre-motion friction in NP stages are then discussed in Section 2.4.

## 2.1 Friction avoidance techniques

As shown in Figure 2.1, avoidance and compensation are the two primary ways of mitigating the undesirable effects of friction [49]. The idea of friction avoidance is to physically reduce the level of friction experienced by the mechanical bearings of the NP stages. Examples of friction avoidance techniques include bearing/lubricant selection and the reduction of the number of rubbing mechanical elements. The use of contactless (direct-drive) motors, cross roller bearings and small amounts of high quality grease are some ways of trying to avoid friction in NP stages [11][49]. Reducing the size of re-circulating balls [69] and putting cage around the individual ball

[70] are other examples that are used by precision bearing manufacturers. Friction avoidance is the first recourse in industrial practice and NP stage manufacturers often extensively exploit the available avoidance techniques, subject to cost and other constraints [49].

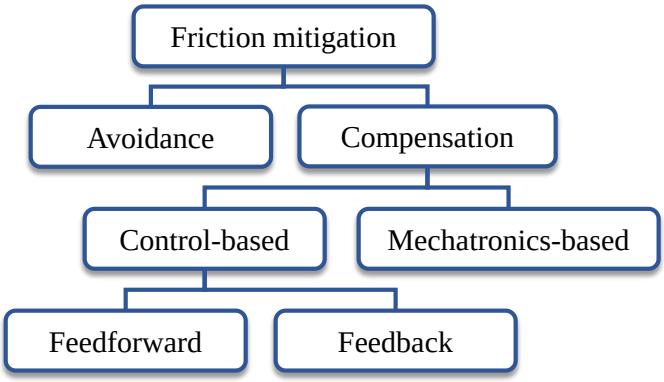


Figure 2.1 Friction mitigation methods.

## 2.2 Control-based compensation approaches

When friction cannot be completely avoided, as in mechanical-bearing-guided NP stages, whatever is remaining has to be compensated. The undesirable effects of friction can be mitigated using purely control-based or mechatronics-based compensation approaches. The idea of control-based compensation methods, which are widely studied in the literature, is to supply an equal and opposite force, through a control system of the NP stage, to cancel out the effects of friction. It can be executed in the feedforward or feedback loop of the controller.

In feedforward compensation, the friction force experienced by a stage is predicted and cancelled out preemptively using a model of friction combined with the knowledge of the reference trajectories (e.g., position and velocity commands) applied to the stage [14][56][71]-[74]. To be effective, the friction model must be sufficiently accurate; and to be practical, the model should have a minimal number of parameters that can be identified easily without the need for frequent re-calibration. The problem is that simple models of pre-motion friction often do not have sufficient accuracy, so, complex models are needed to achieve accurate compensation of pre-motion friction [55][75]. As reported in several studies, tracking accuracy can be greatly improved using feedforward friction compensation with advanced (complex) models of pre-motion friction [55][56][66][75][76].

However, friction, particularly in the pre-motion regime, is very temperamental [14][55]. For example, Bucci et al., report an order of magnitude difference in the identified initial frictional stiffness (i.e., $k_\sigma$ in Eq. (1.1)) of the Dahl model using a NP stage within its 25 mm travel range [54]. Moreover, drastic changes in friction dynamics are also observed as the machine continuously operates through its life time [77]. Feedforward compensation methods using both simple and complex models of pre-motion friction are not robust to these changes in on-machine friction dynamics [55][78]. Thus, they need frequent re-calibration to maintain their effectiveness, which hampers their practicality. Several methods have been proposed in the literature for improving the robustness of model-based feedforward friction compensation methods through parameter adaptations [79]-[81]. However, the convergence of the adaptation schemes is often unreliable and slow because the identification signals are not rich (or persistent) enough [49][81].

Another major problem with feedforward friction compensation approaches is related to their dependence on the desired (i.e., reference) velocity to predict friction. When a stage is trying to settle to a target position, the desired velocity is often zero at the settling region, even though the actual velocity is not [54][82]. Therefore, even if the employed friction model is accurate, the disparity between the desired and actual velocities of the stage hampers the performance of model-based feedforward compensators in reducing the settling time during point-to-point positioning.

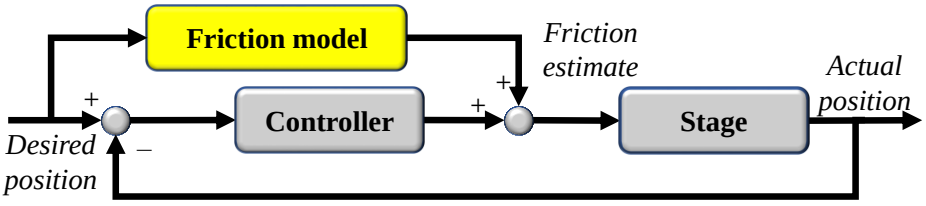


Figure 2.2 Schematic of model-based feedforward friction compensation approach.

In feedback compensation, the actual states (e.g., position and velocity) of the system are utilized (alongside the desired states) to mitigate the undesirable effects of friction. This prevents the problem related to having a stagnant velocity command during settling, as in feedforward compensation schemes. Feedback compensation can be done using model-free or model-based approaches. High gain controller is well known to be a model-free method that increases the disturbance rejection in feedback control systems. High gain methods applied to friction compensation include stiff PD [83]-[85], high integral gain [86][87] and joint torque control [88]-

[90]. While high gain feedback methods can be very effective in compensating friction, they often make the resulting systems to be prone to instability, sensitivity to sensor noise, integrator wind-up, chattering and limit cycles, all of which are very detrimental to the performance of NP stages [49][64][91]. These challenges of stability and robustness are further explained in Appendix A.1 through numerical simulations on a PID-controlled NP stage.

As shown in Figure 2.3, examples of model-based feedback compensation approaches include disturbance observer [66][67][75], gain scheduling controller [48][54][61][62][92], friction observer [49][82][93]-[95] and variable structure controller [13][96]. In general, these feedback compensation approaches also need high gains (e.g., integral gain) to aggressively overcome pre-motion friction [48][54][61]-[64]. Therefore, they share the same problems (e.g., overshoots, limit cycles and instabilities) of model-free high gain controllers in this respect [14][49][97]. By using implicit or explicit models (knowledge) of friction dynamics, the control structures or gains of model-based feedback compensators can be modified as the friction transitions from pre-motion to gross regime [48][54][61]-[64]. As a result, they avoid some of the pitfalls for maintaining high gains during abrupt nonlinear transitions of friction.

However, switching or modulating of controller gains (continuously or discontinuously) as a function of changing friction dynamics brings with it some problems. Firstly, switching itself can introduce stability issues, even if the systems between which switching occurs are by themselves stable [98]. These issues are mitigated in some studies by using conservative gains or by introducing dwell time between switching instances [48][64], at the expense of increased settling time. Secondly, as friction is extremely variable at the micro scale, variation of friction can create performance variations and stability issues for such switching controllers. Numerical simulation is conducted in Appendix A.2 using a recently proposed model-based feedback compensating controller to illustrate the stability and robustness issues arising from switching.

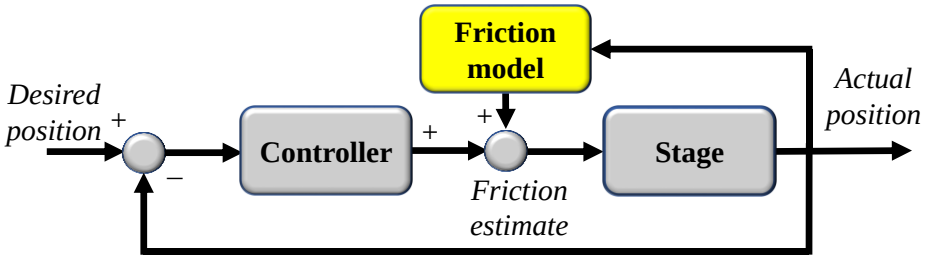


Figure 2.3 Schematic of model-based feedback friction compensation approach.

In summary, while research papers often report impressive improvements in the precision and speed of mechanical-bearing-guided NP stages using control-based friction compensation, these methods are often impractical in industry due to the need for complex models of friction whose parameters cannot be easily identified and/or due to robustness issues.

## 2.3 Mechatronics-based compensation approaches

Apart from the purely control-based compensation approaches discussed in Section 2.2, a less common way to reduce the undesirable effects of pre-motion friction is through design modifications of the conventional mechanical-bearing-guided NP stages, combined with control strategies – also known as mechatronics-based methods [99]. These methods generally achieve much better robustness as a result of the additional mechanical/electrical components. For example, a coarse-fine arrangement, where a "fine" flexure bearing stage is stacked on top of a "coarse" mechanical bearing stage is sometimes used to improve the precision and speed of mechanical-bearing-guided NP stages [100]-[102]. Similar ideas have been applied to improve the tracking accuracy and settling performance of hard disk drives [103]-[105]. In linear nanopositioning, the "coarse" stage is typically a direct-drive rolling bearing stage or a ball screw driven stage that delivers long range (> 50 mm) motions and the "fine" stage, that employs piezoelectric actuator, achieves nanometer-level precision but with limited stroke (< 100 $\mu$m) – see Figure 2.4 for two examples [106]-[108]. Two sensors are typically implemented, and the coarse-fine system is often controlled with a master-slave strategy; that is, the tracking error of the "coarse" stage is used as the reference commands for the "fine" stage [109][110]. The coarse-fine arrangements can significantly improve the precision and speed of mechanical bearing stages, enabling them to achieve long-range, NP motions [111][112]. However, the resulting systems are complex, bulky and expensive due to the additional structural components, actuators, sensors and control hardware [27][113]. Moreover, the performance of the "fine" stage is directly affected by the imprecision of the "coarse" stage such that extra care needs to be taken to decouple the dynamics of the two systems as much as possible [114]-[116]. This leads to further increases in cost, complexity and footprint [117].

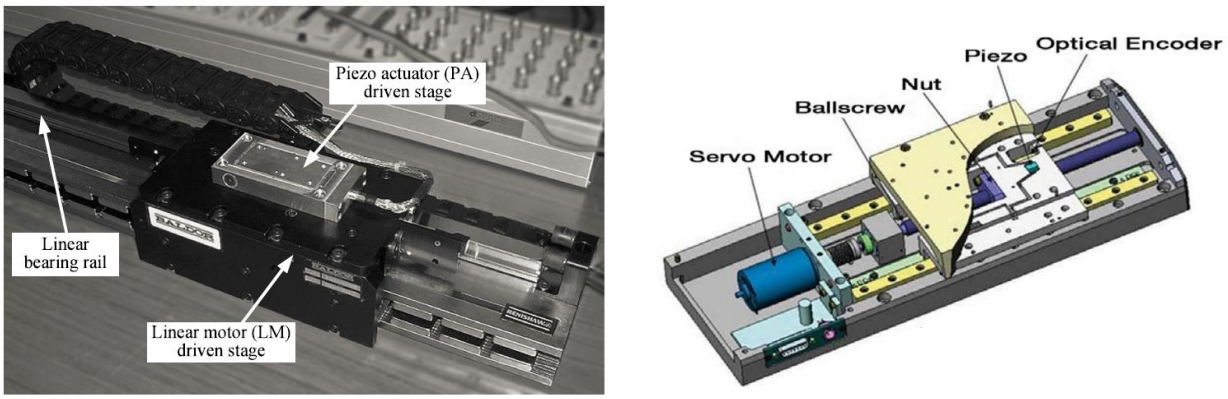


(a) (b)

Figure 2.4 (a) A dual-stage actuator NP system [102], and (b) long travel linear stage with nanometer-level precision using coarse-fine arrangement [118].

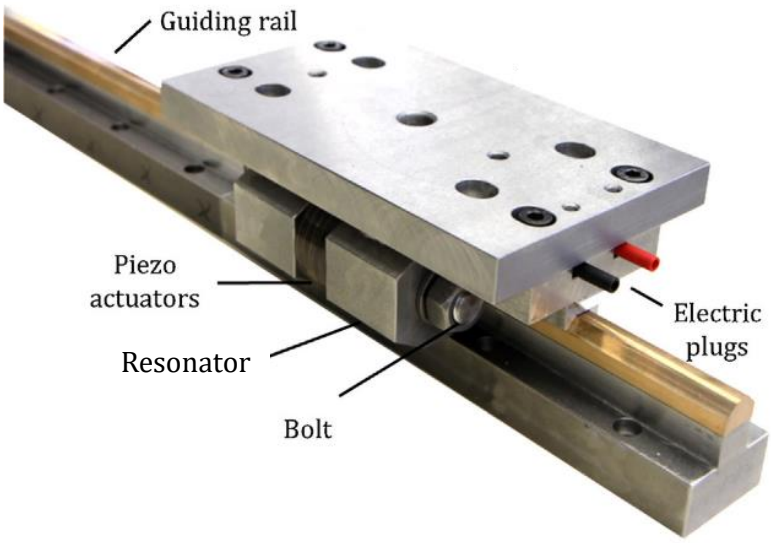


Figure 2.5 A dithering approach for mitigating stiction in sliding bearings of machine tools [119].

High frequency vibration (or dither) is well-known to be an effective, robust and model-free approach for mitigating nonlinear phenomena like friction, backlash and hysteresis [120]-[122]. Under sufficiently high frequency excitation, undesirable frictional phenomena like stick-slip and stiction are shown to disappear in an averaged sense [119][121][122], as is demonstrated in Appendix B. Therefore, dither is widely applied in spool valves of hydraulic servos, disc brakes

and flexible robot arms [49][123][124]. However, there are only a handful of references where dither is used in high precision positioning systems, mainly to reduce hysteresis in piezo actuators or to mitigate Coulomb friction in machine tools [119][125][126]. As shown in Figure 2.5, piezo-driven resonators are integrated in the sliding bearings of a precision machine tool to reduce stiction [119]. However, the machine suffers from micrometer-level vibrations during in-position due to the applied ultrasonic dithering forces. Similarly, Syamsul et al. apply ultrasonic oscillation to a mechanical-bearing-guided NP stage and investigate the effects of dithering waveform on the settling time during point-to-point motions and tracking accuracy during circular motions [127][128]. However, the need for continuously vibrating the rail and bearing carriage also causes large-amplitude oscillations (with a typical peak-to-peak value of 10 $\mu$m), severely jeopardizing the precision (i.e., in-position stability and tracking accuracy) of the NP stage [127][128].

## 2.4 Contribution of dissertation

As discussed in Section 2.2, purely control-based friction compensation methods often suffer from robustness problems, which hamper their practicality. The existing mechatronics-based approaches from Section 2.3 either have poor performance (e.g., dither) or lead to significant increases in cost and complexity (e.g., coarse-fine arrangement). To address the deficiencies identified in the literature, the following contributions are made in this dissertation:

- Three novel mechatronics solutions are proposed to effectively mitigate the undesirable effects of pre-motion friction in mechanical-bearing-guided nanopositioning (NP) stages; they are: 1) vibration assisted nanopositioning (VAN); 2) friction isolator (FI), and 3) semi-active isolator (SAI).
- Different from the traditional dithering techniques which jeopardize the motion precision by directly vibrating the stage or guideway, VAN is able to mitigate the slow settling problem without affecting positioning precision in the ideal scenario. A control scheme that implements a harmonic controller is proposed to address the problems of parasitic vibration due to non-idealities in practice. Using an in-house built prototype VAN stage with the proposed control scheme, significant improvement in settling time is achieved with nanometer-level positioning precision (Chapter 3).
- Although simpler and cheaper than the coarse-fine arrangement, VAN inevitably increases the cost of NP stages due to the need of additional actuators and voltage amplifiers to create

dithering. Therefore, FI is proposed as a simpler and more cost-effective method to mitigate the undesirable effects of pre-motion friction. The idea of FI is to connect the mechanical bearing to the moving table of a NP stage using a joint that is very compliant in the motion direction, thus effectively isolating the stage from the nonlinearities associated with bearing friction. A FI design that achieves low stiffness in the motion direction without overly sacrificing rigidity of the system in off-motion directions is proposed. The low-stiffness FI makes a model-free PID-type feedback controller to deliver high performance and robustness without the need for very high gains, leading to significantly reduced settling times during point-to-point motions. Moreover, the addition of the FI enables accurate and robust feedforward compensation of pre-motion friction using a simple model, resulting in large and robust reductions of tracking errors during circular motions (Chapter 4).

- One major pitfall of FI is that it causes increased motion error during in-position in the presence of noise from servo motor drives. Thus, SAI is proposed to mitigate the undesirable effects of pre-motion friction using FI, while maintaining the benefits of bearing friction on in-position stability. A SAI prototype is designed, which switches its stiffness between compliant and stiff using solenoid actuators and permanent magnets. A two-step control scheme is proposed to mitigate the adverse effects of switching on the positioning performance. By implementing the two-step error mitigation scheme, the stage with SAI simultaneously achieves fast settling and excellent in-position stability during point-to-point motions (Chapter 5).
- The proposed mechatronics-based approaches are compared with respect to their performance and practicality. The FI stands out due to its simplicity, low cost, excellent and robust performance in both point-to-point positioning and circular tracking motions. The influence of design parameters on the effectiveness of FI is then investigated through experimental and theoretical analysis to provide design guidelines for FI (Chapter 6).

# Chapter 3

## Vibration Assisted Nanopositioning

Vibration assisted nanopositioning (VAN) is proposed for mitigating the slow settling problem of mechanical-bearing-guided nanopositioning (NP) stages using high frequency vibration. The concept of VAN and how it addresses the challenges associated with traditional dithering approaches for NP applications are discussed in Section 3.1. The superior performance and robustness of the VAN approach in improving the settling time are demonstrated through numerical simulation in Section 3.2 and a control-scheme for compensating parasitic vibration caused by non-idealities is proposed. The design and sizing of a prototype VAN stage are shown in Section 3.3. Finally, the performance of VAN is experimentally validated using point-to-point positioning tests and circular tracking tests in Section 3.4.

This chapter is partially based on the following publications:

- Dong X, Yoon D, Okwudire CE. *A novel approach for mitigating the effects of pre-rolling/pre-sliding friction on the settling time of rolling bearing nanopositioning stages using high frequency vibration*. Precision Engineering. 2017; 47:375–388.
- Okwudire CE, Dong X. *Vibration Assisted Nanopositioning Stage*. US Patent. 2019; 10281829.

### 3.1 Concept of vibration assisted nanopositioning

As discussed in Section 2.3, high frequency vibration (or dither) is well known to be an effective, robust and model-free approach for smoothing nonlinearities like friction, hysteresis, backlash, etc. [120]-[122]. Under sufficiently high frequency and high amplitude dither, undesirable nonlinear frictional phenomena like stick-slip and stiction become linearized in an average sense, as is demonstrated in Appendix B [119][121][122]. However, there are only a handful of references where dither is used in precision positioning applications, mainly for

micrometer-level precision machines [119][127][128]. In general, when considering dither for mitigating pre-motion friction in NP stages, the following problems emerge:

- Traditionally, the dithering force ($F_d$) is applied indirectly to the location of friction ($F_f$) by adding it to the servo actuation force ($F_a$) of the stage (see Figure 3.1). However, the effectiveness of dither is greatly attenuated by the low pass filtering effect of stage dynamics. In order to achieve the desirable vibration amplitude, the dithering force must be large enough.
- Applying high amplitude dither to a NP stage through its servo actuator or bearing guideway directly causes excessive vibration of the moving table of the stage, thus, jeopardizing its positioning precision. There is no guarantee that the stage will stop at the target position after the dither is turned off.
- When high amplitude dither is maintained for prolonged periods of time, it causes accelerated wear of mechanical components. In addition, the power consumed by the high amplitude and high frequency vibration causes wastage of energy and potentially excessive heat generation [129].

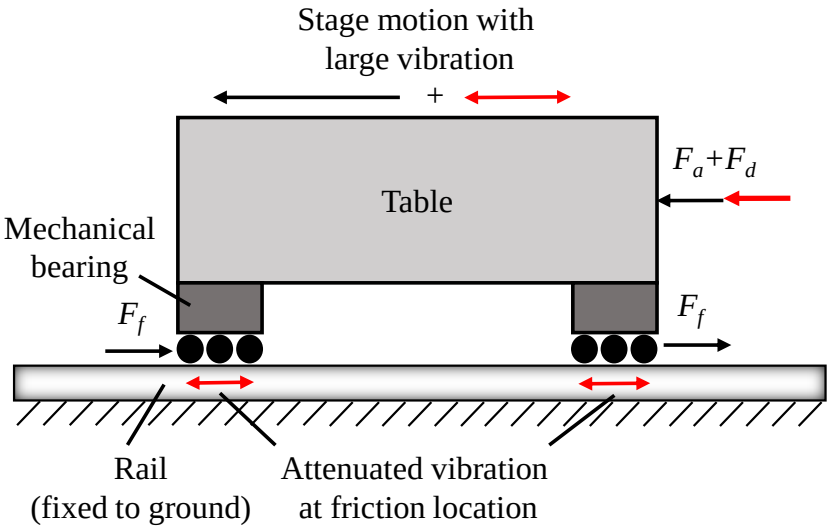


Figure 3.1 Schematic of traditional approach for applying dither to a NP stage.

To address the limitations of the traditional dithering approaches, this dissertation proposes a novel approach for applying dither to mechanical-bearing-guided NP stages which realizes the friction mitigation benefits of dither while significantly reducing its deleterious effects on the

precision of the stage. Figure 3.2 illustrates the proposed method, which is called vibration assisted nanopositioning (VAN). It has the following features:

- Each mechanical bearing is not directly/rigidly attached to the moving table of the stage; rather it is attached to the stage using a compliant joint (e.g., a flexure joint). The joint provides sufficient compliance in the motion direction of the stage while remaining stiff in other orthogonal directions, i.e., the off-axis (lateral and vertical) stiffness of the compliant joint is comparable to that of the mechanical bearing.
- The dithering force ($F_d$) is applied directly to each bearing using a small actuator (e.g., a voice coil motor or piezoelectric stack actuator) to create sufficient amplitude at the location of friction.
- In deal situations where the stage dynamics is perfectly symmetric, $F_d$ is applied with a phase difference of 180° to the bearings on the opposite ends of the stage such that their reaction forces transmitted to the stage cancel out.
- In non-ideal situations, parasitic vibration resulting from any un-cancelled reaction forces is minimized by regulating $F_d$ and/or by applying a compensating force ($F_{comp}$) to the stage using a control system.

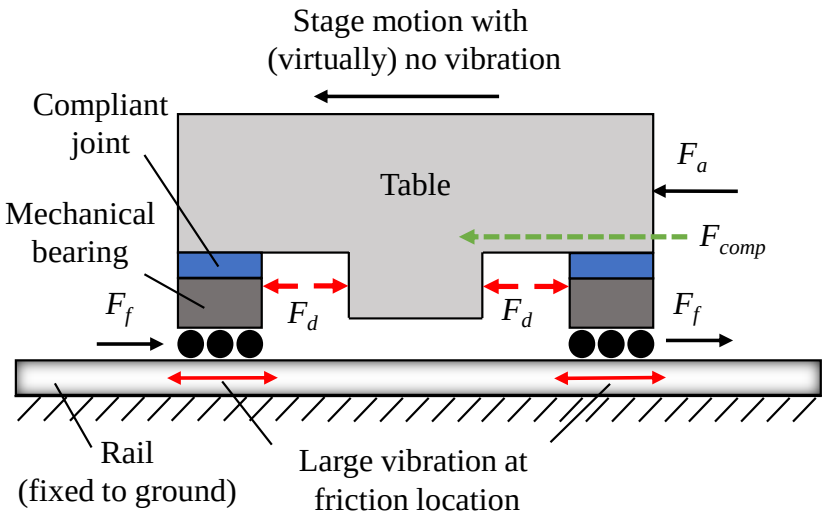


Figure 3.2 Schematic of the proposed VAN approach for applying dither to a NP stage.

Therefore, VAN is a mechatronics solution that synergistically combines mechanical design and active vibration control to ensure that the benefits of dither are realized with little or no

parasitic vibration of the stage. Applying dither directly to the bearings through a compliant joint rather than to the entire moving table reduces the amplitude and frequency of $F_d$, and the power required for dithering, which helps reduce heat and wear. Moreover, due to the symmetrically applied dithering signals, parasitic vibration at the moving table is minimized, enabling nanometer-level positioning precision. Note that, even though the VAN concept is depicted using a stage with one rail and two bearings in Figure 3.2, it is applicable to other stage configurations, such as a stage with two rails and four bearings.

## 3.2 Numerical simulation

### 3.2.1 Performance and robustness of vibration assisted nanopositioning (ideal case)

Figure 3.3 shows a simple three-mass mathematical model of a VAN stage that is closed loop controlled through the actuation force $F_a$. Each compliant joint connecting the table of mass $m_t$ to each bearing of mass $m_{bi}$ ($i$ = 1, 2) is modeled by a spring with stiffness $k_{cji}$ and a damper with viscous coefficient $c_{cji}$. Dither is applied in the form of harmonic excitation force $F_{di}$, with amplitude $A_i$ and frequency $f$. Without loss of generality, the compensating force, $F_{comp}$, is assumed to be applied at bearing 1; however, $F_{comp}$ could equally be applied at bearing 2, or elsewhere on the stage (e.g., through the stage's actuation force, $F_a$).

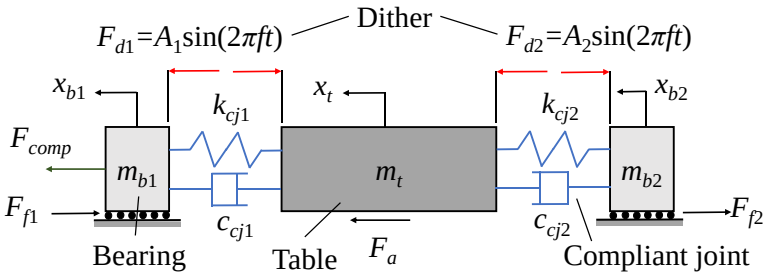


Figure 3.3 A three-mass mathematical model of the proposed VAN stage.

The system dynamics is described by

$$\mathbf{M\ddot{u} + C\dot{u} + Ku = F} \tag{3.1}$$

where **M**, **C** and **K** are respectively the mass, damping and stiffness matrices, while **u** and **F** are the displacement and force vectors of the system. They are given by

$$\mathbf{M}=\begin{bmatrix} m_{b1} & 0 & 0 \\ 0 & m_{b2} & 0 \\ 0 & 0 & m_t \end{bmatrix};\ \mathbf{C}=\begin{bmatrix} c_{cj1} & 0 & -c_{cj1} \\ 0 & c_{cj2} & -c_{cj2} \\ -c_{cj1} & -c_{cj2} & c_{cj1}+c_{cj2} \end{bmatrix};$$
$$\mathbf{K}=\begin{bmatrix} k_{cj1} & 0 & -k_{cj1} \\ 0 & k_{cj2} & -k_{cj2} \\ -k_{cj1} & -k_{cj2} & k_{cj1}+k_{cj2} \end{bmatrix};\ \mathbf{F}=\begin{bmatrix} F_{d1}+F_{comp}-F_{f1} \\ -F_{d2}-F_{f2} \\ F_a \end{bmatrix};\ \mathbf{u}=\begin{bmatrix} x_{b1} \\ x_{b2} \\ x_t \end{bmatrix} \tag{3.2}$$

where $x_t$ and $x_{bi}$ are respectively the displacements of the moving table and bearings.

In an ideal VAN stage, one would expect a perfectly symmetric system such that the mass, damping, stiffness and friction properties of both bearings are exactly the same. In this case, $F_{comp}$ can be eliminated and $F_{d1} = F_{d2} = A\sin(2\pi ft)$ can be used to achieve the purposes of VAN. This ideal situation is evaluated through numerical simulations for a PID-controlled VAN stage model of Figure 3.3 with $m_t$ = 1 kg, $m_{b1} = m_{b2}$ = 0.25 kg, $k_{cj1} = k_{cj2}$ = 5 N/$\mu$m, $c_{cj1} = c_{cj2} = 2 \times 10^{-5}$ N·s/$\mu$m (corresponding to 1% damping ratio) and $F_{f1} = F_{f2} = F_f$. In Appendix A, numerical simulations are carried out to illustrate the stability and robustness issues of feedback friction compensation approaches, using the industrial-standard PID controller and the Nonlinear Integral Action Settling Algorithm (or NIASA for short), recently proposed by Bucci et al. [54][61]. Note that NIASA is a controller that replaces the fixed integral gain of a regular PID controller with the Dahl friction model in Eq. (1.1). To allow a direct comparison between VAN and the numerical examples presented in Appendix A, the total mass of the VAN stage (i.e., $m = m_t + m_{b1} + m_{b2}$), its P and D controller gains, and its frictional parameters (represented by the Dahl model in Eq. (1.1)) are exactly the same as used in Appendix A – see Table A.1; the selected stiffness and damping ratios are consistent with those of a properly sized compliant joint, as discussed in Section 3.3. The most conservative integral gain of Figure A.2 (i.e., $K_I$ = 10 N/($\mu$m·s)) is used for the VAN stage in all simulations.

Figure 3.4 shows the settling times of VAN as functions of $A$ and $f$ for the same tests as in Figure A.2 and Figure A.3 from Appendix A (in response to 50 nm and 500 nm step commands), using various values $\delta$. Note that $\delta \in [-1, \infty)$ is a multiplicative uncertainty parameter introduced

by Bucci et al. into the initial contact stiffness, $k_\sigma$, of the Dahl model described in Eq. (1.1) to help demonstrate the robustness of NIASA to changing friction; i.e., $k_\sigma = k_{\sigma,n}(1 + \delta)$, where $k_{\sigma,n}$ is the nominal value of $k_\sigma$ [61]. For all four values of $\delta$ applied to both step commands, the settling time characteristics of the VAN stage can be said to have a cliff, a canyon and a plain. At very low amplitudes and frequencies, the addition of dither produces little or no effect in reducing settling time (as is also predicted by the analysis in Appendix B). But as $A$ and $f$ are increased beyond their optimal values, the settling time increases slightly after which it remains largely unchanged (i.e., the plain). The canyon provides optimal settling performance at relatively low $A$ and $f$ values. Therefore, operating within the canyon region could also provide benefits with regard to the reduction of heat and wear caused by dither. However, the challenge is that the canyon is very narrow and close to the cliff; settling times could rise sharply if the optimal dithering amplitudes or frequencies are not precise. The plain is excellent in terms of robustness because it provides a wide range of $A$ and $f$ values to choose from without losing performance. Notice also that for the four values of $\delta$, the characteristics of the cliff, canyon and especially the plain is very similar. This means that with sufficiently high $A$ and $f$ values, the performance of VAN is highly insensitive to uncertainties in $k_\sigma$. This fact can also be verified based on the theoretical example presented in Appendix B. It shows that, with sufficiently high amplitude and high frequency dither, the averaged dynamics of the stage does not exhibit any pre-motion stiffness behavior and all nonlinear aspects of friction (based on the Dahl model) are linearized. As a result, significant reductions of settling time are achieved without requiring high integral gain or model-based switching of controller gains/structures, and uncertainties in $k_\sigma$ do not influence controller performance.

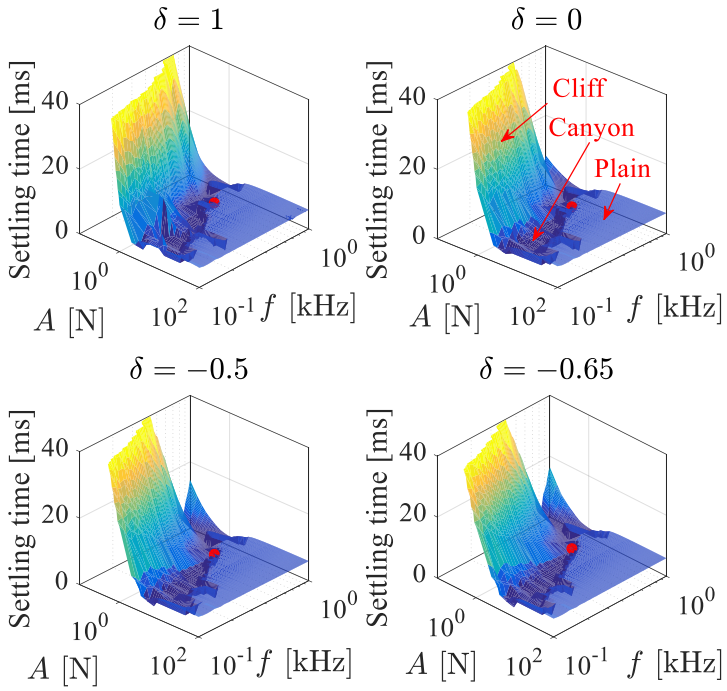


(a)

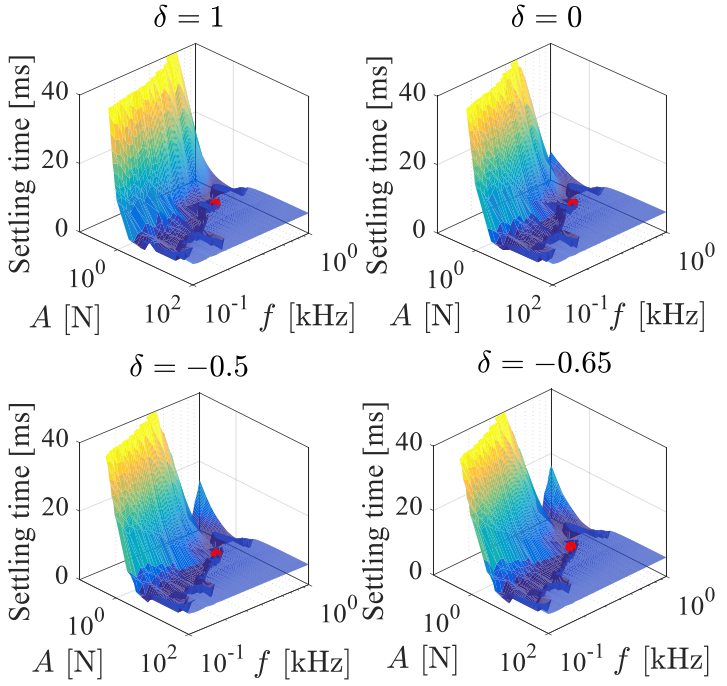


(b)

Figure 3.4 Effect of dithering amplitude ($A$) and frequency ($f$) on settling time of the VAN stage in response to (a) 50 nm, and (b) 500 nm step commands using different values of uncertainty $\delta$ in the Dahl friction model. The red dot represents the operating point of $A$ = 3 N and $f$ = 500 Hz.

To further illustrate this point, Figure 3.5 shows the settling responses of VAN to the 50 nm and 500 nm step commands for various values of $\delta$ using $A$ = 3 N and $f$ = 500 Hz, as highlighted by the red dot on each subplot in Figure 3.4. Compared to the NIASA (as shown in Figure 3.6 and Figure A.3), VAN demonstrates superb robustness and settling performance that is very close to the benchmark settling performance, achieved under zero friction conditions, regardless of frictional uncertainties and magnitudes of the reference signals.

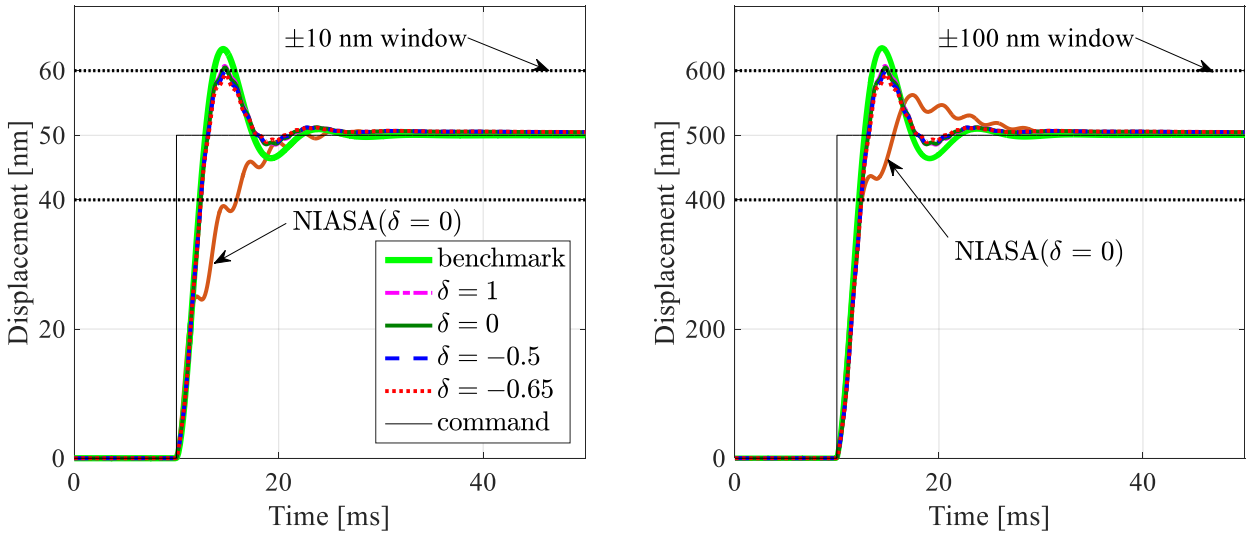


Figure 3.5 Settling results of VAN in response to (a) 50 nm, and (b) 500 nm step commands using different values of initial contact stiffness in the Dahl model. Note that $A$ = 3 N and $f$ = 500 Hz.

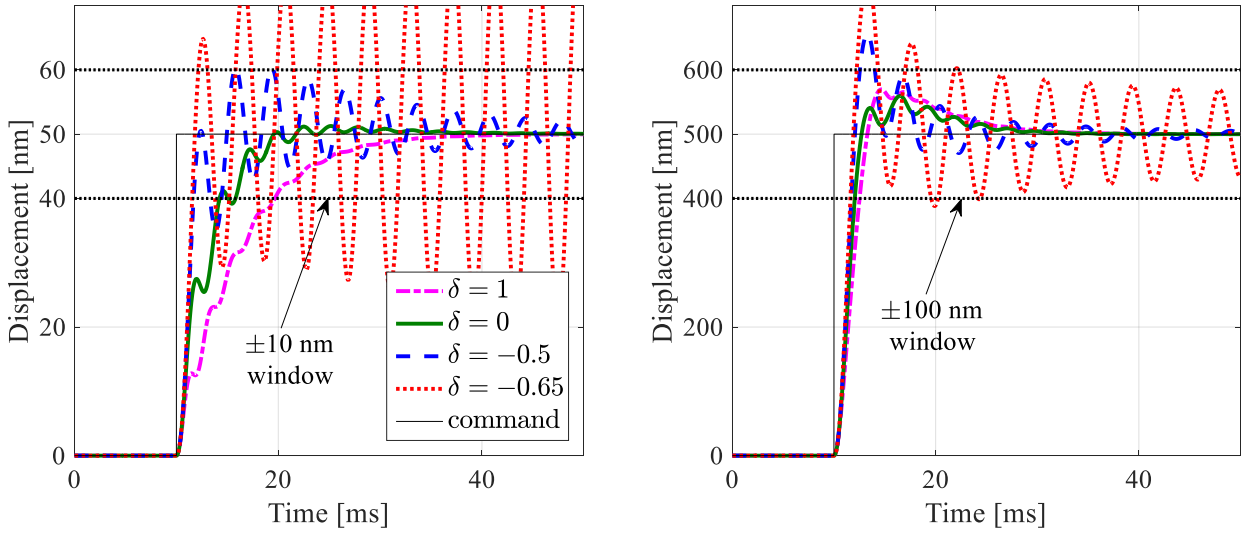


Figure 3.6 Settling results with NIASA in response to (a) 50 nm, and (b) 500 nm step commands using different values of uncertainty $\delta$ in the initial contact stiffness of the Dahl model. Details can be found in Appendix A.2.

### 3.2.2 Compensation of parasitic vibration caused by non-idealities

In Section 3.2.1, the superb performance and robustness of VAN are demonstrated under the ideal situation where the parameters and friction conditions of both bearings are exactly the same. In reality, non-idealities exist due to different frictional parameters, dithering forces, manufacturing and assembly errors. This leads to unbalanced reaction force and parasitic vibration that may adversely affect precise positioning of the VAN stage.

A rudimental way to deal with parasitic vibration is through an on-off regulation technique, where dither is applied and then suddenly turned off after duration $T$, starting when the reference command reaches the target position [130]. Significant improvements in settling times are demonstrated in both simulations and experiments using the on-off regulation method [130]. However, it is observed that the abrupt switching introduces some undesirable transients which can have large amplitudes if the damping of the stage is small. Moreover, the settling performance is highly dependent on the cutoff time, $T$, requiring one to identify the optimal $T$ based on a large number of trials for each position command.

To address these issues with the on-off control technique, a control scheme for generating $F_{comp}$ to eliminate parasitic vibration due to non-idealities is proposed, as shown in Figure 3.7. The signal $x_r$ is the reference position of the table, $F_d = A\sin(2\pi ft)$ is the dithering force which is applied 180° out of phase to both bearings, reflecting the ideal case. A harmonic cancelling (HC) controller [131], is used to generate $F_{comp}$ as a function of the position error of the stage, $e = x_r - x_t$. The generated $F_{comp}$ is then added to the dithering force of bearing 1. Note that a HC controller is a type of repetitive controller [131], designed based on the internal model principle which states that a controller must contain a model of any disturbance that must be rejected with zero steady-state error [132]. In the case of the VAN stage, the disturbance force that must be rejected is the un-balanced reaction force due to dither. It can be assumed to be dominated by a harmonic signal at frequency $f$. Therefore, the transfer function for the HC controller is given by

$$G_{HC}(s) = K_{HC}\frac{s}{s^2 + \omega^2} \tag{3.3}$$

representing the transfer function of a harmonic signal at frequency $f$, where $s$ is the Laplace variable, $\omega = 2\pi f$, and $K_{HC}$ is a tunable gain. For any $K_{HC} > 0$, the magnitude of $G_{HC}$ is theoretically infinite at $s = j\omega$ (where $j$ is the unit imaginary number), ensuring that any disturbance (and associated error, $e$) occurring at frequency $f$ is rejected with zero steady-state error, by modulating the amplitude and phase of $F_{d1}$ relative to $F_{d2}$.

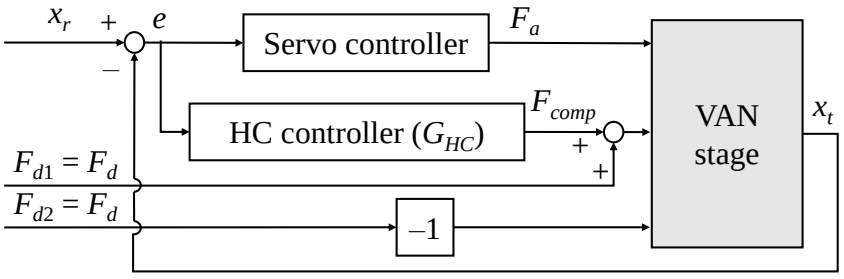


Figure 3.7 Block diagram of the proposed control scheme for compensating parasitic vibration caused by non-idealities.

To evaluate the proposed control scheme in the presence of non-idealities, let us consider a scenario where the stiffness and damping coefficients of the two compliant joints differ by 10% due to manufacturing errors; i.e., $k_{cj2} = 1.1 \times k_{cj1} = 5.5$ N/$\mu$m and $c_{cj2} = 1.1 \times c_{cj1} = 2.2 \times 10^{-5}$ N·s/$\mu$m, while the other parameters remain exactly the same as used in Figure 3.5, with $\delta = 0$. Figure 3.8(a) compares the settling behavior of VAN in response to a 50 nm step command with different repetitive controller gains; very similar results are obtained for the 500 nm case, and are excluded for the sake of brevity. Note that without the HC controller (i.e., $K_{HC} = 0$), the VAN stage suffers from parasitic vibration with a peak-to-peak amplitude of 40 nm, causing it to not settle within the desired window. By introducing the HC controller, the parasitic vibration is gradually reduced, allowing the stage to settle. Notice that the rate of attenuation of the parasitic vibration gets faster as $K_{HC}$ increases. However, $K_{HC}$ cannot be tuned arbitrarily high because a high $K_{HC}$ could introduce instabilities in the HC controller. Therefore, the same type of conservatism that is applied to tuning the integral gain of a PID-type linear-time-invariant (LTI) controller must be applied when tuning $K_{HC}$. Note that the large overshoots experienced when the HC controller is active occur because dither is initiated at the same time as the step command, and the HC controller takes a while to suppress the resulting parasitic vibration. Figure 3.8(b) compares the position error of the initial step for $K_{HC} = 4 \times 10^3$ N/$\mu$m shown in Figure 3.8(a) to subsequent steps, applied after the HC controller has taken effect. It shows that the overshoots reduce over time. This means that, to avoid large overshoots, dither could be applied preemptively, allowing parasitic vibration to settle before position commands are issued.

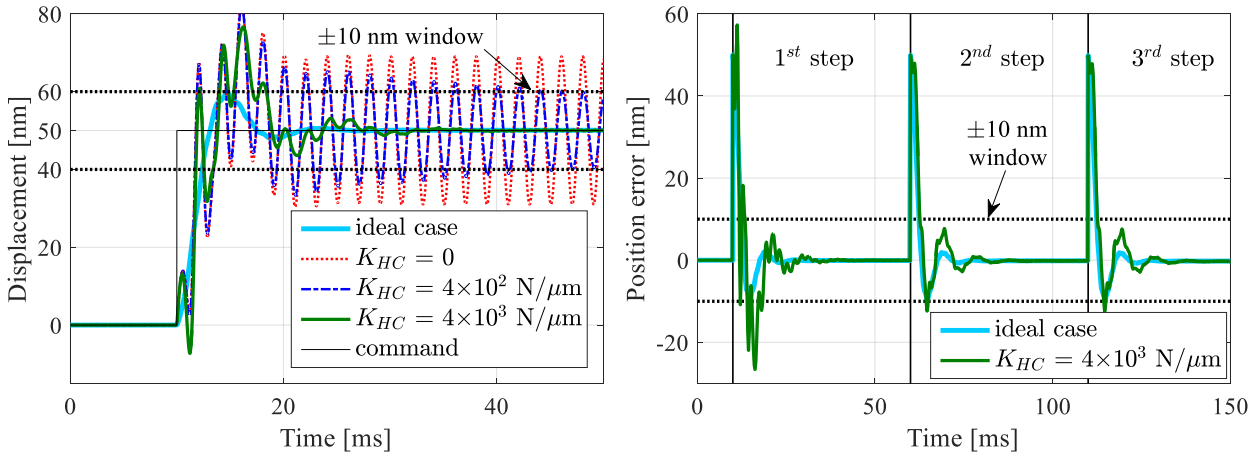


Figure 3.8 (a) Settling results of VAN (in the presence of non-idealities) in response to a 50 nm step command with different HC controller gains, and (b) position errors of three successive step commands with $K_{HC} = 4 \times 10^3$ N/$\mu$m. Note that $\delta = 0$, $A = 3$ N and $f = 500$ Hz are used in all simulations.

### 3.3 Design of a vibration assisted nanopositioning stage

A prototype VAN stage is designed according to the general concept described in Section 3.1. Figure 3.9 shows the CAD drawings of the prototype stage. It has a 2 kg moving mass and 50 mm travel range. The stage is guided by a pair of high-rigidity linear ball bearings with end seals (THK, SR-15SB), riding on a super-precision grade rail, lubricated using grease (THK, AFB-LF). An air core linear motor (Aerotech Inc., BLMUC-95) with 162 N peak and 23 N continuous force limits is employed to drive the stage. The table position is measured using a linear encoder system (Renishaw, T1000 read head and RGSZ20 scale) with a post-interpolation resolution of 4.88 nm; notice that the linear encoder is mounted on the side of the table that is not visible in Figure 3.9. A pair of preloaded piezoelectric stack actuators (PI, P-842.10) is selected to provide the dithering forces; each actuator has a travel range and blocking force of up to 15 $\mu$m and 300 N, respectively, with a maximum operating frequency of 6 kHz under unipolar operation (0 – 100 V). Two flexure mechanisms, made of AISI 304 stainless steel, are designed with their central platforms each connected to the moving table of the stage and their outer platforms connected to their associated bearings. Their roles are to provide sufficient compliance in the direction of dither (i.e., axial direction) to allow displacements in the order of 10 $\mu$m while remaining stiff in the off-axis (i.e.,

lateral and vertical) directions, such that the high stiffness of the linear ball bearings is not unduly sacrificed. Note that the dithering amplitudes in the order of 10 $\mu$m are considered to be sufficient because the pre-motion friction regime of mechanical bearings becomes most pronounced within 5 – 10 $\mu$m of the target position [54].

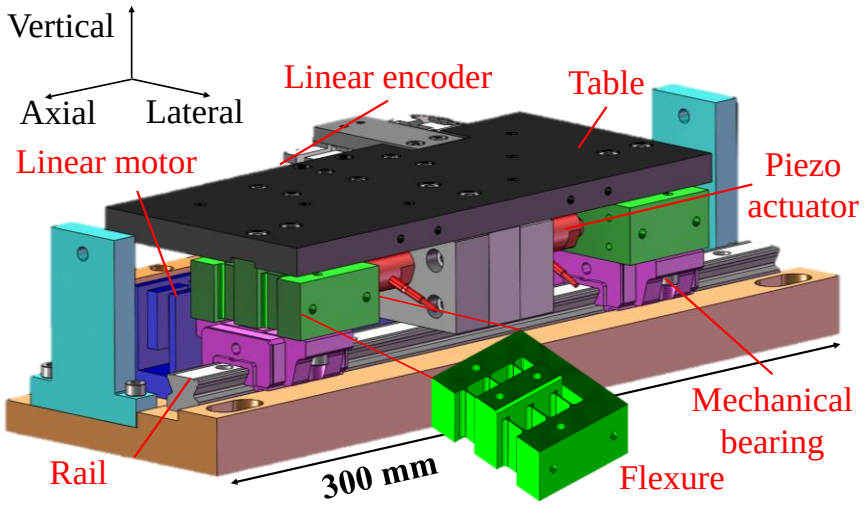


Figure 3.9 CAD model of the prototype VAN stage. The linear encoder is mounted on the distal side of the table.

Table 3.1 Stiffness values of each mechanical bearing, flexure and their combination (i.e., bearing + flexure in series) [N/m].

| | Axial | Vertical | Lateral |
|---|---|---|---|
| Mechanical bearing | N/A | $6 \times 10^7$ | $2 \times 10^7$ |
| Flexure | $6.9 \times 10^6$ | $3.1 \times 10^8$ | $3.3 \times 10^8$ |
| Combined (bearing + flexure) | N/A | $5 \times 10^7$ | $1.9 \times 10^7$ |

Table 3.1 summarizes the stiffness values of each flexure (obtained via finite element analysis using SolidWorks®), the stiffness values of each mechanical bearing (sourced from its manufacturer's catalog [43], and the combined stiffness values of each flexure and bearing (which are in series). Notice that the vertical and lateral stiffness values of each flexure are designed to be much higher than its axial stiffness. Consequently, the combined stiffness of the flexure and linear

ball bearing in the vertical and lateral directions have the same order of magnitudes as those of the bearing alone.

Figure 3.10 shows the force-displacement characteristics of the piezo stack actuator with unipolar operation at different voltage levels, obtained from its manufacturer's datasheet [133]. With its axial stiffness of 6.9 N/$\mu$m, the flexure provides 11 $\mu$m of displacement (with 77 N force) at the maximum operating voltage of the piezo actuators (i.e., 100 V). Using SolidWorks®, the maximum von Mises stress of the flexure (with the maximum applied load of 77 N) is calculated as $S_{max}$ = 43 MPa. This gives a safety factor of 4.8 with regard to the yield strength $S_y$ of the selected material (i.e., 304 stainless steel), see Table 3.2. In the presence of cyclic stresses (as is the case with dither), the stress-life method can be employed to determine the strength of materials against fatigue [134]. Infinite fatigue life is guaranteed if the maximum stress is below the endurance limit, $S_e$, which can be obtained from the Marin equation [134][135]

$$S_e = p_a p_b p_c p_d p_e p_f S'_e \tag{3.4}$$

where $S'_e$ is the nominal endurance limit of a carefully prepared rotary-beam specimen under closely controlled conditions; $p_a$, $p_b$, $p_c$, $p_d$, $p_e$ and $p_f$ are respectively Marin factors that help account for the effects of surface condition, size, loading, reliability, temperature, and miscellaneous items. The nominal endurance limit is estimated as half of the ultimate tensile strength, $S_{ut}$, as shown in Table 3.2. The surface factor of a machined structure is given by [134]

$$p_a = 4.51 S_{ut}^{-0.265} \tag{3.5}$$

while the size factor based on the designed flexure can be calculated using [134]

$$\begin{aligned} p_b &= 1.24 d_e^{-0.107}; \\ d_e &= 0.808\sqrt{hd} \end{aligned} \tag{3.6}$$

where $d_e$ is the equivalent diameter of the thin flexure hinge (of rectangular section) with height ($h$) of 19 mm and thickness ($d$) of 1 mm. A reliability factor of $p_e$ = 0.814 is used (based on 99%

reliability) and the remaining factors are set equal to 1, assuming standard operating conditions. The estimated Marin factors and strength properties are summarized in Table 3.2. Note that the calculated endurance limit of 304 stainless steel (i.e., 195.4 MPa) is much higher than the maximum von Mises stress of 47 MPa. Thus, even under the worst-case loading, infinite life against fatigue failure is guaranteed for the designed flexure mechanism.

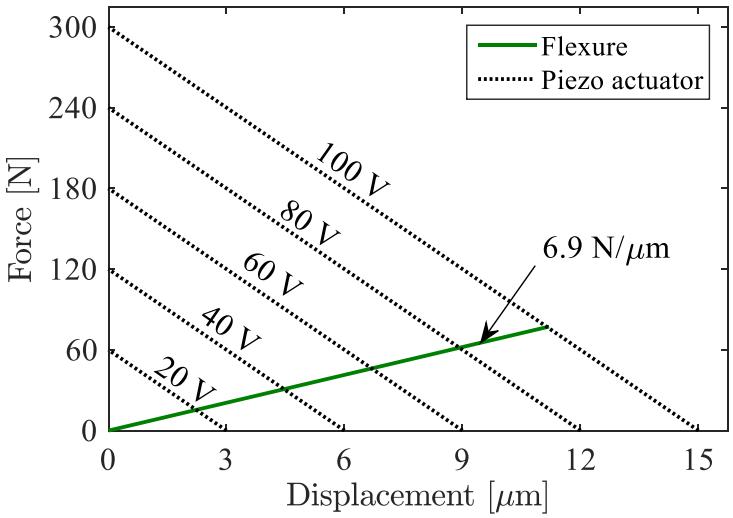


Figure 3.10 Force-displacement relationship of piezo stack actuators at different voltage input levels superimposed with axial force-displacement relationship of flexure mechanism obtained from finite element analysis using SolidWorks®.

Table 3.2 Strength properties of the designed flexure.

| | |
|---|---|
| $S_{max}$ = 47 MPa | $p_a$ = 0.86 |
| $S_{ut}$ = 517 MPa | $p_b$ = 1.08 |
| $S_y$ = 207 MPa | $p_c$ = 1 |
| $S_e^{'}$ = 258.5 MPa | $p_d$ = 1 |
| $S_e$ = 195.4 MPa | $p_e$ = 0.814 |
| $d_e$ = 3.52 mm | $p_f$ = 1 |

Figure 3.11 shows an in-house built prototype VAN stage. The linear motor is driven in force control mode by a linear amplifier (Trust Automation, TA-310). The piezo stack actuator

pair is driven separately by voltage amplifiers (PI, E505) which each has an amplification ratio of 10:1.

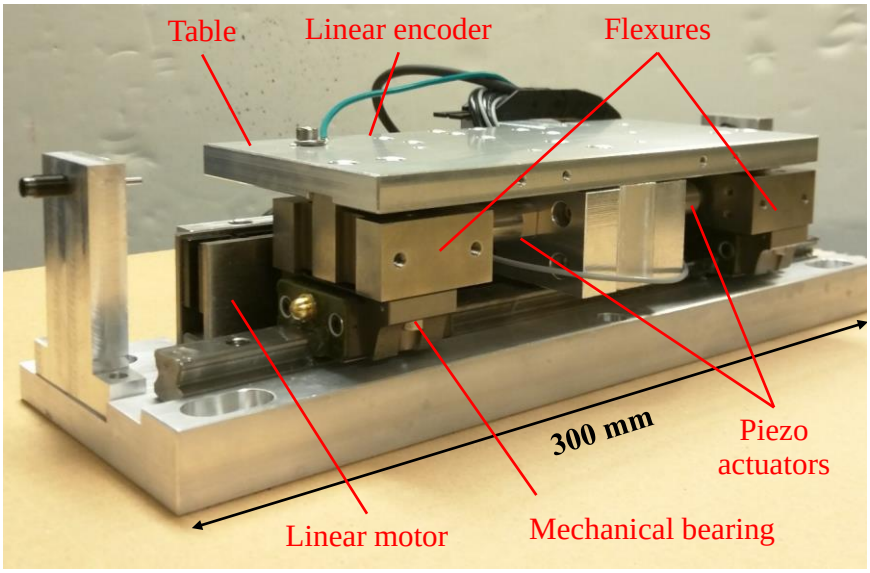


Figure 3.11 Picture of the assembled prototype VAN stage. The linear encoder is mounted on the distal side of the table.

Figure 3.12 shows the magnitude and phase plots of frequency response functions (FRFs) measured from the stage; each FRF is obtained by applying constant-amplitude sinusoidal voltage input commands with varying frequencies to the piezo actuator and recording the corresponding output displacement magnitudes of the stage's position using the linear encoder. In both FRFs, a low frequency resonance peak is observed (around 80 Hz), which is characterized as the Dahl resonance of the nonlinear elastic friction in the pre-motion regime [55]. The higher resonance peaks at around 560 Hz are due to the yaw mode of the stage. Notice that, though the input commands for the two piezo actuators are identical, the obtained FRFs have large discrepancies in terms of both magnitude and phase. At lower frequencies, the magnitudes differ by a constant offset value, but the phase difference is close to the desired 180°. On the other hand, at higher frequencies, their magnitudes are closer in value, but their difference in phase is further away from 180°. The mismatched dynamics of the two piezo actuators can be attributed to non-uniformities in the mechanical properties and frictional behaviors of the two linear ball bearings, their flexures and piezo actuators, as discussed in Section 3.2.2.

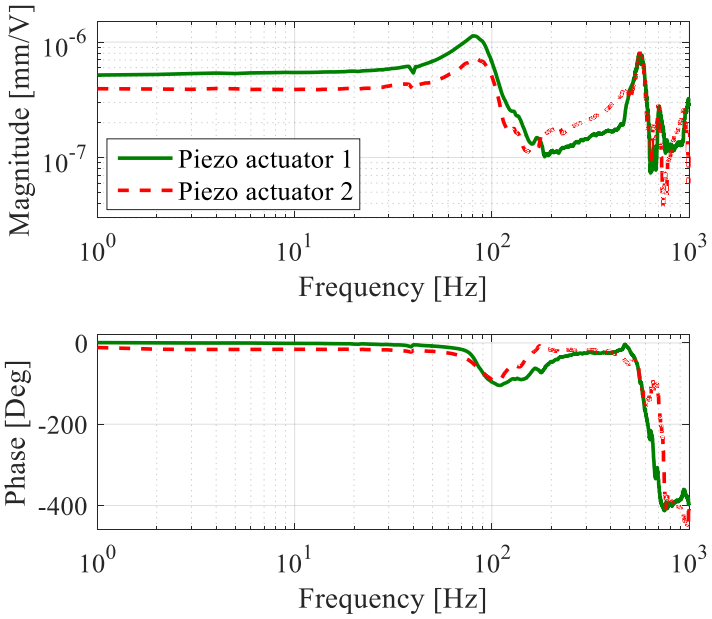


Figure 3.12 Measured open loop frequency response functions (FRFs) from piezo actuator voltage (input) to table position (output). Note that 180° is added to the phase plot of piezo actuator 1 to facilitate easy comparison.

## 3.4 Experimental validation

The performance of the prototype VAN stage is experimentally evaluated using point-to-point positioning tests and circular tracking tests. The control scheme described in Section 3.2.2 is implemented on a real-time controller (dSPACE, DS1007) running at 10 kHz sampling frequency. The servo controller of the stage is a PID-type LTI controller, tuned to have a closed loop bandwidth of 180 Hz using the traditional loop shaping approach, without any information about the applied dithering forces or pre-motion friction dynamics. Note that the servo controller cannot compensate for any un-balanced reaction forces caused by dither with frequencies above its bandwidth of 180 Hz.

### 3.4.1 Point-to-point positioning tests

During point-to-point positioning tests, the stage is given 5 mm and 5 $\mu$m step commands – see Figure 3.13 for the example of a 5 mm point-to-point motion profile. The settling portion,

after the reference command reaches the target position as indicated by the red dashed line, is considered. The time taken for the stage to settle into a ±25 nm window during the settling portion is evaluated for the following cases:

- No dither: no dither is applied; this represents a conventional mechanical-bearing-guided NP stage;
- Dither with HC: dither is applied with the proposed control scheme having the HC controller (see Figure 3.7).

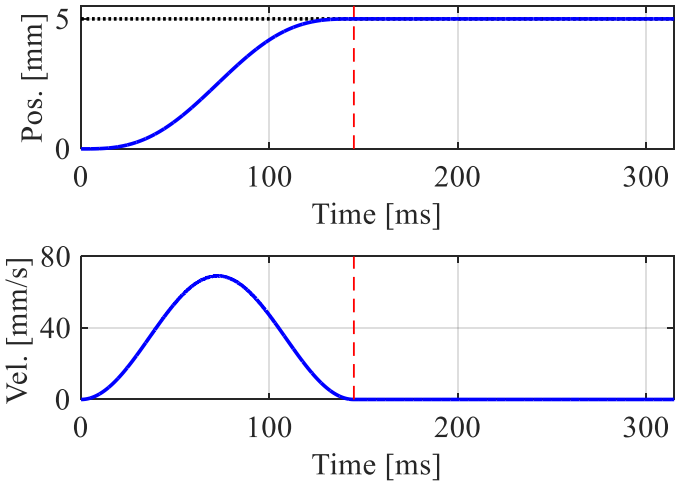


Figure 3.13 Position and velocity commands of a typical 5 mm point-to-point motion profile. The red dashed line indicates the start of the settling portion.

Figure 3.14 compares the settling performance of the stage into the ±25 nm window during 5 mm point-to-point positioning test. Apart from the abovementioned two cases, the open loop controlled dither (i.e., without the HC controller) is also plotted for comparison. The settling portion is highlighted in the subplot. Dithering input with peak-to-peak amplitude of 20 V (corresponding to 15 N in applied force and approximately 2 $\mu$m in bearing displacement) is used. It is known that high frequency dithering generally is more effective in mitigating nonlinear effects of friction [119][121]. Therefore, the dithering frequency is set to 500 Hz, in order to attain high frequency dithering while avoiding the resonance peaks around 560 Hz in the dynamics of the piezo actuators (see Figure 3.12). Without dither, the stage takes 108 ms to settle, which is very long relative to the total duration of the reference trajectory (125 ms). With open loop controlled

dither (i.e., Dither w/o HC), as expected, the stage experiences parasitic vibration, especially in the settling region, with amplitude of about 600 nm, causing the stage to not settle into the desired window. The proposed control scheme with the HC controller is then applied, helping the stage with dither to settle within 38 ms, which is 65% faster than the case without dither. Compared to the No dither case, the stage with dither has smaller overshoot around the target position, causing the stage to move faster into the desired settling window.

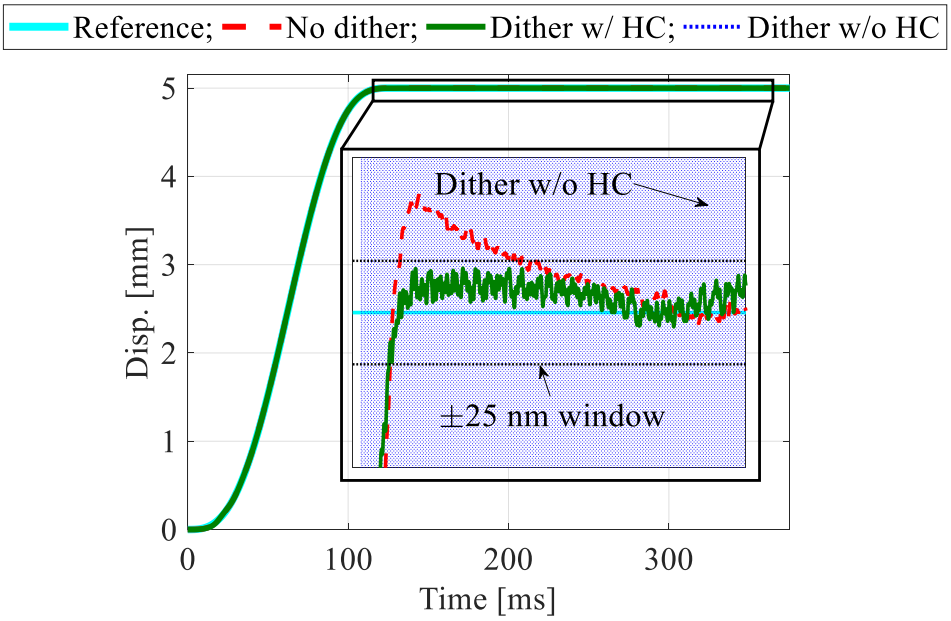


Figure 3.14 Typical settling performance of No dither, Dither without and Dither with the proposed HC control scheme into the ±25 nm window during 5 mm point-to-point motion. The black box shows the settling portion.

Figure 3.15 shows the frequency spectrum of the in-position vibration amplitude after the stage settles inside the ±25 nm window. The stage without dither (i.e., No dither) has an RMS in-position error of 1.9 nm. The large peak (with an amplitude of 607 nm) of Dither without HC case, occurring at 500 Hz indicates that the parasitic vibration is mainly concentrated at the dithering frequency. This leads to an RMS in-position error of 400 nm, severely jeopardizing the precision of the stage. Thanks to the HC controller, the dominant peak at 500 Hz is eliminated. However, some low frequency disturbances around 50 – 300 Hz show up when dither is applied, causing a 42% increase of the RMS in-position error, compared to No dither case. Due to the initially very

large stiffness of pre-motion friction, mechanical bearings often have excellent in-position stability in the presence of noise from servo motor drives, compared to, e.g., air bearings which have near-zero stiffness in the motion direction. As the high frequency vibration mitigates the nonlinear spring characteristics of pre-motion friction, the benefits of bearing friction on the in-position stability are also jeopardized.

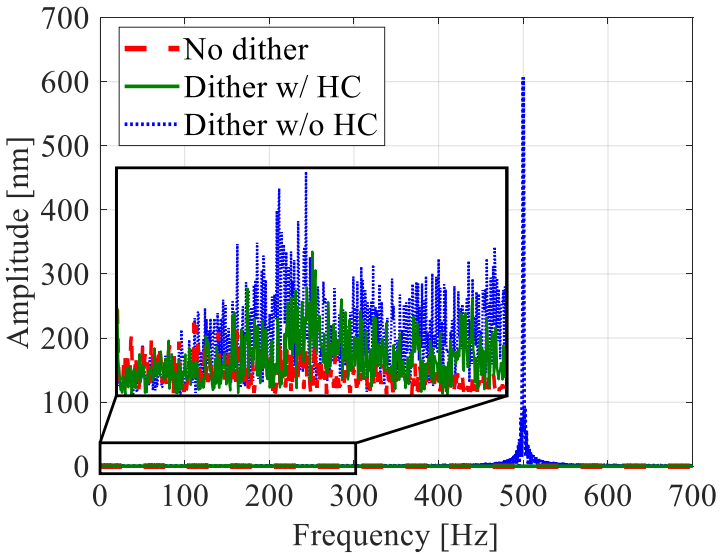


Figure 3.15 Frequency spectra of the position error signals during in-position.

Figure 3.16 shows the typical settling performance of the stage with and without dither during 5 $\mu$m step motion. The No dither case takes 168 ms to settle into the desired ±25 nm window. Using dither with the proposed HC controller, the stage settles within 120 ms, which is 29% faster. Similar to the 5 mm step motion, the introduction of dither leads to a 43% increase in the RMS in-position error.

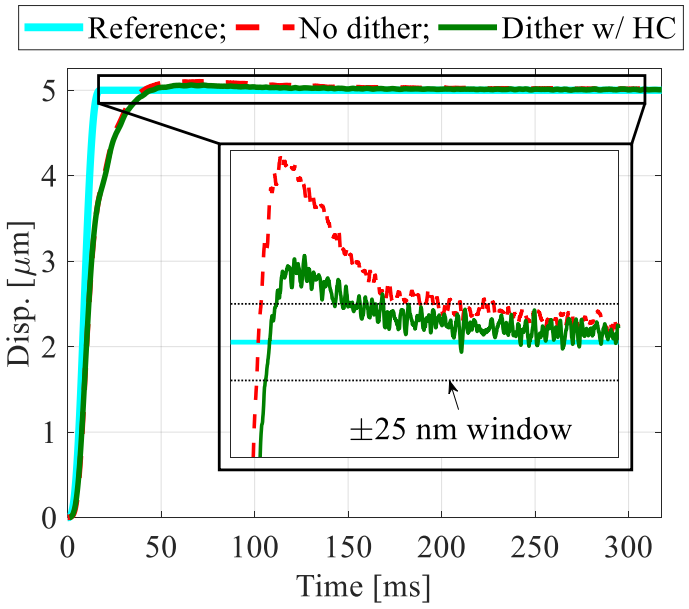


Figure 3.16 Typical settling performance of the stage with and without dither into the ±25 nm window during 5 $\mu$m point-to-point motion. The black box shows the settling portion.

Figure 3.17 and Figure 3.18 compare the settling time and in-position stability during 5 mm and 5 $\mu$m point-to-point positioning tests, based on 50 trials at random positions along the travel range of the stage and Table 3.3 summarizes the mean settling time and RMS in-position error. The settling times of the No dither case are 91 ms and 188 ms for the 5 mm and 5 $\mu$m steps, respectively. The Dither with HC case achieves 66% and 22% reductions in mean settling times, at costs of 50% and 45% increases of RMS in-position errors, compared to the stage without dither.

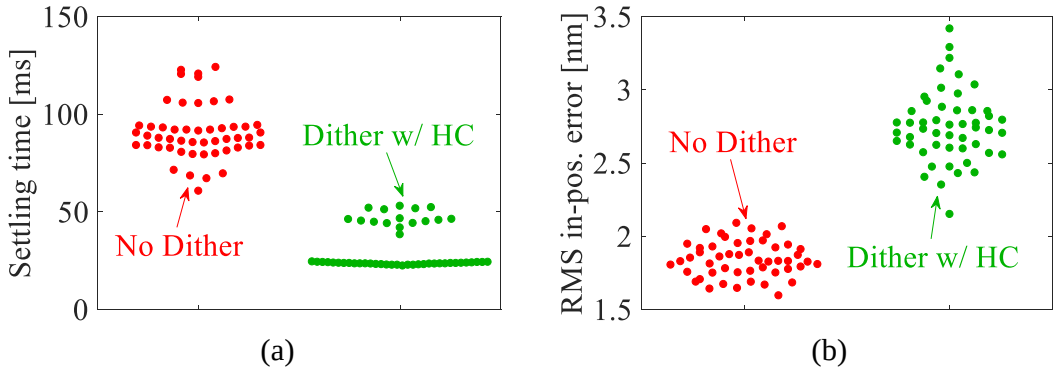


Figure 3.17 Comparison of (a) settling time into the ±25 nm window, and (b) RMS in-position error during 50 trials of 5 mm point-to-point motions.

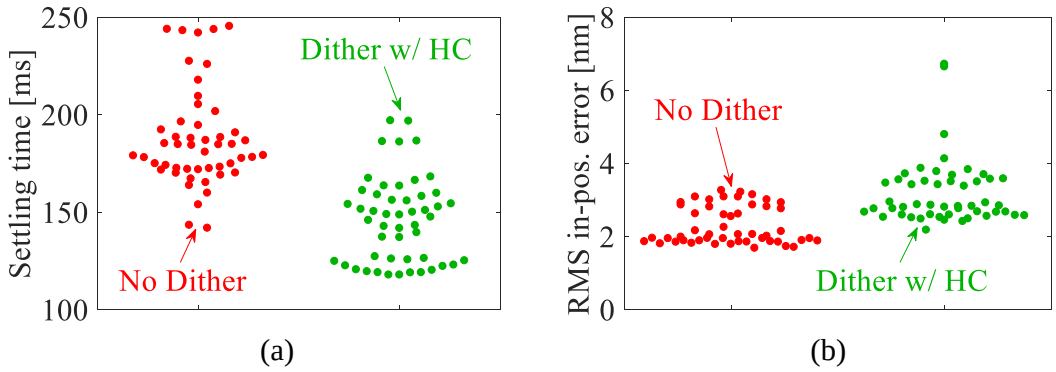


Figure 3.18 Comparison of (a) settling time into the ±25 nm window, and (b) RMS in-position error during 50 trials of 5 $\mu$m point-to-point motions.

Table 3.3 Comparison of mean settling time and in-position error (RMS) during 50 trials of 5 mm and 5 $\mu$m point-to-point motions.

| | | No dither | Dither w/ HC |
|---|---|---|---|
| 5 mm step | Settling time [ms] | 91 | 31 |
| | RMS in-pos. error [nm] | 1.8 | 2.7 |
| 5 $\mu$m step | Settling time [ms] | 188 | 146 |
| | RMS in-pos. error [nm] | 2.2 | 3.2 |

### 3.4.2 Circular tracking tests

During point-to-point positioning tests, it is observed that the stage with dither moves faster to the target position near the end of the motion command compared to the No dither case. This leads to smaller position errors in general at the start of the settling region. Therefore, it is suspected that the proposed VAN stage also has the potential of mitigating the undesirable effects of pre-motion friction during tracking motions.

To test our hypothesis, circular tracking tests with 5 mm and 5 $\mu$m radius and different tangential velocities are conducted. Since the NP stage of Figure 3.11 is a single-axis stage, without loss of generality, only the $x$-axis reference trajectories of the circular motions are utilized. The following cases are tested:

- No dither: no dither is applied; this represents a conventional mechanical-bearing-guided NP stage;
- Dither with HC: dither is applied with the proposed control scheme having the HC controller (see Figure 3.7); dithering input of 20 V peak-to-peak amplitude at 500 Hz is utilized.

Figure 3.19 shows the typical tracking performance obtained from the 5 mm radius circle test with 5 mm/s tangential velocity. The No dither case suffers for large position errors (with 1.67 $\mu$m peak error) at motion reversals due to the initially large stiffness of pre-motion friction. When dither is used with HC controller, the peak error is reduced to 1.49 $\mu$m, resulting in 11% reduction compared to the stage without dither. In the meantime, the RMS tracking error during one cycle of the circular motion is reduced by 9% as a result of the applied dither.

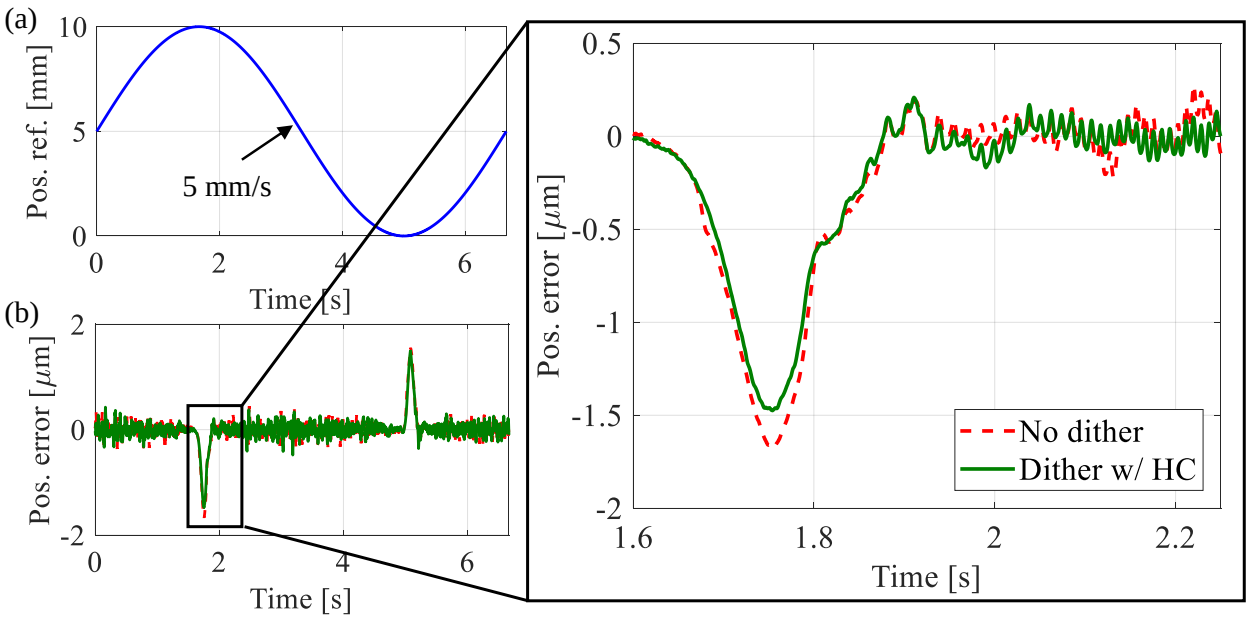


Figure 3.19 (a) *x*-axis position reference trajectory, and (b) tracking error of the stage during circle test with 5 mm radius and 5 mm/s velocity.

Figure 3.20 shows the typical tracking performance obtained from the circle test with 5 $\mu$m radius and 20 $\mu$m/s tangential velocity. In this case, the tracking error of the No dither case is sinusoidal in general, with small spikes at motion reversals. The Dither with HC case is able to effectively suppress these error spikes. However, as the error is dominated by the sinusoidal

motion, the stage with dither only achieves 14% reductions in both peak and RMS tracking errors, compared to the No dither case.

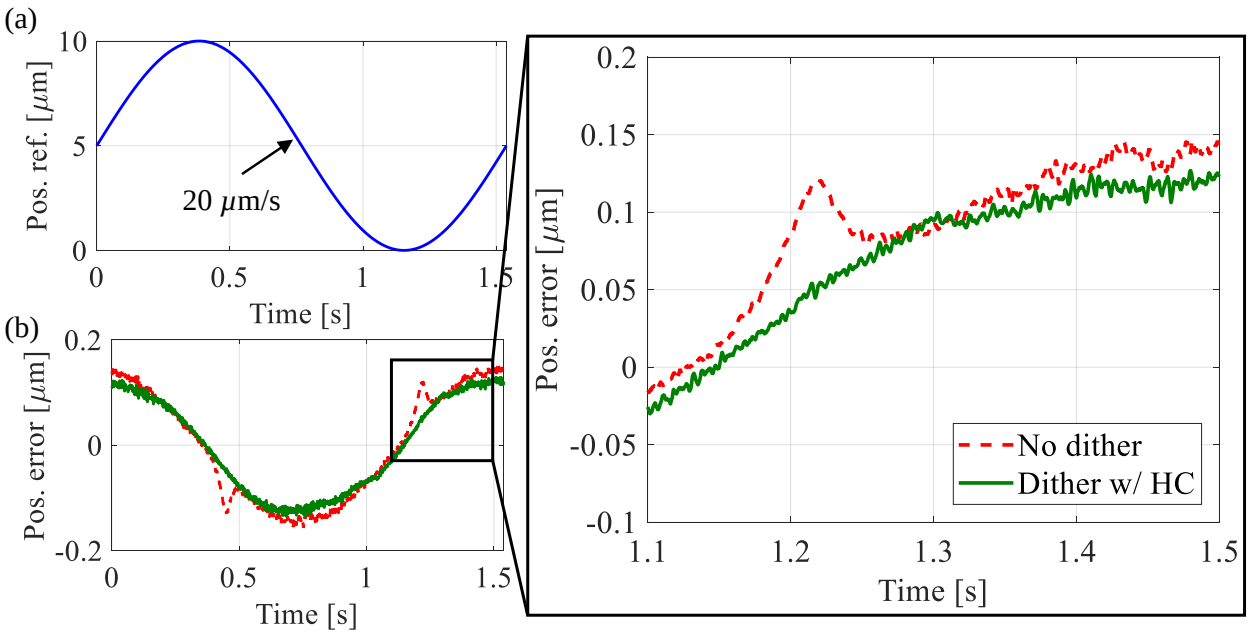


Figure 3.20 (a) *x*-axis position reference trajectory, and (b) tracking error of the stage during circle test with 5 $\mu$m radius and 20 $\mu$m/s velocity.

Figure 3.21 and Figure 3.22 summarize the percentage reductions in peak and RMS tracking errors achieved by Dither with HC case, relative to No dither case, for circular tracking tests with 5 mm and 5 $\mu$m radius and different velocities. It is observed that the stage with dither achieves up to 15 % reductions in terms of both peak and RMS errors.

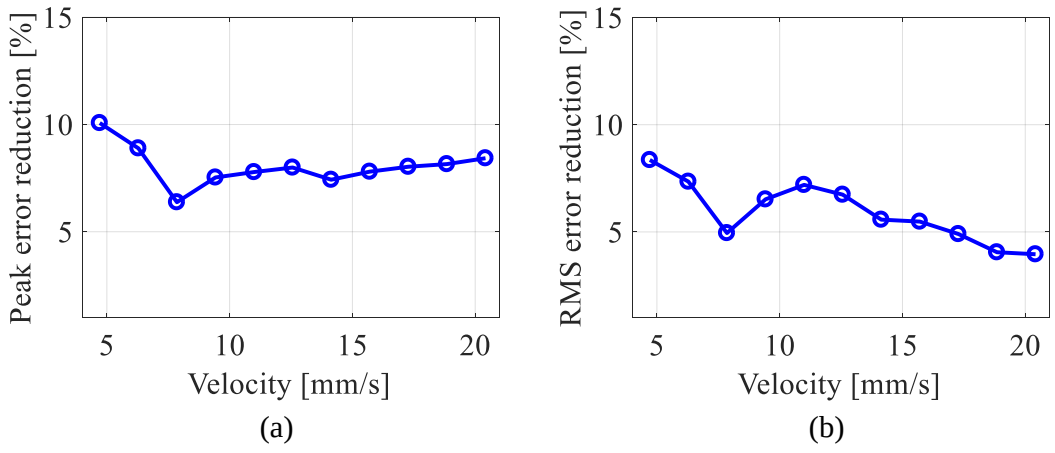


Figure 3.21 (a) Peak, and (b) RMS tracking error reductions achieved by Dither with HC case, compared to No dither case, during 5 mm circle tests with different velocities.

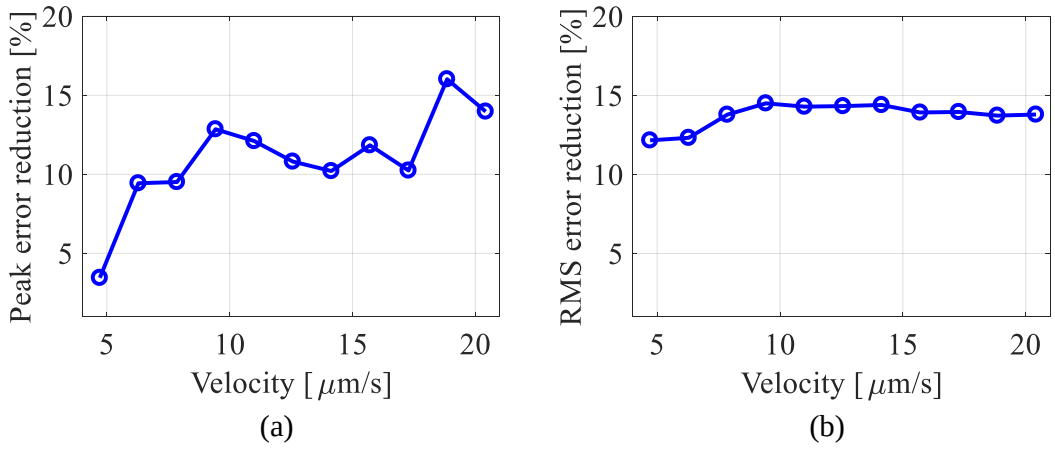


Figure 3.22 (a) Peak, and (b) RMS tracking error reductions achieved by Dither with HC case, compared to No dither case, during 5 $\mu$m circle tests with different velocities.

The relatively poor performance of the VAN approach during circular tracking motions may due to the fact that high frequency vibration is applied for the entire motion. Syamsul et al. have investigated the influence of dithering patterns on the tracking performance of the stage [127]. They have shown that an always-on dithering leads to marginal improvements in terms of both peak and RMS tracking errors. By modulating the amplitudes and oscillation patterns (i.e., waveform and duty cycle) of the applied dithering signal, they have achieved up to 30% improvements in the tracking performance [127]. However, the results are largely dependent on

the specific setup they have utilized for experiments and cannot be easily generalized to other systems. Moreover, a large number of experimental trials are needed for each circular command to obtain the optimal dithering pattern (e.g., amplitude, waveform and duty cycle), making it tedious and most importantly un-reliable to use in practice.

### 3.4.3 Remarks on heat and wear

As mentioned in Section 3.1, one worry about dither is its potential to generate heat and cause wear of mechanical components. Therefore, it is important to investigate the significance of these concerns for the proposed VAN approach. The power consumption ($P_{PZT}$) of a piezo stack actuator in sinusoidal operation can be approximated as [133]

$$P_{PZT} = f \cdot C_{PZT} \cdot V_{PP}^2 \tag{3.7}$$

where $C_{PZT}$ is the capacitance of the piezo actuator, $f$ is the operating frequency and $V_{pp}$ is the applied (peak-to-peak) voltage. The total power consumption of the two piezo stacks of the prototype VAN stage during point-to-point positioning tests can be calculated as 0.6 W (i.e., 0.3 W for each actuator). It is suggested that up to 10% of the electrical power is converted into heat [133], which is less than 0.06 W. In other words, only about 0.015 J of thermal energy is added to the stage, assuming each point-to-point motion ends in 250 ms.

Furthermore, Figure 3.23 shows the temperature of the table and piezo actuators, measured using thermocouples (Omega, type-K), for continuous dithering (at $V_{pp}$ = 20 V and $f$ = 500 Hz) over 30 minutes, starting from thermal equilibrium at room temperature. It can be seen that both piezo actuators heat up by about 0.2 °C, but the table temperature remains reasonably constant. This shows that the thermal impact of continuous dithering is negligible for the prototype stage. It is also worth mentioning that continuous dithering (e.g., for 30 minutes) is not necessary in many situations, like point-to-point positioning.

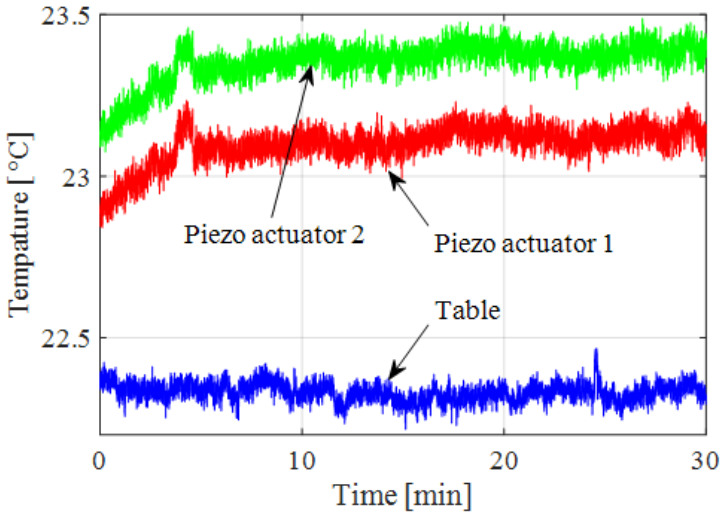


Figure 3.23 Temperature of the table and piezo actuators of the prototype VAN stage during continuous dithering at 20 V and 500 Hz for 30 minutes.

In order to evaluate the potential bearing wear caused by continuous dithering, the vibration amplitude of the linear ball bearing, which is approximately 2 $\mu$m based on the applied dithering signal of 20 V (see Figure 3.10), is used. The additional travel of the bearing caused by dither is calculated as 0.5 mm, assuming each point-to-point motion ends in 250 ms. This leads to 9% reduction of the bearings' service life, compared to the case without dither, during 5 mm step motions. Note that the nominal life of the linear ball bearing is calculated as more than 74,000 km using the equations provided by the bearing manufacturer [43]. This corresponds to over 14.8 billion 5 mm point-to-point motions or over 117 years continuous operation. Therefore, a 9% reduction in service life is a moot point in practice, especially considering the large increases in productivity that can be gained by reducing the settling times using VAN.

Things become tricky for the 5 $\mu$m step motions, since the implementation of dither causes a 100-time reduction of the bearing's service life. However, the 74,000 km nominal life of the bearing corresponds to 14.8 trillion of 5 $\mu$m point-to-point motions or over 117,326 years continuous operation. Therefore, even with a 100-time reduction, the bearing still has a service life of about 117 years. Although the use of VAN approach during 5 $\mu$m point-to-point motions may cause locally accelerated wear, it is not common to use the mechanical-bearing-guided NP stage for purely short stoke motions. In a more practical scenario where the VAN stage is used for a

combination of long range and short range motions, the potential bearing wear caused by continuous dithering is insignificant.

## 3.5 Chapter summary

In this chapter, a novel approach is presented for mitigating the friction-induced slow settling problem of mechanical-bearing-guided nanopositioning (NP) stages using high frequency vibration (or dither). The proposed method, called vibration assisted nanopositioning (VAN), synergistically combines mechanical design and control to allow dithering forces to be applied to a NP stage without causing excessive parasitic vibration, heat or wear. Specially, it proposes the use of two short stroke actuators (e.g., piezo or voice coil actuators), acting opposite to each other, to apply dithering forces directly to the mechanical bearings and hence, minimize unbalanced reaction forces due to dithering; the mechanical bearings are connected to the NP stage using compliant joints (e.g., flexure joints) to facilitate dithering. Moreover, it proposes a method for using a harmonic cancelling controller to compensate any residual parasitic vibration, caused by non-idealities in the mechanical (and electrical) design of the stage. Simulations are used to demonstrate VAN's potential for superior performance and robustness.

A prototype VAN stage is designed and built based on the proposed concept. Experiments conducted using the designed prototype stage demonstrate 66% and 22% reductions in mean settling time during 5 mm and 5 $\mu$m point-to-point positioning motions, respectively, based on 50 random trials. The additional heat and potential bearing wear caused by dither are shown to be insignificant in practice. Circular tracking tests with different radii and tangential velocities show that the proposed VAN approach slightly reduces the peak and RMS tracking errors (up to 15%), compared to the case without dither. Though it is possible to further improve the tracking accuracy of the VAN approach by regulating the dithering patterns (e.g., amplitude, waveform and duty cycle), it is not robust to use such methods in practice due to the need for a large number of experimental trials to optimize the operating condition.

# Chapter 4

## Friction Isolator

The vibration assisted nanopositioning (VAN) discussed in Chapter 3 achieves significant reductions in the settling time of mechanical-bearing-guided nanopositioning (NP) stage while maintaining nanometer-level positioning precision. Although simpler and cheaper than the existing coarse-fine arrangements, the need for additional piezo actuators and voltage amplifiers could also limit the practicality of the VAN approach. Therefore, friction isolator (FI), which is simpler and more cost-effective compared to VAN and coarse-fine arrangement, is proposed for mitigating the undesirable effects of pre-motion friction. In Section 4.1, the principle behind the proposed FI is presented. Section 4.2 discusses the design of a FI prototype that achieves low stiffness in the motion direction without overly sacrificing stiffness in off-axis directions. The benefits of FI on the PID-type controller is shown through frequency domain analysis in Section 4.3. Finally, the performance of FI is evaluated using point-to-point positioning tests and circular tracking tests in Section 4.4.

This chapter is partially based on the following publications:

- Dong X, Liu X, Yoon D, Okwudire CE. *Simple and robust feedforward compensation of quadrant glitches using a compliant joint*. CIRP Annals-Manufacturing Technology. 2017; 66(1):353–356.
- Dong X, Okwudire CE. *Detailed experimental evaluation of the compliant joint method for feedforward compensation of pre-motion friction*. 32rd Annual Meeting of American Society for Precision Engineering. 2017.
- Dong X, Okwudire CE. An experimental investigation of the effects of the compliant joint method on feedback compensation of pre-sliding/pre-rolling friction. Precision Engineering. 2018; 54:81–90.
- Dong X, Yoon D, Okwudire CE. *Axially compliant bearing for precision positioning*. Patent Filing # PCT/US2016/060033. Filed November 2, 2016. (Pending)

## 4.1 Concept of friction isolator

Figure 4.1 shows the concept of the friction isolator (FI) for mitigating the undesirable effects of pre-motion friction (compared to Figure 1.6 in Section 1.3). As discussed in Section 1.3, pre-motion friction is modeled as an equivalent spring of stiffness $k_f$ connecting the bearing to the ground [48]-[50][55][56]. When the NP stage starts from rest (or after motion reversals), $k_f$ rapidly decreases from its initially large value and eventually becomes zero, such that friction enters the gross motion regime [46][49][52]. The large stiffness and highly nonlinear dynamics of pre-motion friction pose great challenges to the PID-type controllers, resulting in severely diminished positioning speed and precision [48][49][62]-[65]. In the proposed FI approach, rather than being rigidly attached to the moving table of the stage, the bearing is attached using a joint of stiffness $k_{fi}$ in the motion direction. As a result, the friction-isolated NP stage (i.e., the stage with FI) is modeled statically as a series combination of $k_f$ and $k_{fi}$ with combined stiffness

$$k_c = \frac{k_f \times k_{fi}}{k_f + k_{fi}} \tag{4.1}$$

Note that the bearing mass is neglected in the spring model for the following quasi-static stiffness analysis. A very small $k_{fi}$ dominates the combined stiffness felt by the feedback controller when $k_f$ is very large in the pre-motion regime; that is $k_c \to k_{fi}$ even when $k_f \to \infty$. Therefore, if $k_{fi} << k_f$, the PID-type feedback controller can easily suppress the equivalent frictional disturbance without using very high gains, potentially leading to large reductions of settling times and errors during point-to-point positioning and tracking motions, respectively.

Moreover, the sensitivity of the combined stiffness $k_c$ to variations in $k_f$ is given by

$$\kappa = \frac{\partial k_c}{\partial k_f} = \left( \frac{\eta}{1+\eta} \right)^2 ; \text{ where } \eta = \frac{k_{fi}}{k_f} \tag{4.2}$$

Note that if $k_{fi} << k_f$, $\eta \to 0$, and the sensitivity of $k_c$ to variations in $k_f$ becomes very small. This indicates that if model-based friction compensation (e.g., feedforward friction compensation) is performed using $k_c$ instead of $k_f$, the adverse effects of errors in $k_f$, due to low-fidelity friction

modeling or variations of friction are diminished. Therefore, if $k_{fi} << k_f$ and $k_{fi}$ is precisely known, accurate and robust feedforward compensation can be achieved even when a significant amount of error exists in $k_f$.

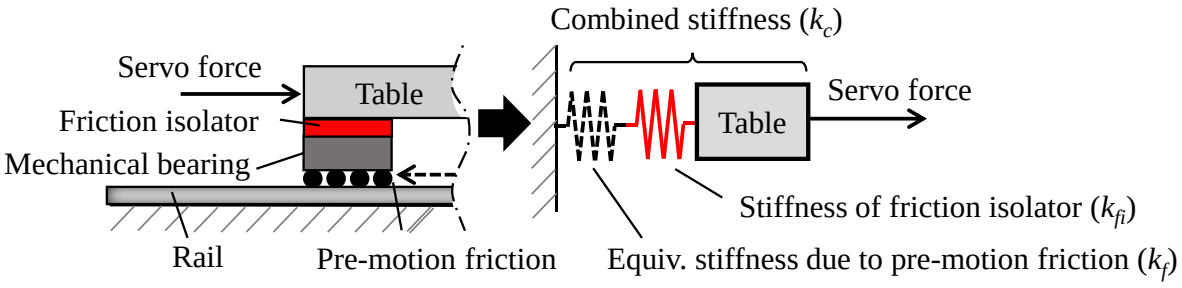


Figure 4.1 Schematic of a NP stage with mechanical bearing attached to the moving table using a friction isolator (FI).

## 4.2 Design of a friction isolator prototype

For the purposes of experimentally validating the above-discussed benefits of FI, a FI prototype for the in-house built NP stage of Section 3.3 (see Figure 3.11) is designed as one possible realization of the proposed concept. As seen from Figure 4.2, the designed FI prototype, whose design is discussed in the rest of this section, is used to attach each bearing to the moving table of the stage. Based on the requirement that $k_{fi} << k_f$, the FI must have orders of magnitude less stiffness than the initial contact stiffness of pre-motion friction experienced by each bearing in the motion (i.e., axial) direction. However, the isolator must also maintain the same order of magnitude of off-axis stiffness (in lateral and vertical directions) as the bearing, so as not to unduly compromise the rigidity of the stage.

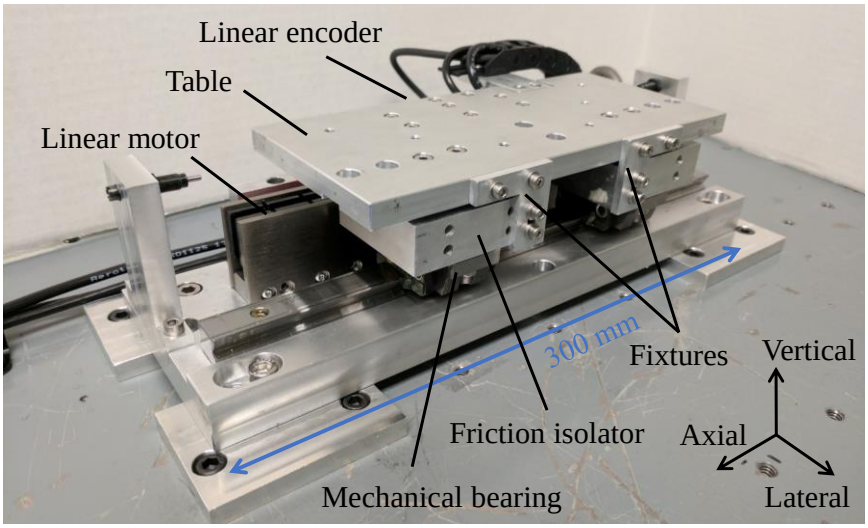


Figure 4.2 The in-house built mechanical-bearing-guided NP stage equipped with the designed FIs. The linear encoder is mounted on the distal side of the table and the fixtures are used to de-activate the FIs.

As shown in Figure 4.3(a), flexure hinges (or flexures, for short) are adopted for the designed FI prototype because of their non-contact and friction-free nature. The outer platform of the flexure is connected to the bearing and the center platform is connected to the table. The stiffness of flexure is coupled in all directions. Therefore, it is challenging to get very low stiffness in the axial direction without overly compromising off-axis stiffness (in lateral and vertical directions). A double parallelogram configuration with an intermediate platform is utilized to connect the center and outer platforms of the flexure to help reduce its axial stiffness. Moreover, the positive stiffness of the flexure is combined in parallel with a negative stiffness mechanism to keep the net axial stiffness positive, but smaller than that of the flexure alone. As highlighted in Figure 4.3(b), the negative stiffness mechanism is realized using a pair of repelling permanent magnets (PMs) attached to the center and intermediate platforms of the flexure. Given relative motion $\lambda$ from the equilibrium position, the PM pair is repelled further apart from each other. Note that eight N42 grade NdFeB PM blocks (each of dimension 1/2" × 1/8" × 1/16") are used to construct opposing halves of the PM pair. As shown by north-pole-pointing arrows in Figure 4.3(b), the blocks are arranged with alternating polarity to increase the repulsion force (hence the negative stiffness) of the PM pair. Figure 4.3(c) shows the manufactured FI prototype. It is manufactured from Aluminum 7075-T6 using wire electric discharge machining (EDM).

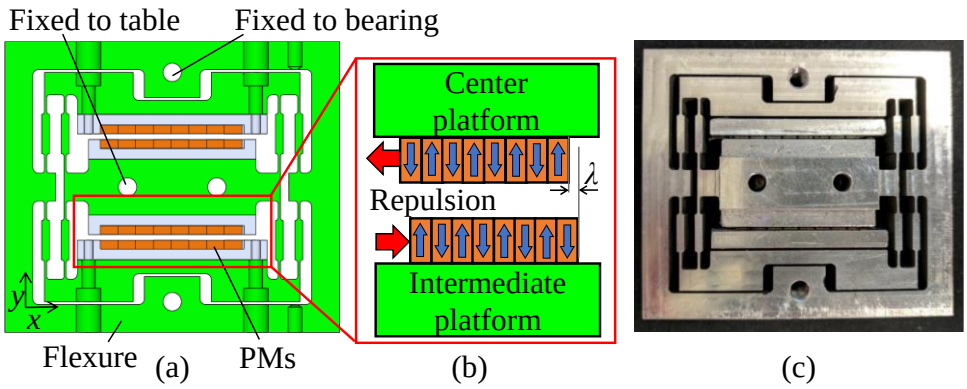


Figure 4.3 (a) CAD model of the designed FI, (b) negative stiffness mechanism with repelling permanent magnets (PMs), and (c) manufactured FI prototype.

Table 4.1 Designed stiffness values of FI, bearing and their combination [N/m].

| | Axial | Vertical | Lateral |
|---|---|---|---|
| Flexure | $9 \times 10^4$ | $3 \times 10^7$ | $3 \times 10^7$ |
| PMs | $-5 \times 10^4$ | $-2 \times 10^4$ | $2 \times 10^5$ |
| FI (PMs + flexure) | $4 \times 10^4$ | $3 \times 10^7$ | $3 \times 10^7$ |
| Bearing | $\sim 10^6$ | $6 \times 10^7$ | $2 \times 10^7$ |
| Combined (FI + bearing) | $\sim 4 \times 10^4$ | $2 \times 10^7$ | $1 \times 10^7$ |

Table 4.1 summarizes the stiffness values of the designed flexure and PMs of Figure 4.3 (obtained via finite element analysis using SolidWorks® and COMSOL®), together with the total stiffness of the FI. Notice that the addition of the PMs reduces the axial stiffness of the FI by more than 50% compared to the flexure alone, with virtually no change to its vertical and lateral stiffness. Table 4.1 also provides the stiffness values of each bearing. The vertical and lateral stiffness values are obtained from the bearing catalog [43]; the reported axial stiffness represents an order-of-magnitude estimation of the bearing's initial frictional stiffness, based on experiments (as explained in Section 4.4.3). Notice that the axial stiffness of the FI is two orders of magnitude less than, while the vertical and lateral stiffness values are of the same order of magnitude as that of the bearing. The combined stiffness of the bearing and FI are computed as shown in the table. The combined axial stiffness is virtually the same as that of the FI, showing that the FI stiffness is

dominant. Observe also that the combined vertical and lateral stiffness values are of the same order of magnitude as those of the bearing, meaning that off-axis rigidity is not overly compromised.

The particular design of the FI prototype shown in Figure 4.3 may introduce Abbe errors [136] to the in-house built NP stage of Figure 4.2. These issues are not addressed in this dissertation since they are not relevant to evaluating the performance of the proposed method. However, they can be resolved by standard precision engineering approaches, such as embedding the FI into a pocket in the moving table to reduce the overall profile of the NP stage.

## 4.3 Frequency domain evaluation of friction-isolated nanopositioning stage

Frequency domain analysis is conducted to evaluate the effects of friction isolator on the servo-controlled NP stage. Figure 4.4 shows the measured frequency response functions (FRFs) of the plant dynamics (i.e., from input motor force to output table displacement) for the stage with and without FI. Note that FIs can be de-activated by installing the fixtures shown in Figure 4.2 to lock the table rigidly to the bearing, such that the resulting system is equivalent to a conventional mechanical-bearing-guided NP stage (i.e., No FI case).

Each FRF is obtained by applying constant-amplitude sinusoidal motor current commands with varying frequencies to the linear motor and recording the corresponding output displacement magnitudes of the table's position using the linear encoder. The motor currents are scaled by a force constant of 11 N/A to convert them to equivalent motor forces. It is well known that, in the presence of pre-motion friction, FRFs of the system can vary significantly, depending on the excitation amplitudes [50][53]-[55][60]. Therefore, to demonstrate the effects of pre-motion friction on the stage with and without FI, the FRFs are generated using input force amplitudes varying from 0.11 N to 16.5 N (via motor current amplitudes varying from 0.01 A to 1.5 A, respectively). When the input amplitude is very small, motion of the No FI case is also very small due to the initially large stiffness of pre-motion friction after each motion reversal. As a result, the measured plant dynamics behaves as a standard spring-mass system (as shown in Figure 1.6) with one dominant low frequency resonance induced by the large frictional stiffness. As the input amplitude increases, the frictional stiffness gradually decreases, causing the friction-induced resonance to shift to lower frequencies [50][53]-[55], indicating a gradual transition of friction from pre-motion to gross motion regime. In the meantime, the motion of the stage without FI also increases as indicated by larger DC (low frequency) gains of the FRF. Eventually, at the highest

input amplitude, the No FI case experiences pure gross motion friction and the friction-induced low frequency resonance disappears from the measured FRFs. Notice that the high frequency dynamics of the No FI case are also greatly affected by the variations of pre-motion friction. For example, the magnitude/phase and resonance frequency of the mode around 400 Hz vary significantly due to its proximity to, and interactions with, the friction-induced resonance of the stage. Therefore, in agreement with the literature [50][53]-[55], the plant dynamics of the No FI case show large variations (nonlinearities) in both low and high frequency regions with changing input force magnitudes, posing significant challenges for the feedback controller [48][49][62]-[65].

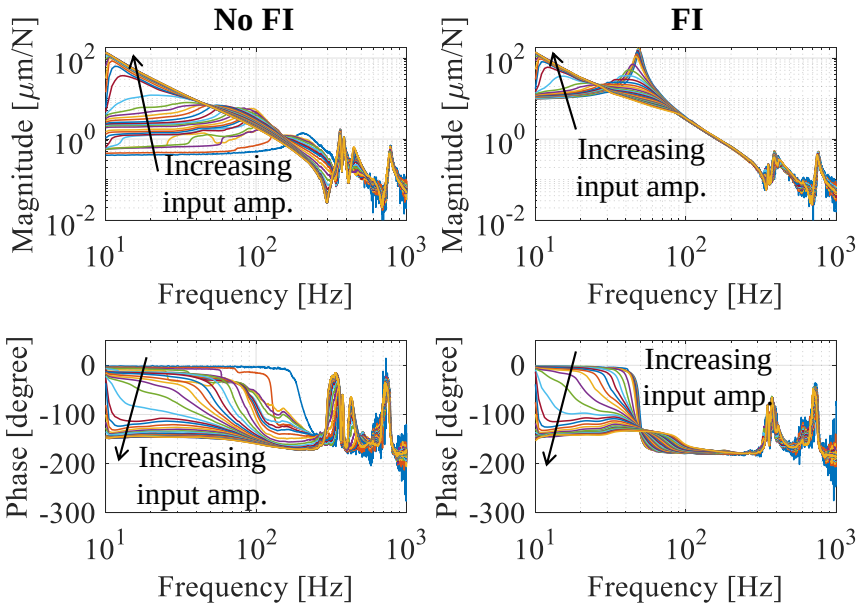


Figure 4.4 Frequency response functions (FRFs) of open loop plant dynamics for the stage with (i.e., FI case) and without (i.e., No FI case) friction isolator using different input amplitudes.

Since the axial stiffness of FI is designed to be much (orders of magnitude) smaller than the initially large stiffness of pre-motion friction (see Table 4.1), the combined spring stiffness (in series) experienced by the stage with FI at very small input amplitude is dominated by FI stiffness. This can be seen from Figure 4.4; with the same input amplitudes applied to the stage, the friction-induced resonance frequencies of the FI case are much lower, and its DC gains are much higher, compared to those of the No FI case. As the input force amplitude increases, the FRFs of the stage

with FI experience similar transitions as the stage without FI, however with less variations of the magnitude/phase and friction-induced resonance frequency. Moreover, the higher frequency dynamics of the FI case (e.g., the mode at 400 Hz) are virtually not affected by the changing frictional stiffness, since the friction-induced resonance of the stage with FI occurs at much lower frequencies (below 50 Hz). As a result, the FI case shows smaller net stiffness and variations (nonlinearities) in the measured plant FRFs, and the variations mainly occur at low frequencies (i.e., less than 100 Hz).

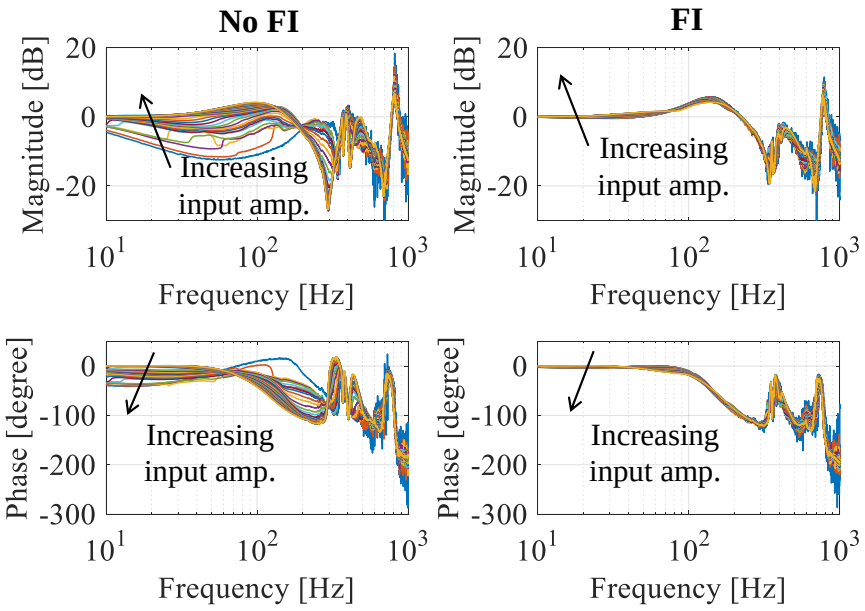


Figure 4.5 Frequency response functions (FRFs) of closed loop dynamics for the stage with (i.e., FI case) and without (i.e., No FI case) friction isolator using different input amplitudes.

An industry-standard PID controller is used to control the stage. It is implemented using a real-time control board (dSPACE, DS1007) running at 10 kHz sampling frequency. The PID controller is tuned to around 200 Hz closed loop bandwidth, using loop shaping, based on an FRF of the stage without FI in the gross motion friction regime (i.e., using the 1.5 A-input plant FRF of the No FI case in Figure 4.4). The exact same PID gains are used for controlling the stage with FI. Figure 4.5 shows the measured closed loop dynamics (from desired to actual position) of the No FI and FI cases using the PID controller. Because the controller is tuned based on the gross-motion-regime plant dynamics, it encounters difficulties in overcoming the large frictional

stiffness of the stage without FI in the pre-motion friction regime. This leads to significant drops of the closed loop FRF magnitudes (below 0 dB) at low frequency regions when the input amplitude is small and pre-motion friction dominates. As a result, the –3 dB closed loop bandwidth of the No FI case is reduced from its original 200 Hz in the gross motion regime to less than 10 Hz in the pre-motion regime as shown in Figure 4.6(a). In other words, when the stage without FI starts from rest, e.g., during motion reversals in tracking motions, or after overshoots in the vicinity of a target position in point-to-point positioning motions, the closed loop bandwidth is reduced to less than 10 Hz. This causes large position errors and sluggish settling performance, as discussed in Section 1.3 and demonstrated in experiments using the in-house built NP stage in Section 3.4. To overcome this shortcoming, PID gains must be increased to improve the closed loop bandwidth in the pre-motion regime [48][62][63]. However, such high gain controller makes the conventional mechanical bearing stage to be prone to instability, sensitivity to sensor noise, integrator wind-up, chattering and limit cycles, all of which are very detrimental to its performance [49][64], as shown in Appendix A.

Compared to the No FI case, the same PID controller applied to the stage with FI experiences much less difficulties and performance variations between the pre-motion and gross motion regimes of friction (see Figure 4.5). This is because the nonlinearity in the plant dynamics of the FI case mainly occurs at low frequency regions. In the presence of a feedback controller, the nonlinearity is effectively suppressed through a phenomenon known as "feedback linearization" [137]. In other words, since the equivalent frictional stiffness experienced by the stage with FI is much smaller and less variable, the feedback controller can better overcome and regulate the disturbance force originated from it. Therefore, a conservatively-tuned PID controller (from the stand-point of the stage without FI) acts as a "high gain" feedback controller for the stage with FI, leading to more consistent and much improved closed loop bandwidth for both pre-motion and gross motion regimes of friction, as shown in Figure 4.6(a).

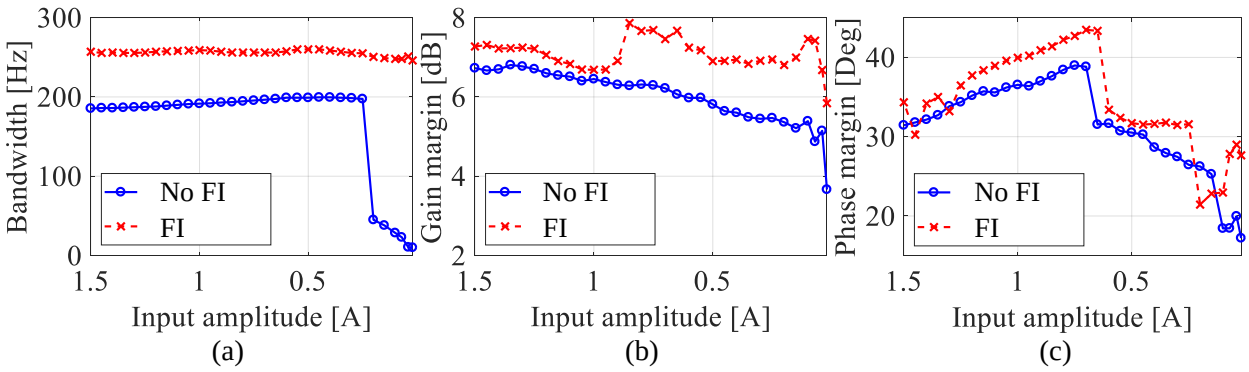


Figure 4.6 Calculated (a) closed loop bandwidth (based on –3 dB criterion), (b) gain, and (c) phase margins of the stage with and without FI using the same PID controller.

Figure 4.6 also shows the calculated gain and phase margins of the stage with and without FI using different input amplitudes. It is assumed that each measured FRF of the stage (at a given input amplitude) represents a linear-time-invariant (LTI) system. This is essentially equivalent to linearizing the nonlinear plant at different operating points (i.e., different pre-motion frictional stiffness values). Although local stability of the linearized systems does not guarantee the global stability of the nonlinear system, the stability of the individual LTI systems can be used as an indicator of the stability of the stage with and without FI at various operating points. For example, it is observed that stability margins of both stages are always positive, showing that each individual LTI system is indeed stable. Moreover, the stage with FI maintains similar or even slightly better stability margins (robustness) while achieving much higher closed loop bandwidth, compared to the stage without FI. This is mainly due to less interactions between the friction-induced resonance and the high frequency dynamics of the FI case, compared to the No FI case.

## 4.4 Experimental validation

The performance of the FI prototype is experimentally evaluated using the same point-to-point positioning tests and circular tracking tests from Section 3.4. Note that the same PID controller (tuned in Section 4.3) is used for the stage with and without FI. Model-based feedforward compensation of pre-motion friction is also conducted to evaluate the potential benefits (in terms of performance and robustness) of the proposed FI approach, as discussed in Section 4.1.

### 4.4.1 Point-to-point positioning tests

Point-to-point motion profiles with 5 mm and 5 $\mu$m step sizes are used as the reference trajectories (see Section 3.4.1) and the time for the stage to settle into a ±25 nm window during the settling portion is evaluated for the following cases:

- No FI: the in-house built mechanical-bearing-guided NP stage of Figure 4.2; note that fixtures are implemented to de-activate the FIs.
- FI: the in-house built mechanical-bearing-guided NP stage of Figure 4.2 with the designed FI prototypes.

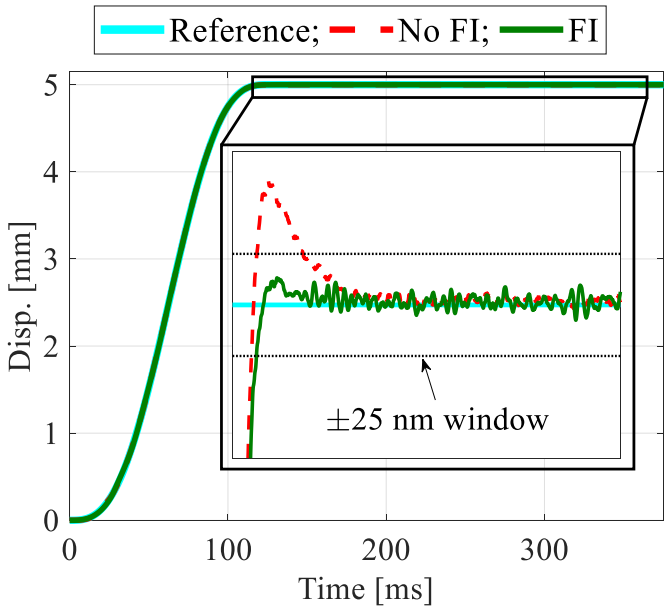


Figure 4.7 Typical settling performance of the stage with and without FI into the ±25 nm window during 5 mm point-to-point motion. The black box shows the settling portion.

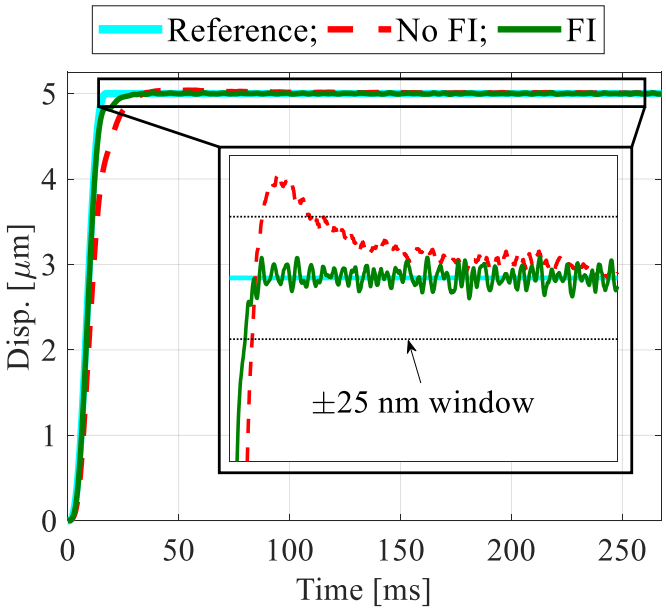


Figure 4.8 Typical settling performance of the stage with and without FI into the ±25 nm window during 5 $\mu$m point-to-point motion. The black box shows the settling portion.

Figure 4.7 and Figure 4.8 compare the typical settling performance of the stage with and without FI during 5 mm and 5 $\mu$m point-to-point positioning tests. For the 5 mm step motions, the No FI case takes 45 ms to settle into the ±25 nm window, with an RMS in-position error of 1.6 nm. Thanks to the reduced equivalent frictional stiffness brought about by the introduction of FI, the same PID controller is able to better suppress the disturbance during the settling region, reducing the settling time to 15 ms. However, as the FI replaces the stiff frictional spring with the much softer combined stiffness, the stage is more prone to noise from servo motor drive during in-position. As a result, the FI case suffers from a significantly increased RMS in-position error of 2.7 nm. Similarly, for the 5 $\mu$m step motion, the stage with FI achieves 83% reduction of the settling time, at the cost of 93% increase in RMS in-position error.

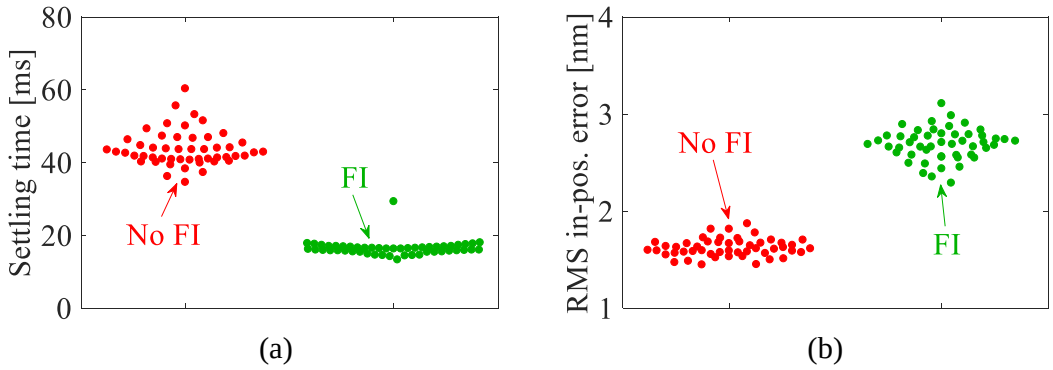


Figure 4.9 Comparison of (a) settling time into the ±25 nm window, and (b) RMS in-position error during 50 trials of 5 mm point-to-point motions.

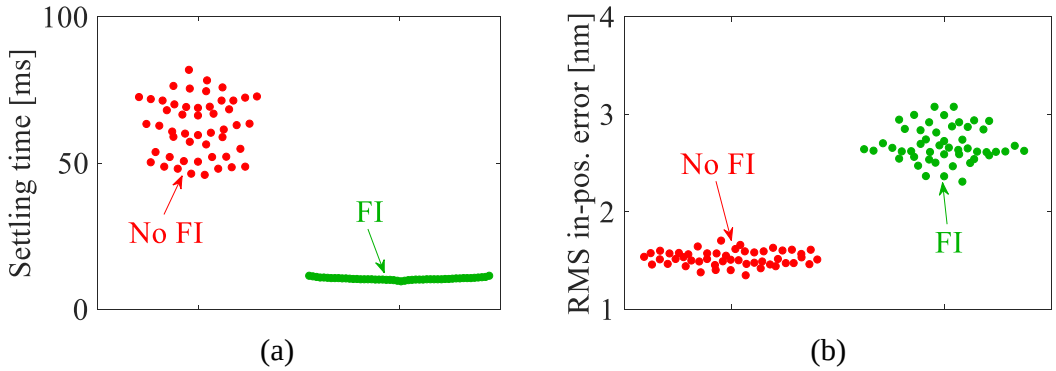


Figure 4.10 Comparison of (a) settling time into the ±25 nm window, and (b) RMS in-position error during 50 trials of 5 $\mu$m point-to-point motions.

Figure 4.9 and Figure 4.10 compare the settling time and in-position stability during 5 mm and 5 $\mu$m point-to-point positioning tests, based on 50 trials at random positions of the table and Table 4.2 summarizes the mean settling time and RMS in-position error. The mean settling times of the No FI case are 44 ms and 62 ms for the 5 mm and 5 $\mu$m steps, respectively. The FI case achieves 63% and 84% reductions in the mean settling times; however, at the costs of 66% and 77% increases of the RMS in-position errors, compared to the No FI case.

Table 4.2 Comparison of mean settling time and in-position error (RMS) during 50 trials of 5 mm and 5 $\mu$m point-to-point motions.

| | | No FI | FI |
|---|---|---|---|
| 5 mm step | Settling time [ms] | 44 | 16 |
| | RMS in-pos. error [nm] | 1.6 | 2.7 |
| 5 $\mu$m step | Settling time [ms] | 62 | 10 |
| | RMS in-pos. error [nm] | 1.5 | 2.7 |

### 4.4.2 Circular tracking tests

Circle tests with 5 mm and 5 $\mu$m radius and different tangential velocities are conducted to evaluate the tracking performance of the proposed FI. Similar to Section 3.4.2, only the *x*-axis reference trajectories of the circular motions are utilized to test the following cases:

- No FI: the in-house built mechanical-bearing-guided NP stage of Figure 4.2; note that fixtures are implemented to de-active the FIs.
- FI: the in-house built mechanical-bearing-guided NP stage of Figure 4.2 with the designed FI prototypes.

Figure 4.11 compares the typical tracking performance of the stage with and with FI, obtained from the 5 mm radius circle test with 5 mm/s tangential velocity. The No FI case suffers from large peak error (of 3.59 $\mu$m) at motion reversals due to the initially large stiffness of pre-motion friction. In the presence of FI, the PID controller can better suppress the less stiff combined stiffness $k_c$, leading to a significantly reduced peak error of 2.33 $\mu$m (35% reduction). As a result of the reduced peak error, the stage with FI also achieves 16% reduction in terms of the RMS tracking error during one cycle of the circular motion.

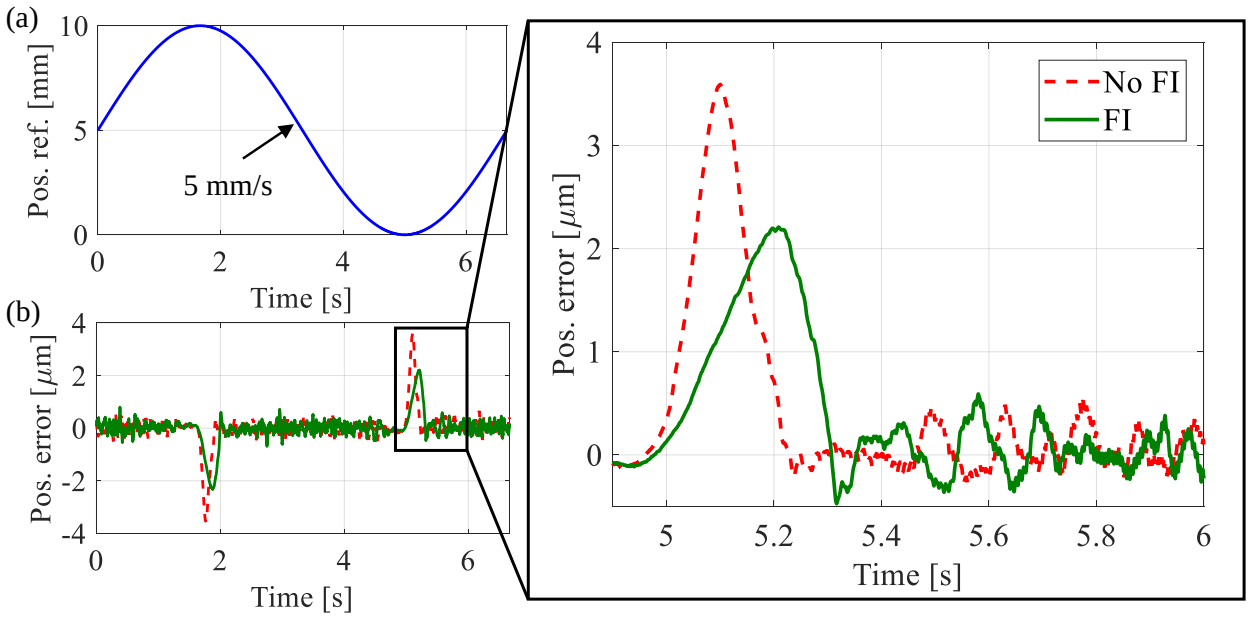


Figure 4.11 (a) *x*-axis position reference trajectory, and (b) tracking error of the stage during circle test with 5 mm radius and 5 mm/s velocity.

Figure 4.12 shows the typical tracking performance obtained from the 5 $\mu$m radius circle test with 20 $\mu$m/s tangential velocity. During the short stroke motion, pre-motion friction dominates the stage with and without FI, showing characteristics of a standard spring-mass system (see Figure 1.6 and Figure 4.1). Since the stiffness of FI is much smaller than that of the pre-motion frictional stiffness, the stage with FI behaves very similar to a flexure-based NP stage. As a result, the FI case achieves 68% and 73% reductions of the peak and RMS tracking error, compared to the No FI case.

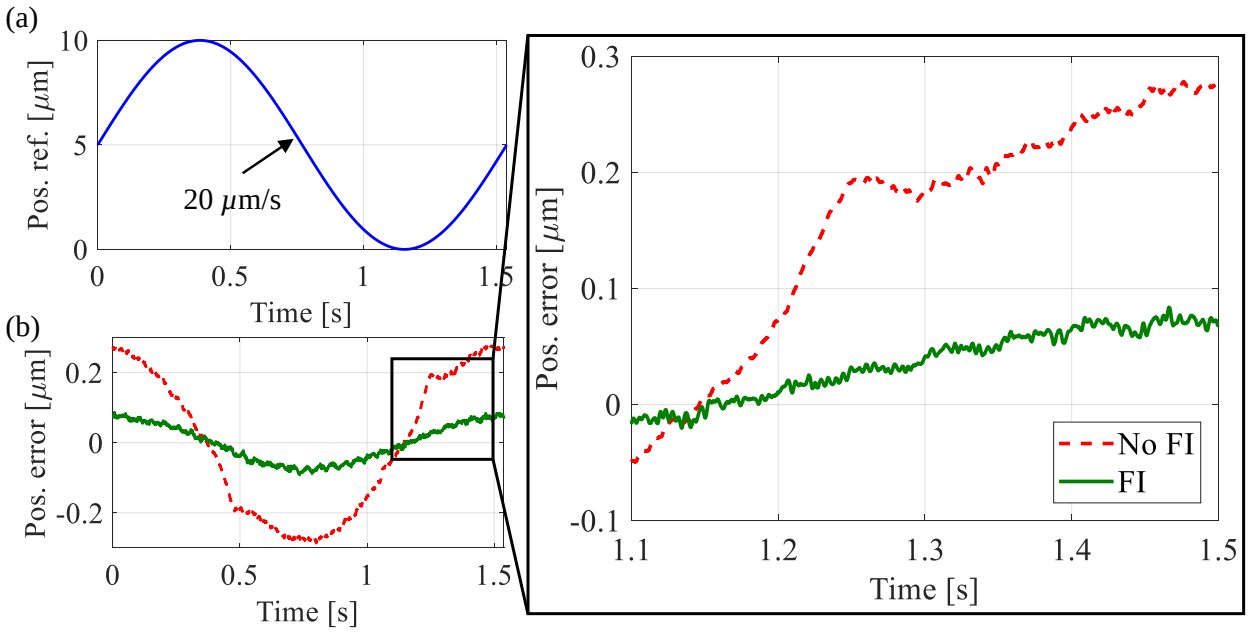


Figure 4.12 (a) *x*-axis position reference trajectory, and (b) tracking error of the stage during circle test with 5 $\mu$m radius and 20 $\mu$m/s velocity.

Figure 4.13 and Figure 4.14 summarize the percentage reductions in peak and RMS tracking errors achieve by the FI case, relative to the No FI case, for circular tests with different radii and velocities. It is observed that the stage with FI achieves up to 70% and 75% reductions in the peak and RMS tracking errors, respectively.

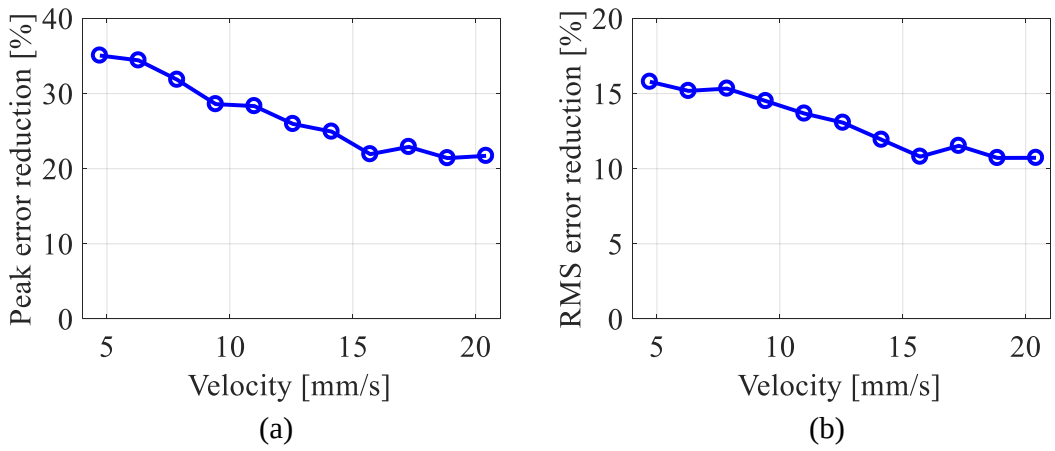


Figure 4.13 (a) Peak, and (b) RMS tracking error reductions achieved by the FI case, compared to the No FI case, during 5 mm circle tests with different velocities.

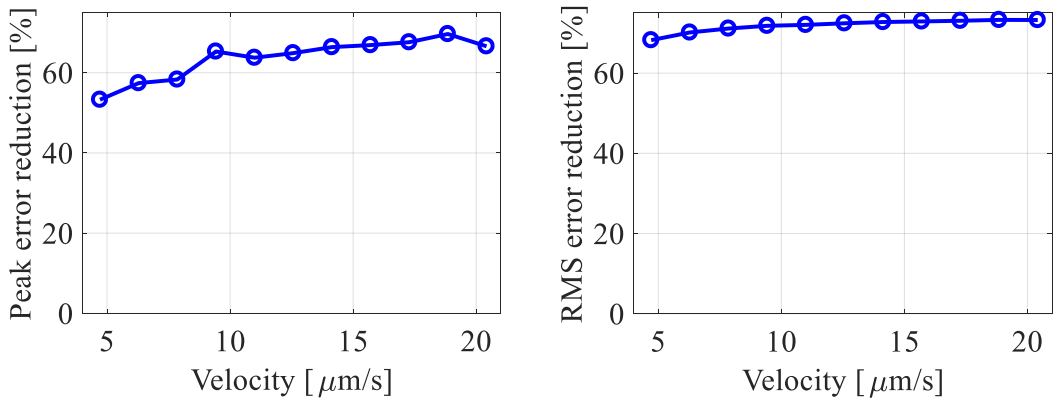


Figure 4.14 (a) Peak, and (b) RMS tracking error reductions achieved by the FI case, compared to the No FI case, during 5 $\mu$m circle tests with different velocities.

### 4.4.3 Circular tracking tests with model-based feedforward friction compensation

As discussed in Section 2.2, model-based feedforward (FF) compensation is often utilized to mitigate the undesirable effects of pre-motion friction during tracking applications [14][56][71]-[74]. Tracking accuracy of the mechanical-bearing-guided NP stage can be greatly improved with FF compensation if the friction model employed is accurate enough [55][66][75]. However, this often requires the use of complex friction models whose parameters cannot be easily identified [55]. Moreover, FF compensators with both simple and complex models of pre-motion friction are not robust to on-machine friction changes that frequently occur as a function of time and/or stage's position [14][77][78]. Therefore, they need frequent re-calibration or adaptation, which hampers their practicality [81].

As shown in Eq. (4.2), the sensitivity of the combined stiffness $k_c$ to variations in pre-motion frictional stiffness $k_f$ becomes very small if the stiffness of FI, $k_{fi}$ is much smaller than $k_f$. That is to say, if model-based FF friction compensation is performed using $k_c$ instead of $k_f$, the adverse effects of errors in $k_f$, due to low-fidelity friction modeling or variations of friction are diminished. Therefore, if $k_{fi} << k_f$ and $k_{fi}$ is precisely known, accurate and robust compensation can be achieved even when a significant amount of error exists in $k_f$. To test this hypothesis, FF compensation of pre-motion friction on the in-house built NP stage of Figure 4.2 is carried out, for the case with and without FI. Figure 4.15 shows the block diagram of the control scheme with a

PID feedback controller and model-based FF friction compensator. Two popular pre-motion friction models are implemented in the FF compensator, namely the Dahl [46] and generalized Maxwell-slip (GMS) models [51][76].

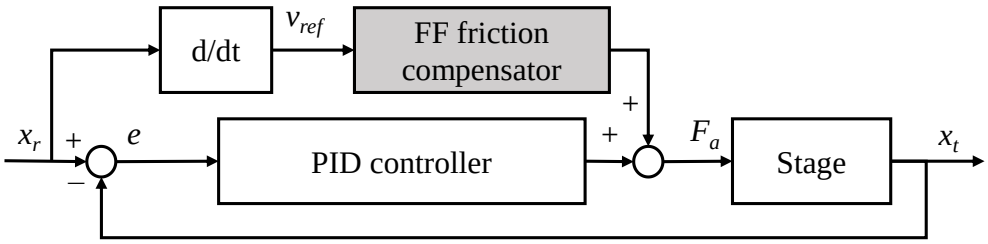


Figure 4.15 Block diagram of the control scheme with PID controller and model-based feedforward (FF) friction compensator.

The Dahl friction model [46][138] is the simplest model that predicts the spring-like characteristic of pre-motion friction. By setting the shape factor, $\upsilon$, in Eq. (1.1) to one, the Dahl model can be written as

$$F_f = k_\sigma z; \quad \frac{dz}{dx} = \dot{x}_t \left( 1 - \frac{F_f}{F_C} \operatorname{sgn} \dot{x}_t \right) \tag{4.3}$$

where $F_f$ is the force of friction, $k_\sigma$ is the initial contact stiffness of pre-motion friction, $F_C$ is the Coulomb friction force, $x_t$ is the position of the moving table and $z$ is an internal state of frictional dynamics. As discussed in Section 1.3, at motion reversals, the stiffness of pre-motion friction starts at $k_f = k_\sigma$ and reduces to $k_f = 0$ as $F_f$ approaches $F_C$, and gross motion begins.

The Dahl model parameters for the stage without FI are identified using the frequency domain approach discussed by Hensen et al. [139]. The open loop frequency response function (FRF), between servo actuation force, $F_a$, and table displacement, $x_t$, that is obtained via sine sweep using a very small force amplitude (0.11 N) is utilized (see Figure 4.4). The frequency of the dominant resonance due to pre-motion friction (i.e., friction-induced resonance) is extracted from the FRF and used to calculated the initial contact stiffness of the No FI case ($k_{\sigma,NoFI}$) based on the simple spring-mass model shown in Figure 1.6. The axial stiffness $k_{fi}$ of the FI is identified using the same technique, applied to the stage with FI (see Figure 4.4); $k_{fi}$ and $k_{\sigma,NoFI}$ are then combined

in series to obtain $k_{\sigma,FI}$ (see Eq. (4.1)), the equivalent initial frictional stiffness of the FI case, assuming the quasi-static model shown in Figure 4.1. $F_C$ is determined from the constant force required to sustain gross motion. The identified parameters of the Dahl model are summarized in Table 4.3. Notice that $k_{\sigma,FI}$ is dominated by $k_{fi}$, and is about two orders of magnitude lower than $k_{\sigma,NoFI}$.

Table 4.3 Identified FI stiffness and Dahl friction model parameters.

| $F_C$ [N] | $k_{fi}$ [N/m] | $k_{\sigma,NoFI}$ [N/m] | $k_{\sigma,FI}$ [N/m] |
|---|---|---|---|
| 5.31 | $8.27 \times 10^4$ | $2.19 \times 10^6$ | $8.08 \times 10^4$ |

Due to the limited tuning parameters, Dahl model often fails to accurately capture the complex dynamics of pre-motion friction [55][75]. For this reason, complex models like the generalized Maxwell-slip (GMS) model [51][76] have been developed. The GMS model consists of $N$ elementary (massless) blocks and springs connected in parallel. The behavior of each elementary block is determined by two states (i.e., stick or slip) and is represented by

$$F_f = \sum_{i=1}^{N} f_i; \quad \frac{df_i}{dt} = \begin{cases} k_i \dot{z}, \text{ if stick (i.e., } f_i < \alpha_i F_C) \\ 0, \text{if slip (i.e., } f_i = \alpha_i F_C) \end{cases}; \quad \frac{dz}{dt} = \dot{x}_t \tag{4.4}$$

where $f_i$, $k_i$ and $\alpha_i$ are the friction force, spring stiffness and saturation limit of the $i$th GMS block; the internal frictional state $z$, is shared by all blocks. Staring from rest, the $i$th GMS block remains sticking until $f_i = \alpha_i F_C$, when it begins to slip. The block keeps slipping until the velocity crosses zero (i.e., motion reversal occurs). Note that the slip (i.e., gross motion) behavior of the blocks is normally represented using more complicated frictional dynamics [51][76]. However, Coulomb model is used in this dissertation to represent gross motion friction, since the focus is on mitigating the undesirable effects of pre-motion friction.

In general, the accuracy of the GMS model improves as $N$ increases. The GMS model parameters of the stage without FI are identified with $N$ = 10 blocks, using a frequency domain approach presented by Yoon and Trumper [55]. Ten plant FRFs from Figure 4.4 are selected, which are obtained via sine sweep using ten different input force amplitudes, ranging from 0.11 N to 4.95 N. The spring stiffness and saturation limit of each GMS block are obtained from a virgin

curve constructed based on the frequency and amplitude of the friction-induced resonance in each FRF. The identified parameters of the GMS model for the stage without FI are summarized in Table 4.4. Similar to the case of Dahl model, the GMS model parameters of the stage with FI are obtained from the re-constructed virgin curve, by combining frictional stiffness and FI stiffness in series; they are summarized in Table 4.5.

Table 4.4 Identified GMS friction model parameters for the stage without FI (No FI case).

| $i$ | $k_i$ [N/m] | $\alpha_i$ | $i$ | $k_i$ [N/m] | $\alpha_i$ |
|---|---|---|---|---|---|
| 1 | $1.34 \times 10^6$ | 0.0136 | 6 | $2.42 \times 10^4$ | 0.0508 |
| 2 | $4.93 \times 10^5$ | 0.0568 | 7 | $3.85 \times 10^4$ | 0.1139 |
| 3 | $8.61 \times 10^4$ | 0.037 | 8 | $1.75 \times 10^4$ | 0.0732 |
| 4 | $5.55 \times 10^4$ | 0.047 | 9 | $2.69 \times 10^4$ | 0.1540 |
| 5 | $5.87 \times 10^4$ | 0.0805 | 10 | $4.58 \times 10^4$ | 0.3733 |

Table 4.5 Identified GMS friction model parameters for the stage with FI (FI case).

| $i$ | $k_i$ [N/m] | $\alpha_i$ | $i$ | $k_i$ [N/m] | $\alpha_i$ |
|---|---|---|---|---|---|
| 1 | $4.44 \times 10^3$ | 0.0012 | 6 | $3.38 \times 10^3$ | 0.0295 |
| 2 | $8.49 \times 10^3$ | 0.0123 | 7 | $7.29 \times 10^3$ | 0.0797 |
| 3 | $3.93 \times 10^3$ | 0.0121 | 8 | $4.49 \times 10^3$ | 0.0606 |
| 4 | $3.75 \times 10^3$ | 0.0181 | 9 | $9.30 \times 10^3$ | 0.1520 |
| 5 | $5.88 \times 10^3$ | 0.0393 | 10 | $2.96 \times 10^4$ | 0.5951 |

Note that, although the GMS model provides a more accurate representation of pre-motion friction compared to the Dahl model, a relatively large number of blocks (and experimental trials) are needed to identify its parameters. Moreover, frequent tuning and re-calibration may be required to maintain the accuracy of all its parameters as pre-motion friction changes with time and/or stage's position.

Circular motions with 5 mm and 5 $\mu$m radius and different tangential velocities are used as the reference commands to the NP stage of Figure 4.2. The following cases are tested:

- Baseline: No FI case without FF compensation;

- No FI + Dahl: No FI case with FF compensation using the Dahl model ($k_\sigma = k_{\sigma,NoFI}$ are used);
- No FI + GMS: No FI case with FF compensation using the GMS model with $N = 10$ (see Table 4.4 for the identified parameters);
- FI + Dahl: FI case with FF compensation using the Dahl model ($k_\sigma = k_{\sigma,FI}$ are used);
- FI + GMS: FI case with FF compensation using the GMS model with $N = 10$ (see Table 4.5 for the identified parameters).

Figure 4.16 and Figure 4.17 summarize the percentage reductions in peak and RMS tracking errors achieved by different test cases (relative to the Baseline case) for the circle tests with various radii and velocities. During 5 mm circular motions, No FI + Dahl case reduces the peak and RMS tracking errors of the Baseline case. When the GMS model is used in the FF compensator, the tracking accuracy of the stage without FI is further improved. This is due to the improved accuracy afforded by the GMS model, compared to the Dahl model. However, using the simple Dahl model, the stage with FI (i.e., FI + Dahl case) achieves very similar or even better performance as the No FI + GMS case. When GMS model is used in the FI case, the resulting percentage improvements of peak and RMS tracking errors are very similar to that of the FI + Dahl case.

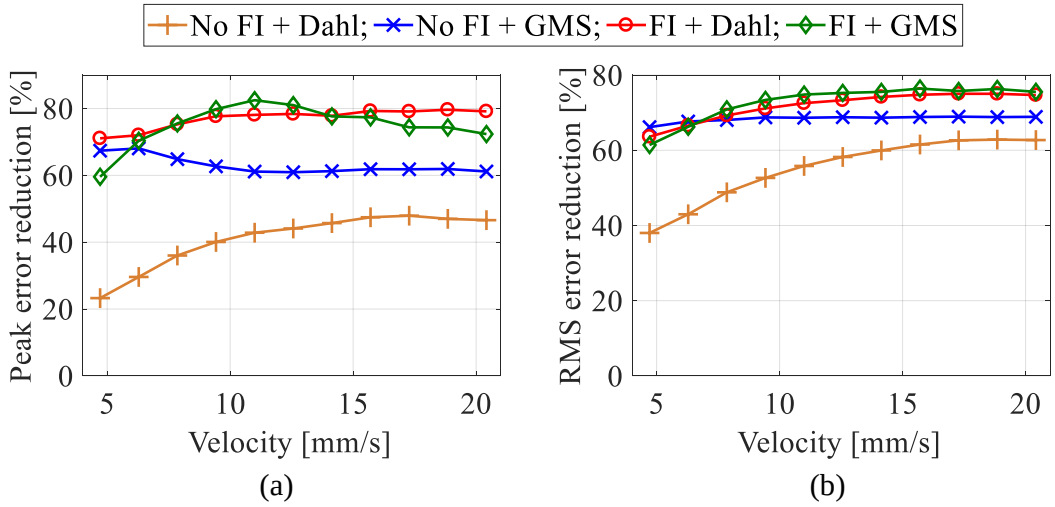


Figure 4.16 (a) Peak, and (b) RMS tracking error reductions achieved by different test cases, compared to the Baseline case, during 5 mm circle tests with different velocities.

During 5 $\mu$m circular motions, it is observed that the No FI + Dahl case performs even worse than the Baseline case. This relatively poor performance is mainly due to the large frictional stiffness estimation errors near motion reversals, even though the friction parameters are carefully identified. On the other hand, the No FI + GMS case exhibits consistently better tracking accuracy than the Baseline case due to its more-accurate estimation of pre-motion frictional stiffness. This indicates that complex models are required for accurate FF compensation of pre-motion friction on the stage without FI. However, the FI + Dahl case achieves significantly better performance, compared to the No FI + GMS case. This is because, when the motion range reduces, the pre-motion frictional stiffness during the circle tests becomes larger and the low stiffness FI becomes more dominant. This leads to more accurate compensation using the combined stiffness $k_c$, since it behaves almost as a linear low stiffness spring for the entire circular motions. Similar to the previous case, using the GMS model in the FF compensator provides marginal improvements on the stage with FI, over the Dahl model.

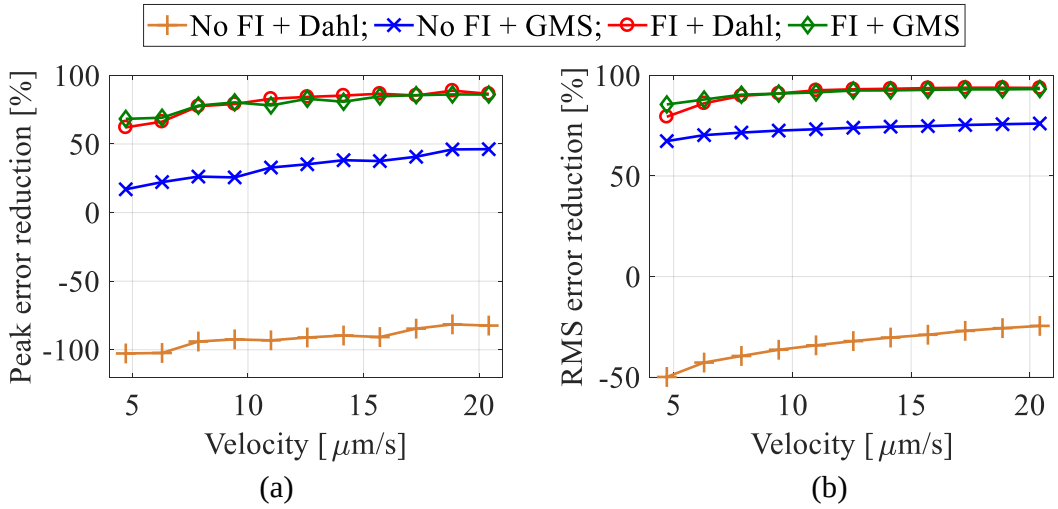


Figure 4.17 (a) Peak, and (b) RMS tracking error reductions achieved by different test cases, compared to the Baseline case, during 5 $\mu$m circle tests with different velocities.

The robustness of FF friction compensation in the presence of model parameter errors (due to inaccurate modeling or variations of friction) is also tested. Deviations of 0, ±10%, ±20% and ±50% are introduced into the identified frictional stiffness of the stage without FI (i.e., $k_{\sigma,NoFI}$ in Table 4.3 and $k_i$ in Table 4.4). For each deviation case, $k_{\sigma,FI}$ is re-calculated using $k_{fi}$ in Table 4.3

and the inaccurate $k_{\sigma,NoFI}$. Note that the FI + GMS case is not tested since it does not provide significant improvements over the FI + Dahl case, in terms of both peak and RMS tracking errors. Thanks to the much softer combined stiffness brought about by the introduction of FI, the Dahl model is able to accurately capture the equivalent pre-motion friction dynamics. Therefore, it makes practical sense to use the simpler Dahl model, whose two parameters can be easily identified, for the stage with FI. Further analysis is carried out in Section 6.4.2 to investigate under what circumstances that FI can enable accurate FF compensation using the simple Dahl model.

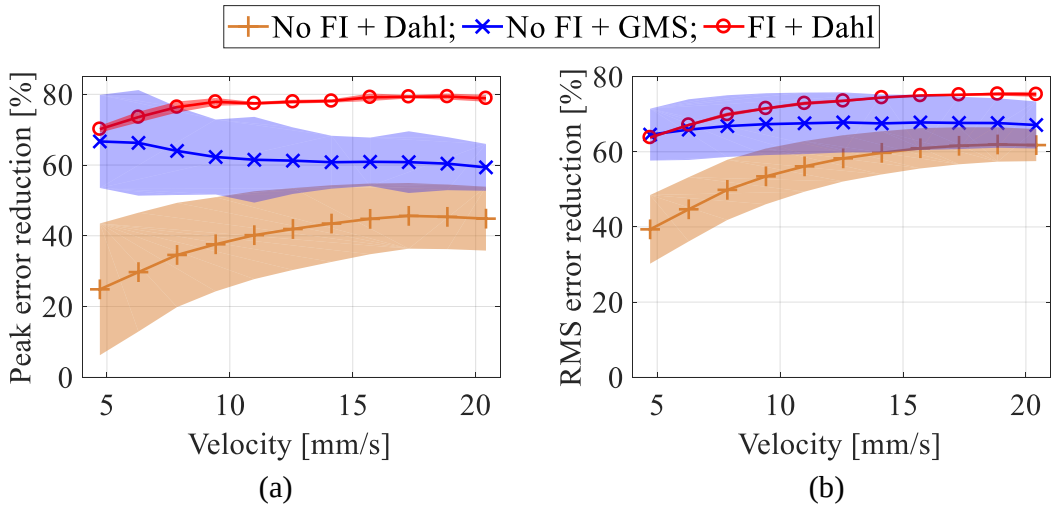


Figure 4.18 (a) Peak, and (b) RMS tracking error reductions achieved by different test cases, compared to the Baseline case, during 5 mm circle tests with different velocities. Estimation errors are introduced into the identified frictional stiffness. Solid lines represent mean values and shaded bands indicate $\pm 1\sigma$ (standard deviation).

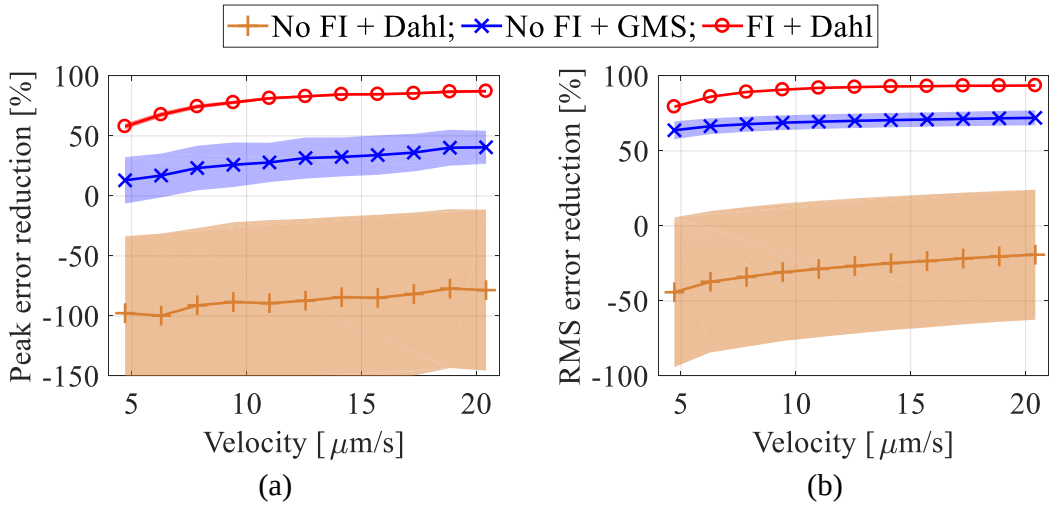


Figure 4.19 (a) Peak and (b) RMS tracking error reductions achieved by different test cases, compared to the Baseline case, during 5 $\mu$m circle tests with different velocities. Estimation errors are introduced into the identified frictional stiffness. Solid lines represent mean values and shaded bands indicate $\pm 1\sigma$ (standard deviation).

The performance variations are compared in Figure 4.18 and Figure 4.19 by plotting the mean percentage reductions of peak and RMS tracking errors (relative to the Baseline case), together with the corresponding $\pm 1\sigma$ (standard deviation) bands based on all deviation cases (seven instances for each circular command). As seen from the figure, the No FI + Dahl case and No FI + GMS case both suffer from large performance variations due to the errors in their pre-motion frictional parameters. This indicates that frequent re-calibration is needed to ensure robust FF compensation for the stage without FI. On the other hand, the FI + Dahl case provides very robust tracking accuracy due to the reduced sensitivity of combined stiffness $k_c$ to errors in pre-motion frictional stiffness $k_f$ (see Eq. (4.2)). With the proposed FI, accurate and robust FF compensation of pre-motion friction is achieved with a simple Dahl model, in the presence of up to 50% errors in the identified frictional stiffness.

## 4.5 Chapter summary

In this chapter, friction isolator (FI) is proposed as a simple, low cost, effective and robust mechatronics method to mitigate the undesirable effects of pre-motion friction. The idea of FI is to connect the mechanical bearing to the moving table of a nanopositioning (NP) stage using a

joint that is very compliant in the motion direction, thus effectively isolating the stage from the nonlinearities associated with bearing friction. Based on the proposed concept, a FI prototype is designed for an in-house built mechanical-bearing-guided NP stage. Very low stiffness in the motion direction of the stage is achieved, without overly compromising off-axis stiffness, by combining a positive-stiffness flexure with a negative-stiffness mechanism utilizing permanent magnets.

It is shown through frequency domain analysis using a PID controller that, for the same feedback gains, the in-house built NP stage with the FI prototypes demonstrates much less variations (nonlinearities) in the closed loop dynamics and higher bandwidth compared to the conventional stage without FI. This is because with the FI, the very stiff and variable frictional stiffness is replaced by a much softer and less variable stiffness, making it much easier for a feedback controller to deliver high performance and robustness through feedback linearization, without the need for very high gains. As a result, the stage with FI achieves 63% and 84% reductions in mean settling times during 5 mm and 5 $\mu$m point-to-point positioning tests, respectively. Circular tracking tests with different radii and tangential velocities demonstrate that the proposed FI significantly reduces peak and RMS tracking errors (up to 73%), compared to the case without FI, especially during short stroke motions. The introduction of FI also makes the stage highly insensitive to modeling errors and variations in pre-motion frictional stiffness. This enables accurate model-based feedforward (FF) compensation of pre-motion friction, using a simple model, leading to greatly improved tracking accuracy. Moreover, the FF compensator on the stage with FI also achieves superior robustness such that re-calibration is not needed even with up to 50% variations in the identified pre-motion frictional stiffness.

# Chapter 5

## Semi-active Isolator

The friction isolator (FI) proposed in Chapter 4 effectively isolates the stage from the harmful effects of pre-motion friction, making it a lot easier for a feedback controller to deliver high performance without the need for very high gains. The stage with FI achieves large and robust reductions of settling time during point-to-point positioning tests. However, it is observed that the benefits of bearing friction are also diminished due to the introduction of FI, resulting in increased motion error during in-position as seen from Table 4.2. This is because the motor drive displays certain noise even though the commanded current is zero – see Figure 5.1. When perturbed by the servo motor noise, the in-house built nanopositioning (NP) stage with FI has significantly larger errors while at rest (i.e., in-position), compared to the stage without it, as shown in Figure 5.2.

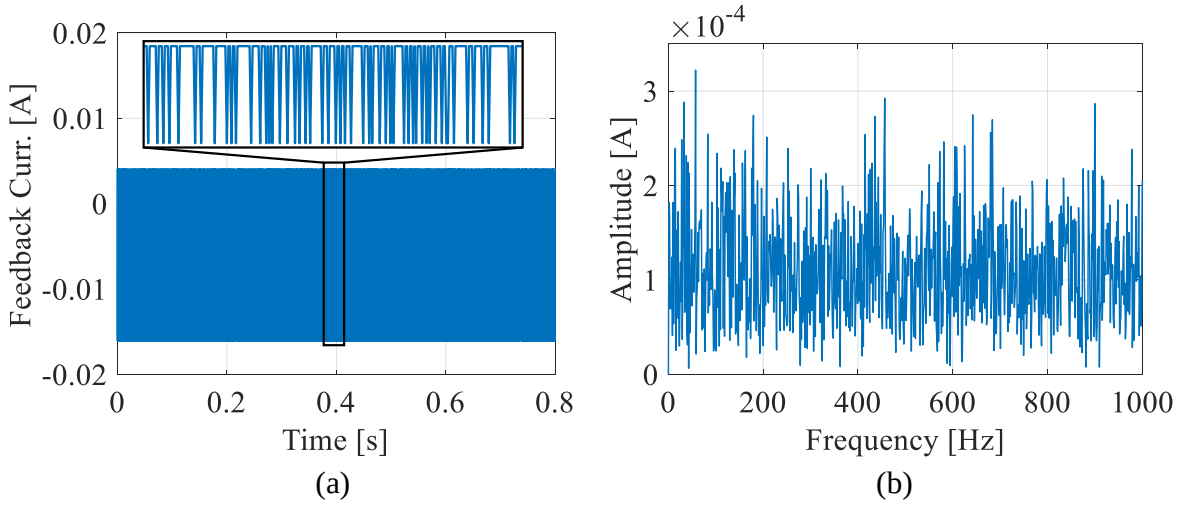


Figure 5.1 (a) Measured current noise from servo motor drive, and (b) frequency spectrum of current signal.

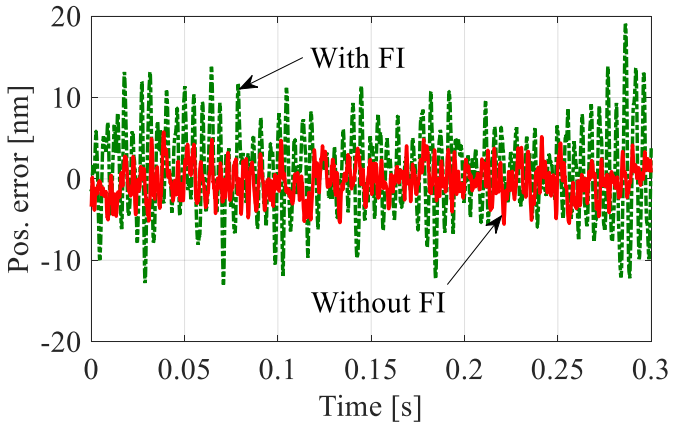


Figure 5.2 Measured in-position error using the in-house built NP stage of Figure 4.2 with and without FI.

Therefore, a semi-active isolator (SAI), which connects the mechanical bearings to a NP stage, is proposed for simultaneously achieving fast settling and excellent in-position stability. Section 5.1 presents the principle behind the proposed SAI. The design of a NP stage that equipped with a SAI prototype for experimental validation is discussed in Section 5.2. In Section 5.3, the adverse effect, due to switching of the designed SAI, on positioning performance of the stage is illustrated and a two-step control scheme is proposed for addressing it. Finally, the performance of SAI is evaluated using point-to-point positioning tests and circular tracking tests in Section 5.4.

This chapter is partially based on the following publication:

- Dong X, Okwudire CE. *Semi-active joint for ultra-precision positioning using sliding/rolling bearings*. CIRP Annals-Manufacturing Technology. 2019; 68(1):385–388.

## 5.1 Concept of semi-active isolator

Figure 5.3 shows the concept of the semi-active isolator (SAI) for mitigating the undesirable effects of pre-motion friction during motion transients while maintaining excellent in-position stability. As discussed in Section 1.3 and Section 4.1 (see Figure 1.6 and Figure 4.1), pre-motion friction is modeled as an equivalent spring of stiffness $k_f$ connecting the bearing to the ground [48]-[50][55][56]. At the start of the motion, $k_f$ is very large; but as more servo force is applied to counteract friction, $k_f$ rapidly reduces and eventually becomes zero, allowing full sliding/rolling of the stage. [46][49][52]. Due to the initially very large $k_f$, mechanical bearings

often have excellent in-position stability in the presence of noise from servo motor drives, compared to, e.g., air bearings which have near-zero stiffness in the motion direction. However, the high stiffness of pre-motion friction also leads to sluggish settling behavior of the stage during point-to-point motions [54]. In the proposed SAI approach, rather than being rigidly attached to the moving table of the stage, the bearing is attached using a joint (of stiffness $k_{sai}$) that can be switched between two modes: stiff and compliant. Accordingly, the stage with the SAI can be modeled as a series combination of $k_f$ and $k_{sai}$ with combined stiffness

$$k_c = \frac{k_f \times k_{sai}}{k_f + k_{sai}} \tag{5.1}$$

When the stage is at rest (e.g., while it is in-position), the joint is very stiff ($k_{sai} >> k_f$) such that the combined stiffness approaches the initially high stiffness of pre-motion friction (i.e., $k_c \rightarrow k_f$). As a result, the stage with SAI is equivalent to a conventional mechanical-bearing-guided NP stage which has excellent in-position stability. The joint becomes compliant ($k_{sai} << k_f$) once the stage starts to move (i.e., during motion transients) such that the combined stiffness is dominated by the much softer $k_{sai}$ (i.e., $k_c \rightarrow k_{sai}$). In this case, the resulting system turns into a friction-isolated NP stage (as discussed in Chapter 4) which achieves large reductions of settling time during point-to-point motions.

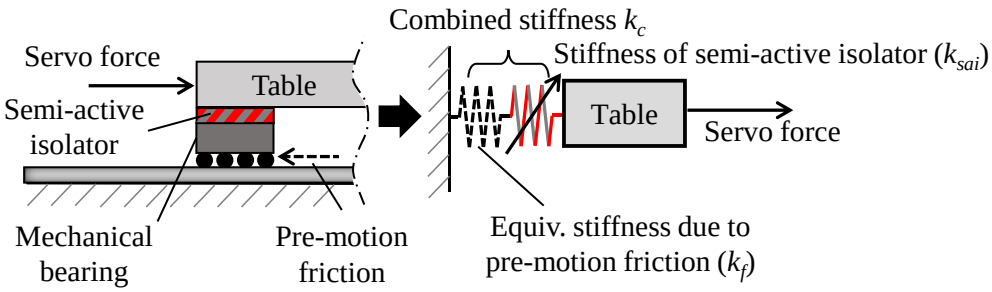


Figure 5.3 Schematic of a NP stage with mechanical bearing attached to the moving table using a semi-active isolator (SAI).

## 5.2 Design of a semi-active isolator prototype

As shown in Figure 5.4, a single-axis NP stage is designed and built for experimental validation of the proposed SAI. The stage has 1.4 kg moving mass and 25 mm travel range. It is guided by a high-rigidity mechanical bearing with end seals (THK, SR-25TB), riding on a precision grade rail that is lubricated using grease (THK, AFB-LF). A voice coil motor (Moticont, LVCM-044) is used to drive the stage and the table's position is measured using a linear encoder system (Renishaw, T1000 read head and RGSZ20 scale) with a post-interpolation resolution of 4.88 nm.

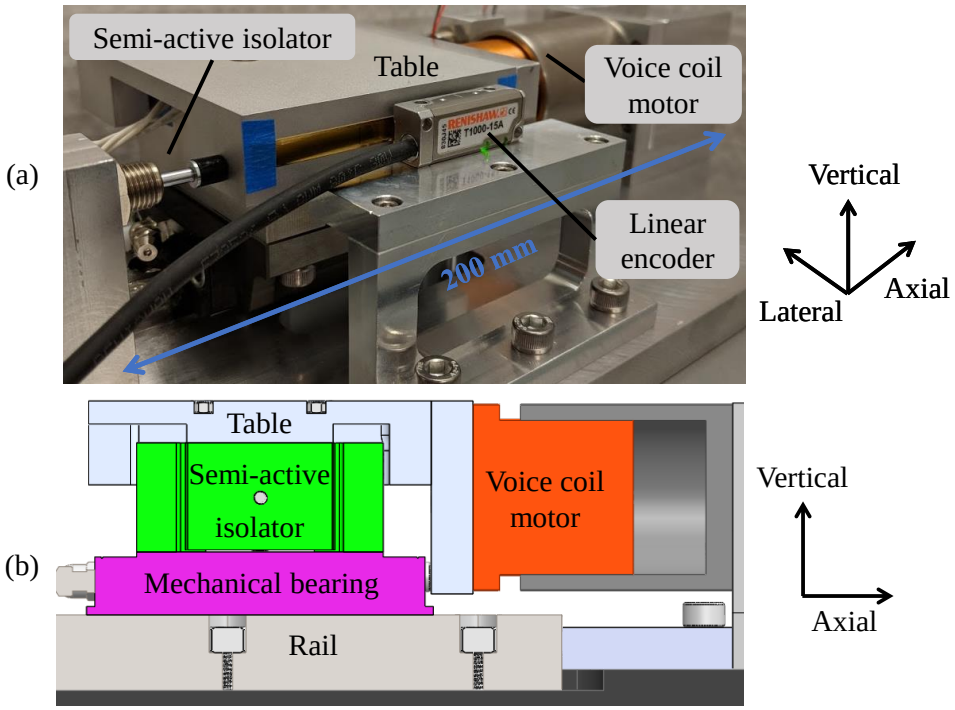


Figure 5.4 (a) Picture of an in-house built NP stage equipped with the designed SAI prototype, and (b) cross-section view of the stage's CAD model.

A semi-active isolator (SAI) prototype for attaching the mechanical bearing to the moving table of the NP stage, is designed as one possible realization of the proposed concept. As shown in Figure 5.5(a), to create compliance in the axial direction, a flexure with four leaf springs is adopted due to its non-contact and friction-free nature. The outer platform of the flexure is connected to the bearing and the center platform is connected to the table. Table 5.1 summarizes the stiffness values of the designed flexure (obtained via finite element analysis using

SolidWorks®), together with the stiffness values of mechanical bearing and their combination. Note that the flexure achieves orders of magnitude less stiffness (in the axial direction) than the initial contact stiffness of pre-motion friction experienced by the bearing. It also maintains the same order of magnitude of off-axis stiffness as the bearing, so as not to unduly compromise overall rigidity in lateral and vertical directions.

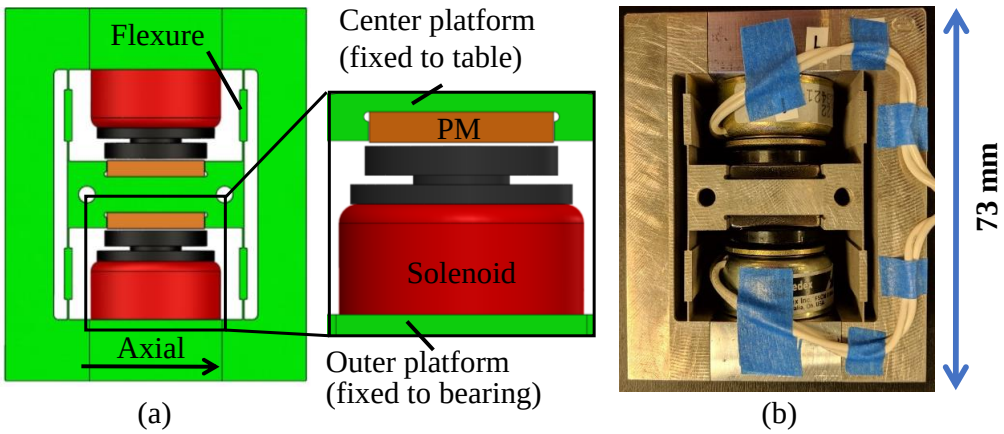


Figure 5.5 (a) CAD schematic, and (b) photo of the designed SAI prototype.

Table 5.1 Designed stiffness values of flexure, mechanical bearing and their combination [N/m].

| | Axial | Vertical | Lateral |
|---|---|---|---|
| Flexure | $5 \times 10^4$ | $5 \times 10^7$ | $1 \times 10^8$ |
| Mechanical bearing | $\sim 10^6$ | $3 \times 10^7$ | $4 \times 10^7$ |
| Combined (flexure + bearing) | $\sim 5 \times 10^4$ | $2 \times 10^7$ | $3 \times 10^7$ |

The stiffness of the designed SAI is switched using two solenoid actuators and permanent magnets (PMs) which are attached to the outer and center platforms of the flexure, respectively. When no power is applied, the PMs attract ferrous armatures of the solenoids such that the center platform of the flexure is locked to the outer platform through contact friction (i.e., the SAI is in stiff mode). When power is applied, the solenoid actuators pull the armatures away from the PMs to release the lock, allowing relative motion between the bearing and the moving table (i.e., the SAI is in compliant mode). Figure 5.5(b) shows the assembled SAI prototype; the flexure is manufactured from Aluminum 7075-T6 using wire EDM.

## 5.3 Mitigating switching-induced errors of semi-active isolator

Initial point-to-point positioning tests are carried out on the NP stage of Figure 5.4 to evaluate the performance of the proposed SAI. The stage is given 5 mm and 5 $\mu$m step motion commands and the time taken for it to settle into a ±25 nm window after each step (i.e., during the settling portion) is evaluated for the stage with the SAI prototype. Note that the SAI is switched to compliant mode before the start of the motion and switched back to stiff mode once the reference command reaches the target position (i.e., at the start of the settling portion).

A PID controller is used to control the stage. It is tuned to 200 Hz closed loop bandwidth based on the identified dynamics of the stage without SAI (i.e., equivalent to a conventional mechanical-bearing-guided NP stage). The exact same controller gains are used for controlling the stage with SAI. The controller is implemented on a real-time control board (dSPACE, DS1007), running at 10 kHz sampling frequency. A linear amplifier (Trust Automation, TA-115) is used to power the voice coil motor. The solenoid actuators are controlled through two relay modules to switch the SAI between its two modes.

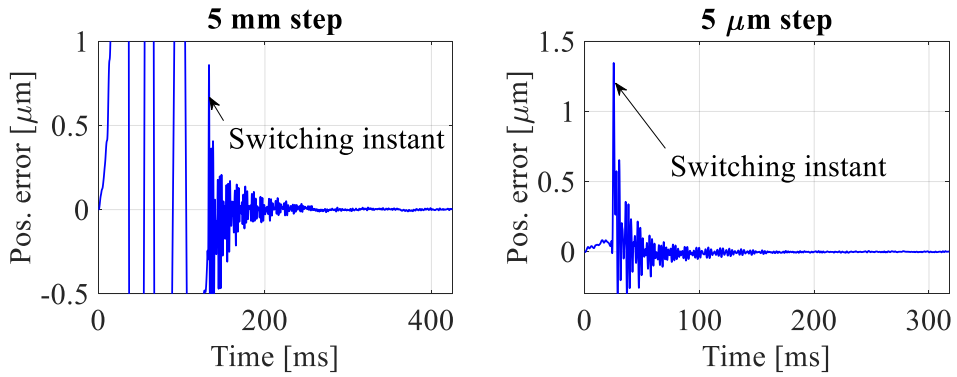


Figure 5.6 Typical position errors of the stage with SAI during (a) 5 mm, and (b) 5 $\mu$m point-to-point motions.

Figure 5.6 shows the typical positioning performance of the stage with SAI during 5 mm and 5 $\mu$m point-to-point motions. Observe that, in both cases, switching of the isolator (from compliant to stiff) during settling region introduces large motion errors, followed by severe

oscillations. As seen from the frequency spectrum of the position error signals after switching – see Figure 5.7, several high frequency modes are excited due to the impact force at the instant of switching. These high frequency oscillations take a very long time to settle, severely increasing the settling time of the stage with SAI.

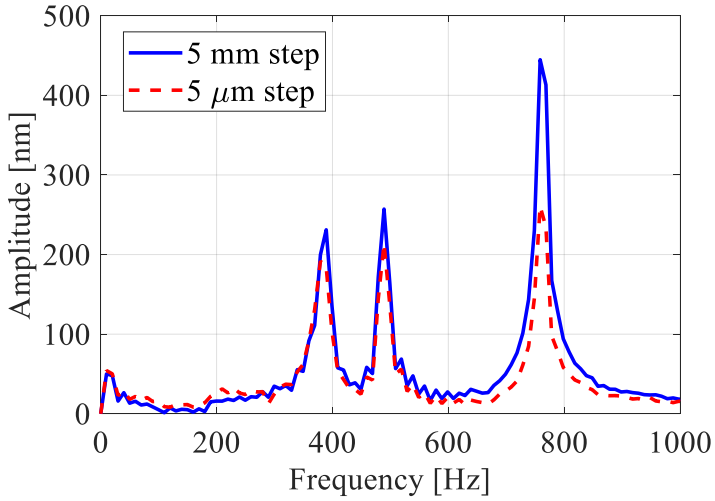


Figure 5.7 Sample frequency spectra of the position error signals of the stage with SAI after the switching instant.

A two-step scheme is proposed to mitigate the adverse effects of switching on the settling performance of the SAI approach:

- Step I (Cushioning): soften the impact force during switching via mechanical and electronic means;
- Step II (Compensation): modify the reference position of the stage to cancel out residual switching errors following Step I.

Polyurethane rubber sheets of 0.3 mm thickness are attached to the armatures of solenoids to provide additional mechanical cushioning when the SAI is switched from compliant to stiff mode (i.e., when the solenoid armatures contact the PMs). This also reduces the maximum gap between the PMs and solenoids from 0.4 mm to 0.1 mm such that the contact speed and the resulting impact force are decreased. Moreover, the voltage input to the solenoid actuators is low pass filtered using a resistor-capacitor (RC) circuit to further soften the impact force, electronically. The cutoff frequency of the first order RC filter is set to 300 Hz, which is just below

the lowest frequency peak in Figure 5.7. Note that reducing the cutoff frequency much below 300 Hz makes the switching unnecessarily sluggish without much benefit in attenuating the high frequency switching dynamics.

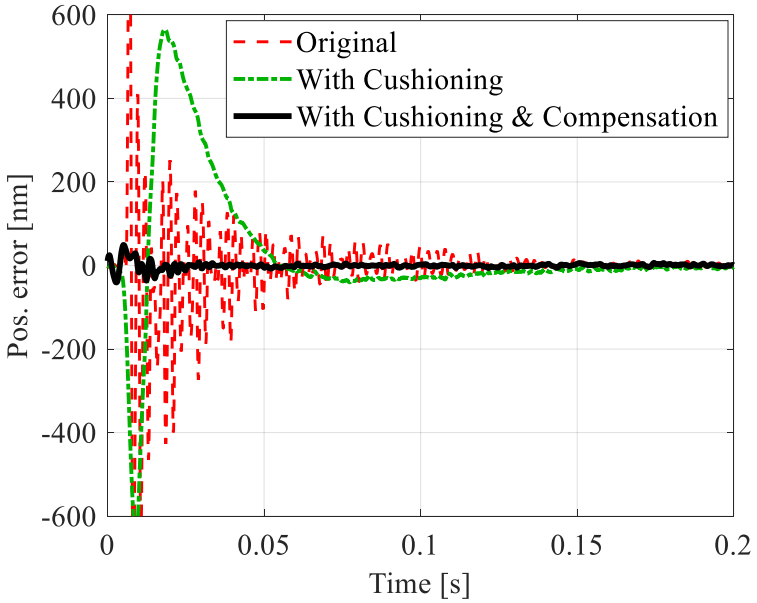


Figure 5.8 Position errors after switching of the SAI with and without the proposed error mitigation techniques.

Figure 5.8 shows the positioning errors when the SAI is switched from compliant to stiff mode. Thanks to the mechanical and electronic cushioning (i.e., Step I discussed above), the high frequency components of the positioning error are highly attenuated but are replaced with undesirable low frequency errors. Fortunately, these low frequency errors are very repeatable. Therefore, in Step II, they are compensated by adding a correction signal to the reference command of the stage each time a switch command is issued. Let $\mathbf{e}_k \in \Re^{q\times 1}$ represent the positioning error of the stage after the switching instant $k = \{0, 1, 2, \ldots\}$, while the stage is commanded to be at rest; $q$ is the number of discrete time steps in $\mathbf{e}_k$. The correction signal, $\mathbf{u}_{k+1} \in \Re^{q\times 1}$, is determined iteratively using a simple P-type iterative learning approach [140], given by

$$\mathbf{u}_{k+1} = LPF\left(\mathbf{e}_k\right) + \mathbf{u}_k \tag{5.2}$$

which is repeated starting from $\mathbf{u}_k = \mathbf{0}$ at $k = 0$ until $\mathbf{u}_{k+1} \approx \mathbf{u}_k$ (i.e., the correction signal reaches steady-state). Note that a 4$^{th}$ order low pass Butterworth filter (i.e., *LPF*) with a cutoff frequency of 200 Hz is applied to $\mathbf{e}_k$ to ensure stability of the iterative learning [140].

Figure 5.9 compares the position error (RMS) after the switching instant at each iteration $k$. Observe that the error reduces significantly after a few iterations and has converged by $k = 9$. Therefore, $\mathbf{u}_{10}$ is selected as the correction signal and is added to the reference position command of the stage whenever the SAI is switched from compliant to stiff mode. As seen from Figure 5.8, the adverse effects of switching on the positioning performance are effectively mitigated after implementing both steps of the proposed error mitigation scheme (i.e., Cushioning and Compensation).

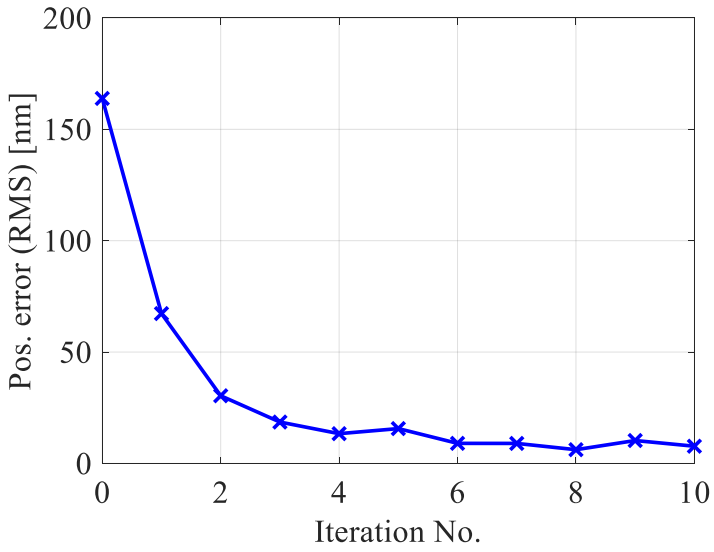


Figure 5.9 RMS value of the position error after each iteration of Eq. (5.2).

## 5.4 Experimental validation

### 5.4.1 Point-to-point positioning tests

Experiments are carried out on the stage of Figure 5.4. Point-to-point motion profiles with 5 mm and 5 $\mu$m step sizes are used as the reference trajectories and the time for the stage to settle into a ±25 nm window during the settling portion is evaluated for the following cases:

- Baseline: SAI is always in stiff mode; this is equivalent to a conventional mechanical-bearing-guided NP stage;

- FI: SAI is always in compliant mode; this is equivalent to a stage with (passive) FI (i.e., friction-isolated NP stage from Chapter 4);
- SAI: SAI is switched to compliant mode before the start of the motion and switched back to stiff mode once the reference command reaches the target position; the two-step switching error mitigating scheme from Section 5.3 is implemented whenever the SAI is switched from compliant to stiff mode.

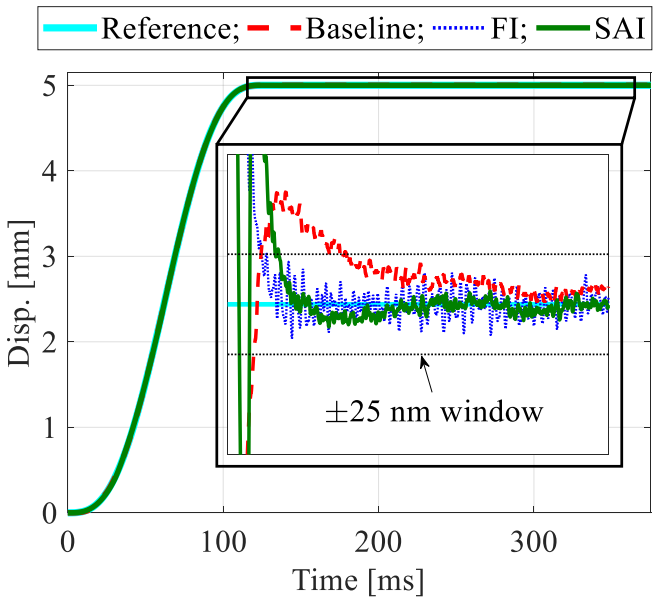


Figure 5.10 Typical settling performance of the stage into the ±25 nm window during 5 mm point-to-point motion. The black box shows the settling portion.

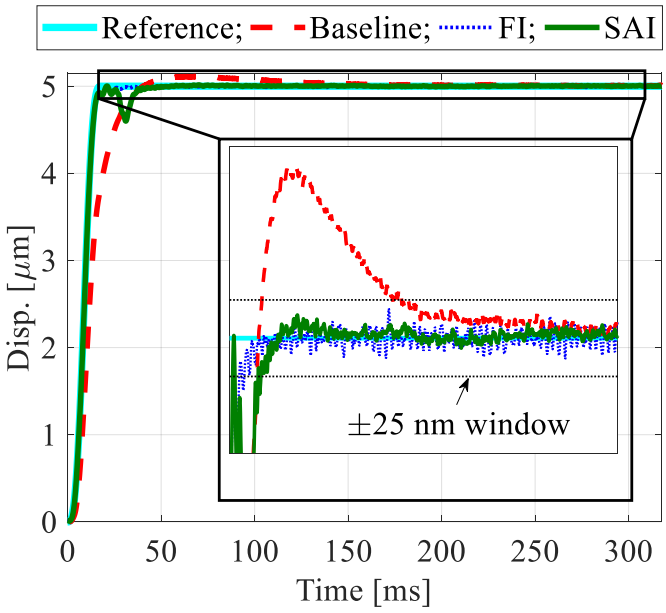


Figure 5.11 Typical settling performance of the stage into the ±25 nm window during 5 $\mu$m point-to-point motion. The black box shows the settling portion.

Figure 5.10 compares the settling performance of the Baseline, FI and SAI cases during the 5 mm step motion. The Baseline case takes 78 ms to settle within the ±25 nm window, with an RMS in-position error of 2.2 nm. The FI case reduces the settling time to 26 ms, but with a significantly increased RMS in-position error of 5.5 nm. Thanks to the proposed two-step error mitigation scheme, the SAI case settles within 34 ms (which is quite close to the FI case) with the same RMS in-position error (2.1 nm) as the Baseline case. Similarly, during the 5 $\mu$m step motion (see Figure 5.11), the SAI case achieves 82% and 58% reductions in the settling time and RMS in-position error, respectively, compared to the Baseline and FI cases.

The settling performance of the SAI case is slightly worse than the FI case even after implementing the two-step error mitigation scheme. This is because the correction signal (in Step II), that is determined while the stage is at rest, may be slightly different from the correction signal needed to fully eliminate switching-induced errors when the stage is commanded to move and settle. The reason is that the movement of the stage causes relative motion between the bearing and the table which may not have stopped at the time the switch is executed. Nonetheless, as noted above, the settling time reductions of the SAI case relative to the Baseline case are of similar levels as those achieved by the FI case.

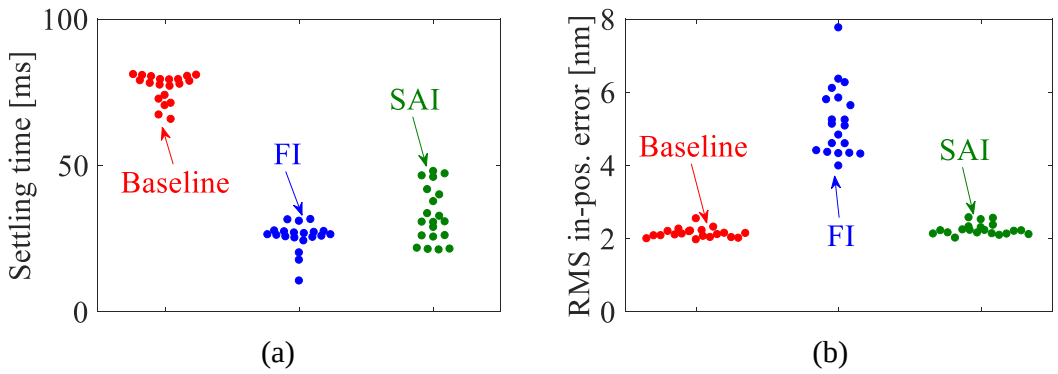


Figure 5.12 Comparison of (a) settling time into the ±25 nm window, and (b) RMS in-position error during 20 trials of 5 mm point-to-point motions.

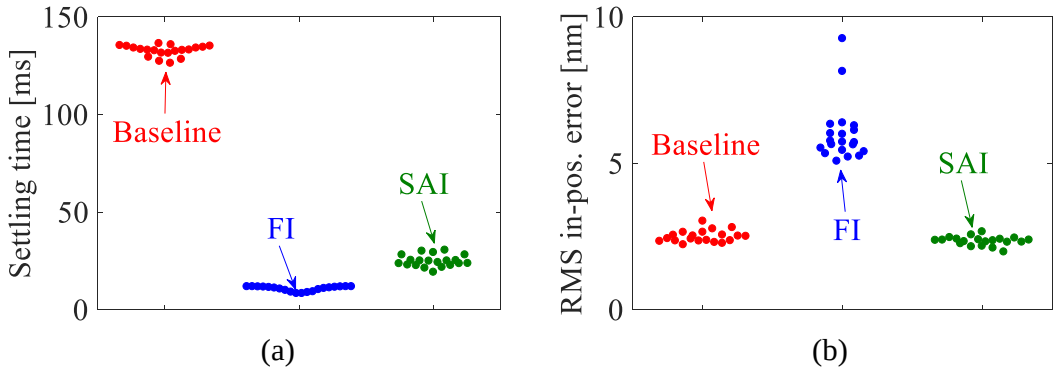


Figure 5.13 Comparison of (a) settling time into the ±25 nm window, and (b) RMS in-position error during 20 trials of 5 $\mu$m point-to-point motions.

Figure 5.12 and Figure 5.13 compare the settling time and in position stability during 5 mm and 5 $\mu$m point-to-point positioning tests, based on 20 trials at random positions of the table and Table 5.2 summarizes the mean settling time and RMS in-position error. The mean settling times of the Baseline case are 77 ms and 133 ms for the 5 mm and 5 $\mu$m steps, respectively. The FI case achieves 66% and 92% reductions in the mean settling times, at the cost of more than two times the in-position errors of the Baseline case. However, the SAI case achieves similar levels of mean settling time reductions (i.e., 61% and 81%) as the FI case without sacrificing the in-position stability, relative to the Baseline case.

Table 5.2 Comparison of mean settling time and in-position error (RMS) during 20 trials of 5 mm and 5 $\mu$m point-to-point motions.

| | | Baseline | FI | SAI |
|---|---|---|---|---|
| 5 mm step | Settling time [ms] | 133 | 11 | 25 |
| | RMS in-pos. error [nm] | 2.4 | 6 | 2.5 |
| 5 $\mu$m step | Settling time [ms] | 77 | 26 | 33 |
| | RMS in-pos. error [nm] | 2.2 | 5.2 | 2.2 |

### 5.4.2 Circular tracking tests

During point-to-point positioning tests, the stage with SAI achieves significantly improved settling time without sacrificing in-position stability, when compared to the conventional mechanical-bearing-guided NP stage. It is also worth investigating if the proposed SAI can provide any benefits over the FI approach during tracking motions. The idea is that the SAI can be switched to compliant mode during motion reversals to mitigate the undesirable effects of pre-motion friction, while remaining stiff during motion transients to maintain excellent disturbance rejection associated with bearing friction. Therefore, circular tracking tests with 5 mm and 5 $\mu$m radius and different tangential velocities are conducted. The $x$-axis reference trajectories of the circular motions are utilized to test the following cases:

- Baseline: SAI is always in stiff mode; this is equivalent to a conventional mechanical-bearing-guided NP stage;
- FI: SAI is always in compliant mode; this is equivalent to a stage with (passive) FI (i.e., friction-isolated NP stage from Chapter 4);
- SAI: SAI is only switched to compliant mode during motion reversals and remains in stiff mode for the rest of the circular motion. Note that only Step I (i.e., Cushioning) of the error mitigating scheme from Section 5.3 is implemented.

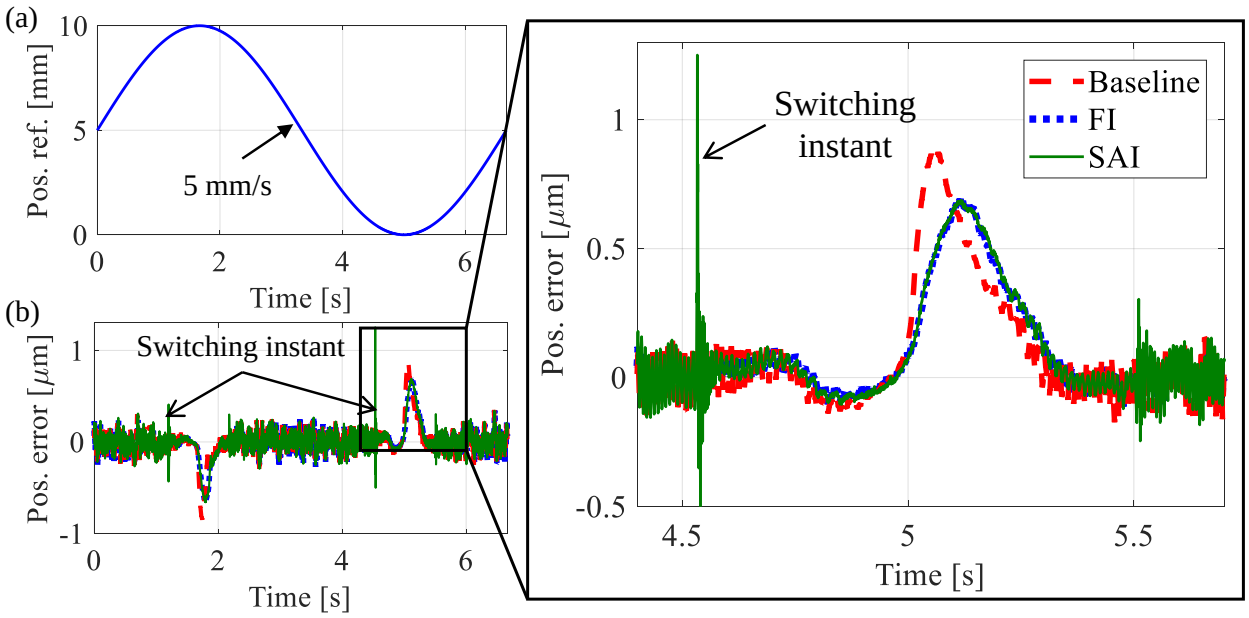


Figure 5.14 (a) *x*-axis position reference trajectory, and (b) tracking error of the stage during circle test with 5 mm radius and 5 mm/s velocity.

Figure 5.14 compares the typical tracking performance of the different cases, obtained from the 5 mm radius circle test with 5 mm/s tangential velocity. As also demonstrated in Section 4.4.2, the FI case reduces the amplitude of peak error, relative to the Baseline case. The proposed SAI case achieves the same reductions of peak error as the FI case during motion reversals, while maintaining similar tracking accuracy as the Baseline case during the rest of the circular motion (i.e., non-motion reversal region). However, large position errors are observed at the switching instant, severely hampers the tracking accuracy of the stage with SAI. Moreover, different from the point-to-point motions where the switching-induced errors remain largely unchanged for different experimental trials, the corresponding error amplitudes for two consecutive switching instants (when the SAI is switched from stiff to compliant mode) vary significantly as shown in Figure 5.14(b). This is because, the error is primarily caused by the impact force (when the solenoid armatures contact the PMs) as the SAI is switched from compliant to stiff mode during point-to-point motions; with the mechanical and electronic cushioning, the switching dynamics becomes relatively consistent. On the other hand, when the SAI is switched from compliant to stiff mode during tracking motions, the movement of the stage causes relatively large motion between the bearing and table, leading to deformation of the flexure. The friction lock between solenoids

and PMs prevents any further relative motion when the SAI is in stiff mode, such that elastic energy is stored inside the flexure. When the SAI is switched back from stiff to compliant mode before motion reversals, the stored elastic energy is released at the switching instant, acting as an "impact" force in the motion direction of the stage. This leads to large position errors since the feedback controller has difficulty to overcome the "instant" disturbance force. Moreover, because the relative motion between the table and bearing (or stored elastic energy) may be different, the corresponding "impact" disturbance for the following switching instant (i.e., when the SAI is switched back from stiff to compliant mode) may also be different, resulting in drastically different position errors. Therefore, it is not possible to accurately compensate this switching-induced error using a single correction signal, as in Step II of the proposed error-mitigation scheme (see Section 5.3).

The switching of SAI causes bigger problem during circular motions with 5 $\mu$m radius as shown in Figure 5.15. Observe that the switching-induced error (when SAI is switched from stiff to compliant mode) has much larger amplitudes, compared to the original tracking errors of the Baseline and FI cases. Moreover, for short stroke circle tests, the FI case achieves uniformly much better tracking accuracy for the entire motion. Therefore, it makes practical sense to use the SAI as a regular (passive) FI (i.e., SAI is always in compliant mode).

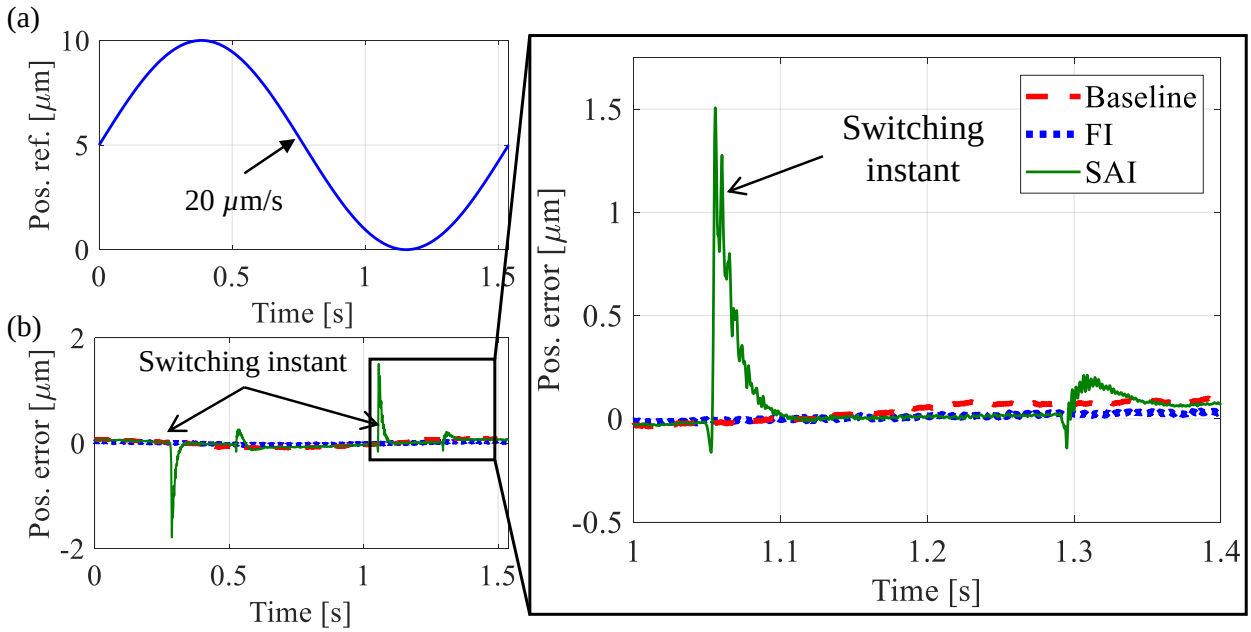


Figure 5.15 (a) *x*-axis position reference trajectory, and (b) tracking error of the stage during circle test with 5 $\mu$m radius and 20 $\mu$m/s velocity.

Figure 5.16 and Figure 5.17 summarize the peak and RMS tracking errors of different test cases during 5 mm and 5 $\mu$m circle tests with different velocities. The adverse effects due to switching become worse as the motion range (or speed) reduces. As a result, the SAI case has similar or worse performance as the FI case during 5 mm circle tests and suffers from significantly increased tracking errors during 5 $\mu$m circle tests, relative to both the Baseline and FI cases. Therefore, for many tracking applications of the NP stages which have little or no process-induced disturbance force, it is more practical to use the SAI as a regular FI.

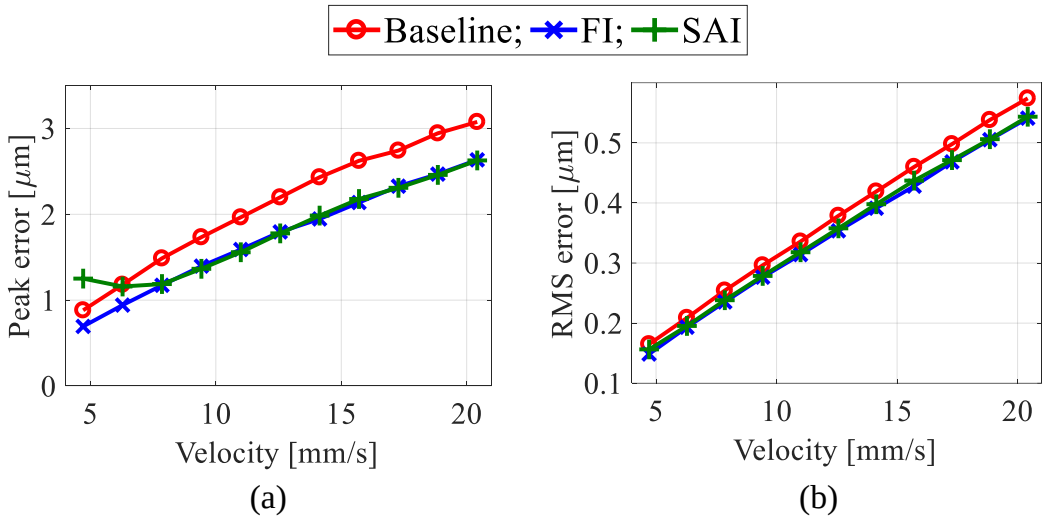


Figure 5.16 (a) Peak, and (b) RMS tracking error of different test cases during 5 mm circle tests with different velocities.

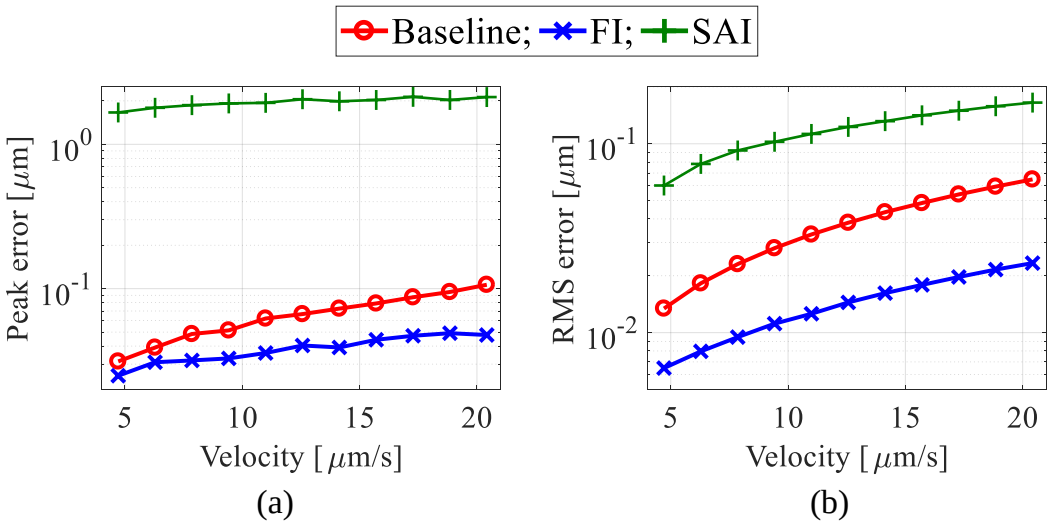


Figure 5.17 (a) Peak, and (b) RMS tracking error of different test cases during 5 $\mu$m circle tests with different velocities.

## 5.5 Chapter summary

This chapter presents a semi-active isolator (SAI) for simultaneously achieving rapid positioning with mechanical bearings while maintaining excellent in-position stability. The mechanical bearing is attached to the moving table of a nanopositioning (NP) stage using a joint that actively switches its stiffness between two modes: compliant and stiff. The joint is compliant

in the motion direction during motion transients such that the undesirable effects of pre-motion friction on the settling time are mitigated through the friction isolator (FI) approach; the joint becomes very stiff once the stage gets into position to leverage the benefits of bearing friction on in-position stability.

A SAI prototype is designed by integrating solenoid actuators and permanent magnets into a flexure hinge to realize the switching mechanism. Point-to-point positioning experiments are carried out on an in-house built NP stage equipped with the designed SAI prototype. It is observed that the impact force, caused by switching the SAI from stiff to compliant mode during the settling portion, introduces large motion errors and causes high frequency oscillations, severely jeopardizing the settling time of the stage. Therefore, a two-step scheme is proposed to address the adverse effects of switching on the positioning performance. Firstly, the impact force is softened by mechanical and electronic cushioning (using damping sheets and an RC filter). Then the remaining error is compensated in the second step by adding a correction signal to stage's reference position each time a switch command is issued. Using 5 mm and 5 $\mu$m point-to-point positioning tests, the stage with SAI (and the two-step switching error mitigation scheme) achieves similar levels of settling time reductions as the FI method without sacrificing in-position stability relative to a conventional mechanical-bearing-guided NP stage. Circular tracking tests reveal that switching the SAI from stiff to compliant mode also introduces large position errors, due to the stored elastic energy inside the flexure, severely hampering the tracking accuracy of the stage with SAI. Moreover, it is very hard to accurately compensate this switching-induced error without knowing the exact deformation of the flexure (i.e., stored elastic energy) at the switching instant. Therefore, for many NP applications which have little or no process-induced disturbance force, it makes practical sense to use the SAI as a regular FI (i.e., SAI is always in compliant mode).

# Chapter 6

## Influence of Design Parameters on the Effectiveness of Friction Isolator

The three mechatronics-based methods proposed in this dissertation are compared in Section 6.1. The friction isolator (FI) clearly stands out due to its simplicity, cost-effectiveness, excellent and robust performance in both point-to-point positioning and tracking motions. However, the introduction of FI hampers the disturbance rejection ability of the bearing friction. As a result, the stage with FI suffers from significant increases of in-position error. Moreover, the experimental results obtained from Section 4.4 are based an in-house built nanopositioning (NP) stage with a proof-of-concept FI design. The influence of design parameters (e.g., stiffness and damping coefficient) on the performance of FI (e.g., settling time, in-position stability and tracking accuracy), which is critical for applying the method, has not been explored.

Therefore, this chapter investigates the effects of design parameters on the effectiveness of FI. A brief overview of the experimental setup is discussed in Section 6.2 where three FIs with different stiffness and damping coefficients are tested on the NP stage of Figure 5.4. In Section 6.3, point-to-point positioning tests are conducted. It is observed that as the stiffness and damping of FI decrease, the in-position stability becomes worse while the settling time during short stroke motions reduces significantly. Frequency domain analysis that uses a simple model of the friction-isolated NP stage under the influence of pre-motion friction clearly demonstrates this design tradeoff. It is shown in Section 6.4 using circular tracking tests that the accuracy of model-based feedforward friction compensation improves with lower stiffness and higher damping FI design. Simulation analysis also confirms the experimental observation that the compensator remains robust when the stiffness of FI is an order of magnitude smaller than the initial large stiffness of pre-motion friction.

This chapter is partially based on the following publication:

- Dong X, Okwudire CE. *Influence of design parameters on the effectiveness of friction isolators in mitigating pre-motion friction in mechanical bearings*. Submitted to Mechatronics.

## 6.1 Comparison of proposed mechatronics methods

In Chapter 3 to Chapter 5, three mechatronics-based approaches are proposed to mitigate the undesirable effects of pre-motion friction in mechanical-bearing-guided nanopositioning (NP) stages; they are, vibration assisted nanopositioning (VAN), friction isolator (FI) and semi-active isolator (SAI). Since experiments are carried out using different testbeds, it is hard to compare the three methods in a rigorous (and quantitative) manner. Instead, Table 6.1 compares the different approaches using qualitative measurements based on the performance and practicality criteria described in Figure 1.8; a greater number of stars indicate better performance.

Table 6.1 Comparison of three mechatronics methods proposed in this dissertation[1,2].

| | | VAN | FI | SAI |
|---|---|---|---|---|
| **Performance** | Settling time | *** | ***** | **** |
| | In-position stability | *** | ** | ***** |
| | Tracking accuracy | *** | ***** | *[3] |
| **Practicality** | Cost effectiveness | * | ***** | *** |
| | Simplicity | * | ***** | *** |
| | Robustness | **** | ***** | **** |

Note:

1. Different approaches are qualitatively compared with respect to the performance and practicality criteria described in Figure 1.8; the greater number of stars, the better.
2. Note that the performance of each method is compared relative to the corresponding mechanical-bearing-guided NP stage.
3. The tracking accuracy of SAI can potentially be the same as FI if it is used as a regular FI (i.e., SAI is always in compliant mode); however, here evaluates the case when SAI is actively switched between two modes during tracking motions.

The VAN approach achieves 66% and 22% reductions of mean settling time during point-to-point positioning tests with 5 mm and 5 $\mu$m step sizes, respectively, compared to a conventional mechanical bearing stage. The stage with FI achieves better settling time, with 63% and 84% improvements relative to the stage without FI, for the 5 mm and 5 $\mu$m step motions. The SAI case suffers from slightly worse settling time reductions (61% and 81%), compared to the FI case, due to the imperfect compensation of the switching-induced errors. However, VAN and FI approaches cause up to 50% and 77% increase in the RMS in-position error. On the other hand, the stage with SAI achieves virtually the same in-position stability of a conventional mechanical-bearing-guided NP stage.

During circular motions, the VAN stage only achieves up to 15% reductions in the tracking errors, compared to the stage without dither. The stage with SAI performs even worse than the conventional mechanical bearing stage during circle tests with 5 $\mu$m radius due to the large errors caused by switching. Different from point-to-point motions where the switching-induced error is consistent and predictable after cushioning, the corresponding position error when the SAI is switched from stiff to compliant mode during tracking motions vary significantly with the deformation of flexure (or the stored elastic energy) at the switching instant, making it very hard to be compensated accurately and robustly. Finally, the stage with FI achieves superior performance with up to 75% reduction in position errors during circle tracking tests. Moreover, the introduction of FI enables accurate and robust model-based feedforward compensation of pre-motion friction using a simple model (with only two parameters), leading to significant improvements of tracking accuracy. Meanwhile, no re-calibration is needed in the presence of up to 50% uncertainty in the identified pre-motion frictional stiffness.

The FI is also the simplest, most cost-effective and robust solution among these three methods. The only design modification that is necessary to transfer a conventional mechanical-bearing-guided NP stage to a friction-isolated NP stage is to implement a flexure mechanism that connects each bearing to the moving table. In addition to this, the SAI adopts solenoid actuators and power electronics, to actively switch its stiffness between two modes. Moreover, a two-step error mitigation scheme, that utilizes mechanical/electronic cushioning and control regulation, is needed to ensure large reductions of settling time. This affects the robustness of the SAI method and leads to increases in cost and complexity. The VAN approach involves further mechanical/electrical modifications of a conventional mechanical-bearing-guided NP stage such

that high frequency vibration can be directly applied at the bearing location. Moreover, the piezo actuators and voltage amplifiers can be relatively costly, compared to the required components for FI and SAI.

In summary, the proposed FI approach rises to the top in almost all the categories except for the in-position stability. It also has the greatest potential to be broadly applied in different applications due to its low cost, simplicity, excellent and robust performance. As discussed in Appendix D, a rotary FI has been implemented on high precision roll-to-roll machine to mitigate the undesirable effects of friction during constant velocity tracking motions [141]. However, the experimental results obtained so far are based an in-house built NP stage with a proof-of-concept FI design. Therefore, to understand the influence of FI parameters on its performance, and to leverage its benefits on the settling time without overly sacrificing the in-position stability, the rest of this chapter focuses on investigating the effects of design parameters (e.g., stiffness and damping coefficient) on the effectiveness of FI.

## 6.2 Experimental setup

For the purposes of experimental validation, the in-house built NP stage of Figure 5.4 is utilized. Recall that the stiffness of the semi-active isolator (SAI), that is equipped on the stage, can be switched between two modes: stiff and compliant. In order to experimentally investigate the influence of design parameters on the effectiveness of friction isolator (FI), the designed SAI is operated in compliant mode throughout the entire motion; in this case, it is equivalent a regular (passive) FI. For the sake of brevity, it is referred to as FI in the rest of this chapter.

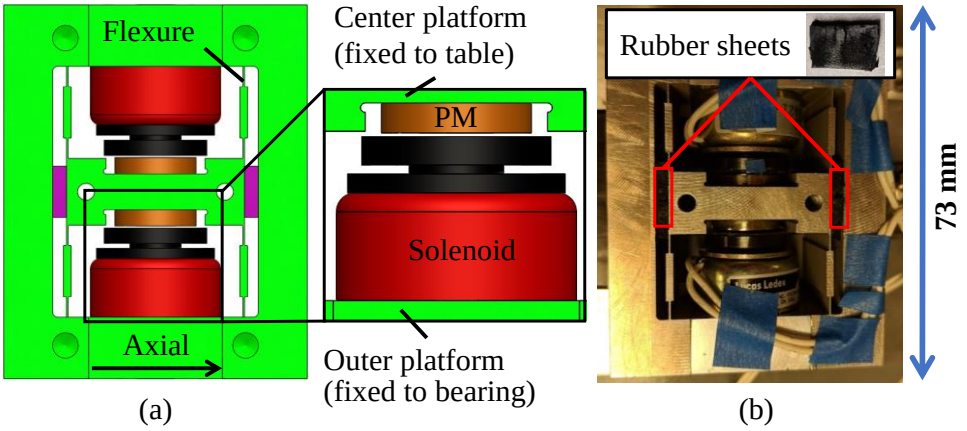


Figure 6.1 (a) CAD schematic, and (b) photo of the semi-active isolator (SAI) prototype designed in Section 5.2. Note that the SAI is referred to as FI in the rest of this chapter because it is used as a regular FI (by maintaining its stiffness in compliant mode).

Polyurethane rubber sheets with different sizes and hardness are placed in between the center and outer platforms of the flexure to alter the stiffness and damping properties of the designed FI. Table 6.1 summarizes the measured parameters of three FIs that are used in the following experiments. Although the HS-HD case has higher damping coefficient than the LS-HD case, their equivalent damping ratios are similar.

Table 6.2 Measured parameters of three FIs.

| Test case | Stiffness [N/m] | Damping coefficient [kg/s] |
|---|---|---|
| Low stiffness, low damping (LS-LD) | $3.3 \times 10^4$ | 240 |
| Low stiffness, high damping (LS-HD) | $2.9 \times 10^4$ | 520 |
| High stiffness, high damping (HS-HD) | $6.8 \times 10^4$ | 990 |

## 6.3 Influence of design parameters during point-to-point motions

### 6.3.1 Point-to-point positioning tests

Experiments are carried out on the NP stage of Figure 5.4 to evaluate the effectiveness of FI during point-to-point motions. The stage is given 5 mm and 5 $\mu$m step commands and the time for it to settle into a ±25 nm window after each step is evaluated for the following cases:

- No FI: the designed FI of Figure 6.1 is always in stiff mode;
- FI: the designed FI of Figure 6.1 is always in compliant mode.

The same PID controller from Chapter 5 is used to control the motion of the stage. Recall that it is tuned to 200 Hz closed loop bandwidth based on the identified dynamics of the No FI case; the exact same gains are used for controlling the FI case.

Table 6.3 Percentage reductions of settling time and RMS in-position error achieved by different FIs.

| | | LS-LD | LS-HD | HS-HD |
|---|---|---|---|---|
| 5 mm step | Mean settling time | 36% | 33% | 40% |
| | RMS in-pos. error | –118% | –81% | –66% |
| 5 $\mu$m step | Mean settling time | 89% | 65% | 49% |
| | RMS in-pos. error | –122% | –79% | –66% |

Table 6.3 summarizes the percentage improvements of settling times and RMS in-position errors of three FIs over the No FI case, during 5 mm and 5 $\mu$m point-to-point positioning tests. In general, the in-position stability improves as the stiffness and damping of the designed FI increase. During 5 $\mu$m step motions, it is observed that the settling time reduces significantly with a FI design of lower stiffness and damping. However, there is no obvious correlation between the settling time and changes in FI parameters during 5 mm step motions. The following frequency domain analysis is aimed at investigating the influence of design parameters on the settling time and in-position stability of the friction-isolated NP stage (i.e., stage with FI).

### 6.3.2 Frequency domain analysis

During settling, the stage mainly experiences pre-motion friction, therefore, the servo-controlled NP stage with FI is represented using the simple model shown in Figure 6.2. The motion stage is closed loop controlled through the actuation force $F_a$, using a PID controller. The FI attaching the table of mass $m_t$ to the bearing of mass $m_b$ is modeled by a spring with stiffness $k_{fi}$ and a damper with viscous coefficient $c_{fi}$. Pre-motion friction is also modeled as a spring-damper system of stiffness $k_f$ and damping coefficient $c_f$ that connects the bearing to the fixed ground. In addition, $x_r$, $x_t$ and $x_b$ are, respectively, the reference position, table displacement and bearing displacement. Note that the No FI case can be represented using the same model, assuming rigid connection between the moving table and bearing of the NP stage.

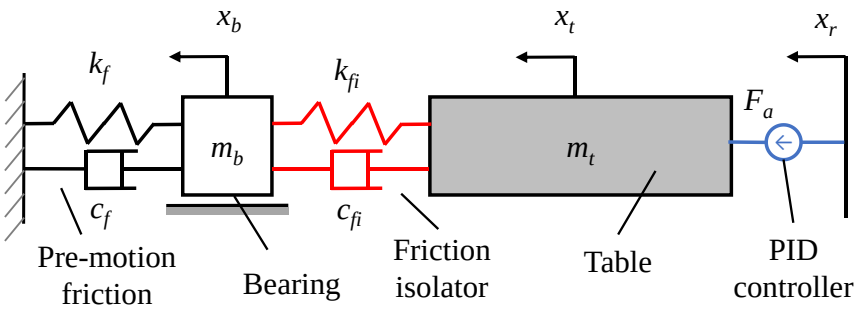


Figure 6.2 Simple model of a servo-controlled NP stage with FI under the influence of pre-motion friction.

To evaluate the settling performance of the friction-isolated stage, the closed loop error transfer function $G_e$ is utilized; it is given by

$$G_e(s) = 1 - \frac{x_t}{x_r} = \frac{1}{1 + C(s)G(s)} \tag{6.1}$$

where $C$ and $G$ represent the PID controller and open loop plant dynamics (from input $F_a$ to output $x_t$), respectively

$$
\begin{aligned}
&C(s) = K_p + \frac{K_i}{s} + K_d s;\; G(s) = \frac{b_2 s^2 + b_1 s + b_0}{a_4 s^4 + a_3 s^3 + a_2 s^2 + a_1 s + a_0};\\
&a_4 = m_t m_b;\; b_2 = m_b;\\
&a_3 = c_{fi}\left(m_t + m_b\right) + c_f m_t;\\
&a_2 = k_{fi}\left(m_t + m_b\right) + c_f c_{fi} + k_f m_t;\quad b_2 = m_b;\\
&a_1 = c_f k_{fi} + k_f c_{fi};\qquad\qquad b_1 = c_{fi} + c_f;\\
&a_0 = k_f k_{fi};\qquad\qquad\qquad\; b_0 = k_{fi} + k_f
\end{aligned}
\tag{6.2}
$$

Figure 6.3 compares the simulated closed loop error frequency response functions (FRFs) of the friction-isolated NP stage with the three FIs that are used in experiments. Observe that the FRFs of the FI cases have significantly less magnitudes at low frequency regions. This is because the combined stiffness is much smaller than that of the pre-motion frictional stiffness, making it easier for the same PID controller to deliver better disturbance rejection. Interestingly, increasing the damping of FI has adverse effects on the magnitude of $G_e$, below the resonance mode due to pre-motion friction (as highlighted in Figure 6.3(a)) [55]. Large damping, especially when the system is overdamped, acts as an additional disturbance that leads to sluggish settling behavior.

Figure 6.3(b) plots the 2-norm of the $G_e$ magnitude over the frequency range from 1 to 50 Hz, which is critical to the settling performance of the stage, as the stiffness and damping coefficient of FI vary. In general, lower stiffness and damping lead to smaller magnitude of closed loop error FRF and better settling performance, agreeing with the experimental results during 5 $\mu$m step motions. However, observe that reducing the stiffness and damping beyond certain thresholds (as highlighted in Figure 6.3(b)) provides little improvements. The frequency domain analysis fails to describe the settling performance during 5 mm point-to-point positioning tests. As the bearing friction experiences transitions between pre-motion and gross motion regimes in a short period of time, complex interactions between friction dynamics, controller dynamics and stage dynamics introduce large uncertainties [142]. Therefore, nonlinear analysis is needed to properly understand the transition of friction from pre-motion to gross motion regime (and vice versa) and its influence on the settling time of long range point-to-point motions.

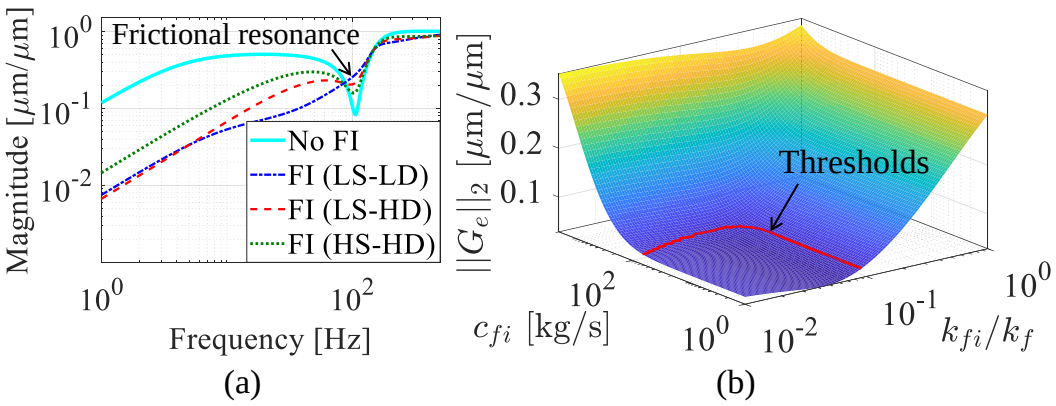


Figure 6.3 (a) Simulated closed loop error FRFs (i.e., $G_e$), and (b) 2-norm of $G_e$ magnitude with different stiffness and damping coefficient of FI.

The in-position stability is analyzed using the closed loop disturbance transfer function, $G_d$, from motor force to table displacement, since the error is mainly contributed by motor noise during in-position (see Figure 5.2); it is given by

$$G_d(s) = \frac{x_t}{F_a} = \frac{G(s)}{1 + C(s)G(s)} \tag{6.3}$$

Figure 6.4(a) compares the simulated closed loop disturbance FRFs using the friction-isolated NP stage with the three FIs. The FRF of the stage without FI has much smaller magnitudes than that of the FI cases, because the large frictional stiffness is able to resist the perturbation from the servo motor. Similarly, the FI with higher stiffness has better disturbance rejection ability, thus, smaller in-position error. Increasing damping coefficient attenuates the FRF near the resonance frequency of the FI, also leading to better in-position stability. Figure 6.4(b) summarizes the 2-norm of the $G_d$ magnitude (over the frequency range from 1 to 500 Hz, since motor noise is often broad band as shown in Figure 5.1) as a function of the stiffness and damping coefficient. The exact opposite trend as that of Figure 6.3(b) is observed; high stiffness and damping coefficient lead to smaller magnitude of closed loop disturbance FRF and smaller in-position error in the presence of motor noise. However, there is no obvious threshold for both design parameters; increasing stiffness and damping leads to continuous reduction of $G_d$ magnitude, thus, improving in-position stability.

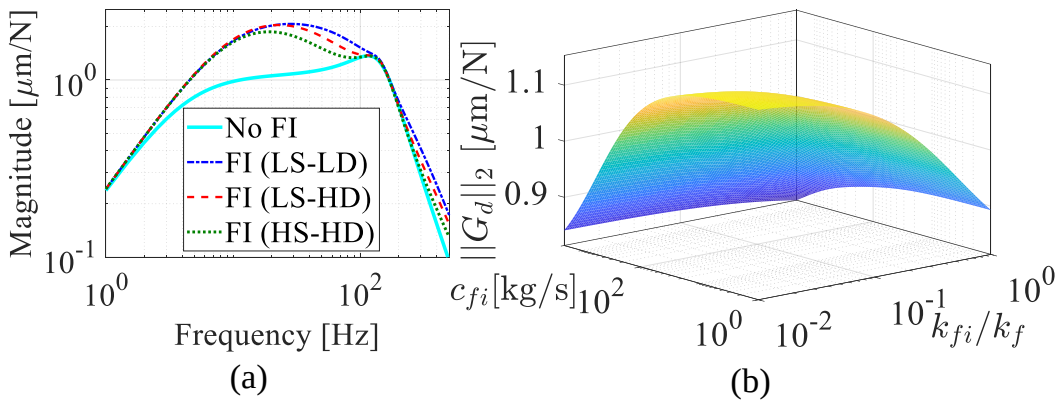


Figure 6.4 (a) Simulated closed loop disturbance FRFs (i.e., $G_d$), and (b) 2-norm of $G_d$ magnitude with different stiffness and damping coefficient of FI.

Given the clear tradeoff between settling time and in-position stability, careful considerations must be taken when using the FI for point-to-point positioning applications. It is recommended that the FI should be designed to meet the RMS in-position error requirements with the smallest stiffness and damping coefficient. In case the desired in-position stability requirement can be easily achieved with a wide range of parameters, the FI should be designed around the thresholds to avoid other potential side effects associated with small stiffness and/or damping (e.g., overly sacrificing rigidity in off-motion directions). If no acceptable parameters are found, the semi-active isolator (proposed in Chapter 5) that switches its mode from compliant, during settling, to stiff once the stage gets into position, should be used for simultaneously achieving fast settling and excellent in-position stability.

## 6.4 Influence of design parameters during tracking motions

### 6.4.1 Circular tracking tests with model-based feedforward friction compensation

As discussed in 4.4.3, the proposed FI enables accurate and robust feedforward (FF) compensation of pre-motion friction, leading to significantly reduced errors during tracking motions. Therefore, the effectiveness of FI is experimentally evaluated using circular tracking tests with 5 mm and 5 $\mu$m radius and different tangential velocities. The following cases are tested:

- Baseline: No FI case without FF compensation

- No FI + Dahl: No FI case with Dahl FF compensation;
- No FI + GMS: No FI case with GMS FF compensation;
- FI + Dahl: FI case with Dahl FF compensation;

Table 6.4 Identified Dahl friction model parameters (No FI case).

| $F_C$ [N] | $k_{\sigma,NoFI}$ [N/m] |
|---|---|
| 5.31 | $2.19 \times 10^6$ |

Table 6.5 Identified GMS friction model parameters (No FI case).

| $i$ | $k_i$ [N/m] | $\alpha_i$ | $i$ | $k_i$ [N/m] | $\alpha_i$ |
|---|---|---|---|---|---|
| 1 | $3.9 \times 10^5$ | 0.0104 | 6 | $4.9 \times 10^4$ | 0.0961 |
| 2 | $4.6 \times 10^4$ | 0.0605 | 7 | $1.4 \times 10^4$ | 0.0448 |
| 3 | $2.3 \times 10^4$ | 0.0916 | 8 | $2.2 \times 10^4$ | 0.1055 |
| 4 | $1.7 \times 10^4$ | 0.1333 | 9 | $3.1 \times 10^4$ | 0.2025 |
| 5 | $1.1 \times 10^4$ | 0.1453 | 10 | $1.4 \times 10^4$ | 0.1100 |

Note that only the Dahl model is used on the stage with FI since using the complex GMS model in the FF compensator does not lead to significant improvements over the simple Dahl model, as demonstrated in Section 4.4.3. Table 6.4 and Table 6.5 summarize the measured Dahl and GMS parameters of the stage without FI. They are obtained using the same approach as described in Section 4.4.3, applying to the in-house built NP stage of Figure 5.4. The equivalent parameters of the FI cases are calculated by combining the frictional stiffness and FI stiffness in series. Deviations of 0, ±10%, ±20% and ±50% are introduced into the identified frictional stiffness of the No FI case (as summarized in Table 6.4 and Table 6.5), to test the robustness of FF compensator in the presence of model parameter errors. For each deviation case, the equivalent stiffness values of the FI case are re-calculated using the inaccurate frictional stiffness.

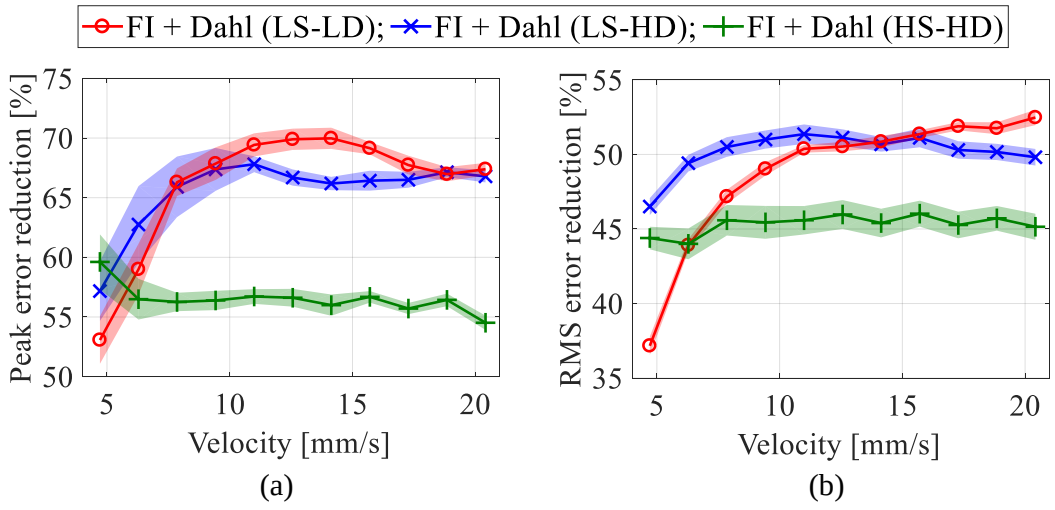


Figure 6.5 (a) Peak, and (b) RMS tracking error reductions achieved by different FIs, compared to the Baseline case, during 5 mm circle tests with different velocities. Estimation errors are introduced into the identified frictional stiffness. Solid lines represent mean values and shaded bands indicate $\pm 1\sigma$ (standard deviation).

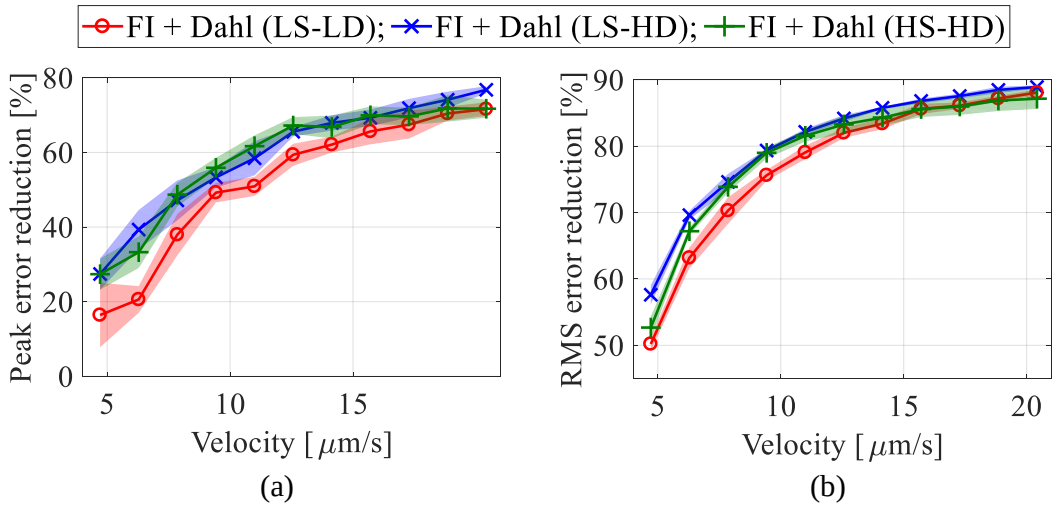


Figure 6.6 (a) Peak, and (b) RMS tracking error reductions achieved by different FIs, compared to the Baseline case, during 5 $\mu$m circle tests with different velocities. Estimation errors are introduced into the identified frictional stiffness. Solid lines represent mean values and shaded bands indicate $\pm 1\sigma$ (standard deviation).

Figure 6.5 and Figure 6.6 compare the percentage error reductions in peak and RMS tracking errors achieved by different FI designs (over the Baseline case). Regardless of the changes in stiffness and damping coefficient, the robustness of FF compensator for the three FIs are very similar; the remaining variations are primarily due to non-repeatable disturbances in the system, such as motor noise, variations of on-machine friction dynamics. Also observe that FF compensation using the three FIs achieves almost the same performance during circle tests of 5 $\mu$m radius. In this case, the FI behaves as a linear low stiffness spring, which dominates the equivalent stiffness felt by the servo controller; the accuracy of FF compensator remains un-affected if the identified FI stiffness is accurate enough. As the stiffness of FI increases, the effectiveness of FF compensator during circle tests of 5 mm radius becomes worse; however, the differences in peak and RMS error reductions are only about 10% and 5%, respectively. Interestingly, reducing the damping coefficient of FI negatively impacts the RMS error reductions, especially during circle tests with low velocities. This is because the tracking errors during non-motion reversal portions of the circle, which are mainly contributed by the variations of gross motion friction [141], have large impacts on the overall RMS errors. The resonance mode due to the FI can be easily excited when the damping is small, resulting in increased motion errors [141]. The benefits of higher damping on the RMS tracking errors vanish when the reference velocity is large, as the peak errors during motion reversals become dominant.

### 6.4.2 Simulation analysis

As discussed in Section 6.4.1, the accuracy and robustness of FF friction compensation are primarily affected by the stiffness of FI. In Section 4.4.3, it is demonstrated that the tracking accuracy of the FI + Dahl case is very similar to that of the FI + GMS case (see Figure 4.16 and Figure 4.17). Therefore, it makes practical sense to use the simpler Dahl model with the FI. In this section, the accuracy of FI + Dahl is evaluated against FI + GMS to understand under what circumstances the FI can enable accurate FF compensation using the simple Dahl model. It is assumed that, due to its high order and complexity, the GMS model can accurately capture the actual friction dynamics of the stage if its parameters are carefully identified.

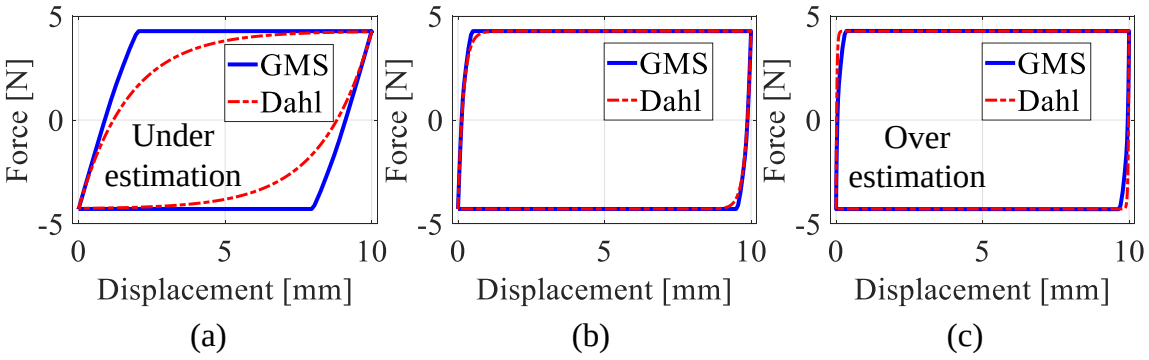


Figure 6.7 Simulated friction forces using Dahl and GMS models for the FI case with stiffness ratio ($k_{fi}/k_f$) of (a) 0.01, (b) 0.1, and (c) 1.

Figure 6.7 compares the simulated friction forces during 5 mm radius circle test using Dahl and GMS models for the FI case with different stiffness values; note that the tangential velocity is irrelevant since both friction models are rate-independent [52]. In general, smaller stiffness leads to more linear behavior of the combined stiffness and better compensation accuracy. However, the Dahl model tends to underestimate the friction force when the FI stiffness is extremely small, resulting in large force difference. Fortunately, the feedback controller can effectively suppress this slow change of disturbance force. Figure 6.8 plots the calculated RMS force difference, $\gamma$, between Dahl and GMS models for the FI case during one cycle of the 5 mm circle test. The accuracy of FF compensator using the Dahl model is optimal when the stiffness ratio ($k_{fi}/k_f$) is around 0.05 – 0.1. Increasing the stiffness of FI beyond this range often leads to over-compensation of the friction force, which is commonly observed in the stage without FI as error spikes toward the opposite direction of stage's motion.

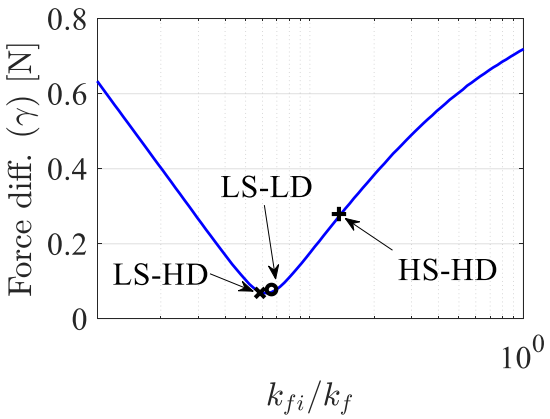


Figure 6.8 Calculated RMS force difference ($\gamma$) between Dahl and GMS models for the FI case during circle test of 5 mm radius.

The robustness of FF compensator is investigated through quasi-static stiffness analysis, using the stage's model shown in Figure 4.1. The sensitivity $\kappa$ of the combined stiffness $k_c$ to errors in $k_f$ (due to low fidelity modeling or variations of friction) are given by Eq. (4.2). As discussed in Section 4.4.3, if $k_{fi} << k_f$, and $k_{fi}$ is precisely known, $\eta \to \infty$ and $\kappa \to 0$. This indicates that if FF compensation is carried out using the FI case (i.e., $k_c$), variations of $k_f$ will not affect the result much. Figure 6.9 plots the sensitivity $\kappa$ as the stiffness ratio $\eta$ changes. So long as the stiffness of FI is one order of magnitude smaller than that of the equivalent stiffness of pre-motion friction (i.e., $\eta < 0.1$), the FF compensation remains relatively robust.

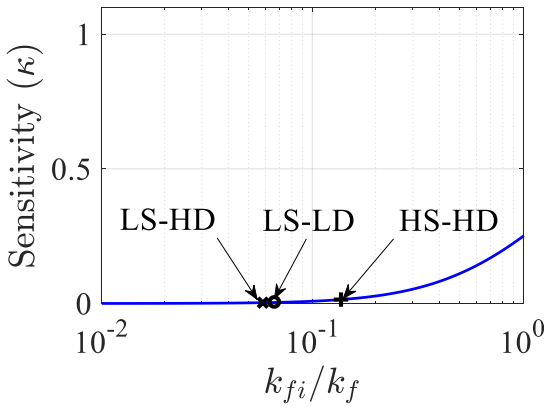


Figure 6.9 Calculated sensitivity ($\kappa$) of combined stiffness $k_c$ to variations of frictional stiffness $k_f$.

Since the accuracy and robustness of FF friction compensation both improve as the stiffness of FI reduces, using FI for tracking applications is more straightforward. It is recommended that the FI should be designed to have as small stiffness as possible. In practice, this is often limited by other design considerations, such as the off-axis stiffness requirements. The damping of FI should be designed to achieve at least a critically damped system to avoid excitation of the resonance mode by variations of friction force in the gross motion regime [141], or other un-modeled disturbances.

## 6.5 Chapter summary

Among three proposed mechatronics solutions for mitigating the undesirable effects of pre-motion friction, the friction isolator (FI) rises to the top of the list because of its excellent performance and practicality, with great potential of being broadly applied in different applications. Therefore, this chapter investigates the influence of design parameters on the effectiveness of FI, which is critical for applying the method. The in-house built nanopositioning (NP) stage equipped with a FI prototype from Chapter 5 is used for experimental validation; the stiffness and damping coefficient of the designed FI are varied by adding rubber sheets of different sizes and hardness.

During point-to-point positioning tests, a clear tradeoff between faster settling and better in-position stability is observed for short range motions: the stage with a lower stiffness and damping FI design achieves better settling performance at the cost of increased in-position error. Frequency domain analysis using a simple model of the friction-isolated NP stage under the influence of pre-motion friction confirms the experimental finding. When using FI for point-to-point positioning applications, it should be designed to meet the in-position stability requirement with the smallest stiffness and damping coefficient.

During circular tracking tests, accurate and robust feedforward (FF) compensation of pre-motion is achieved in the presence of up to 50% modeling errors (or variations) in the identified frictional stiffness. Sensitivity analysis with respect to variations of friction reveals that the FF compensator remains robust so long as the stiffness of FI is an order of magnitude smaller than the initially large value of pre-motion frictional stiffness. In addition, the accuracy of FF compensator improves when the stiffness of FI reduces, as is confirmed by both numerical simulations and experiments. When using FI for tracking applications, its stiffness should be designed as small as

possible with a large enough damping coefficient. Other design requirements should also be considered in practice, such as off-axis rigidity of the stage.

# Chapter 7

# Conclusions and Future Work

## 7.1 Conclusions

Mechanical bearings are finding increasing use in nanopositioning (NP) stages due to their long range, high rigidity and vacuum/cleanroom compatibility. However, the presence of pre-motion friction adversely affects the precision and speed of mechanical-bearing-guided NP stages. This doctoral dissertation has proposed three novel mechatronics methods for mitigating the undesirable effects of pre-motion friction in NP stages with mechanical bearings. Unlike most control-based methods available in the literature that rely on accurate models of pre-motion friction dynamics, the proposed methods focus on mechanical design modifications of the existing NP stages, accompanied by simple control strategies to ensure that the benefits of each method are realized with little or no side effects. Although the proposed methods are discussed in the context of NP stages, they are readily applicable to other precision motion stages with mechanical bearings, including linear and rotary types, which are widely employed in manufacturing and metrology-related processes.

In Chapter 3, vibration assisted nanopositioning (VAN) is proposed to mitigate the slow settling problem due to pre-motion friction using high frequency vibration (or dither). Different from the existing dithering techniques that jeopardize the motion precision by directly vibrating the stage or guideway, VAN proposes the use of two short stroke actuators (e.g., piezo actuators), acting opposite to each other, to apply dithering forces directly to the mechanical bearings such that the unbalanced reaction forces due to dithering are minimized at the moving table of the NP stage. Moreover, a control scheme with a harmonic cancelling controller is proposed to compensate any parasitic vibration, caused by non-idealities in the mechanical/electrical design and assembly of the stage. A prototype VAN stage is designed and built based on the proposed concept. Experiments conducted using the VAN stage demonstrates up to 66% reductions in the settling time during point-to-point positioning tests. The additional heat and potential wear caused

by dithering are also shown to be un-important in practice. Circular tracking tests with different radii and tangential velocities show that the proposed VAN approach achieves slightly reduced peak and RMS tracking errors (up to 15%), compared to a conventional mechanical-bearing-guided NP stage. Although the implementation of piezo actuators and voltage amplifiers introduces additional costs and complexities to the system, the resulting VAN stage is simpler and cheaper than the existing coarse-fine techniques that are used to improve the precision and speed of mechanical bearing stages.

To address the cost and complexity issues associated with the VAN approach, friction isolator (FI) is proposed to mitigate the undesirable effects of pre-motion friction, which is simpler and more cost-effective compared to VAN and coarse-fine arrangements. The idea of FI is to connect the mechanical bearing to the moving table of a NP stage using a joint that is very compliant in the motion direction, thus effectively isolating the stage from nonlinearities associated with bearing friction. Based on the proposed concept, a FI prototype is designed for a single-axis NP stage. Very low stiffness in the motion direction of the stage is achieved, without overly compromising off-axis stiffness, by combing a positive-stiffness flexure with a negative-stiffness mechanism utilizing repelling permanent magnets. It is shown through frequency domain analysis that with FI, the very stiff and variable frictional stiffness is replaced by a much softer and less variable stiffness, making it much easier for a feedback controller to deliver high performance and robustness without the use of high gains. As a result, the stage with FI achieves 63% and 84% reductions in mean settling times during 5 mm and 5 $\mu$m point-to-point positioning tests, respectively. The introduction of FI also makes the stage highly insensitive to modeling errors and variations in pre-motion frictional stiffness. This enables accurate model-based feedforward (FF) compensation of pre-motion friction, using a simple friction model, leading to greatly reduced peak and RMS tracking errors during circular tracking tests with different radii and tangential velocities. Moreover, the FF compensator on the friction-isolated NP stage achieves superior robustness such that re-calibration is not necessary in the presence of up to 50% variations in the identified pre-motion frictional stiffness.

One side effect of the FI approach is that it jeopardizes the benefits of bearing friction on the in-position stability, causing increased error when the stage is perturbed by noise from the servo motor drive during in-position. To alleviate this issue, semi-active isolator (SAI) is proposed for simultaneously achieving fast settling and excellent in-position stability. The SAI, that

connects the mechanical bearing to the moving table of the NP stage, is compliant in the motion direction during motion transients such that the undesirable effects of pre-motion friction on the settling time are mitigated through the FI approach. The SAI becomes very stiff once the stage gets into position to leverage the benefits of bearing friction on in-position stability. A SAI prototype is designed and built in which solenoid actuators and permanent magnets are combined with flexure mechanism to switch its stiffness between two modes (i.e., compliant and stiff). A two-step scheme is developed to address the adverse effects caused by switching of the SAI (from compliant to stiff mode) on the positioning performance. Using the 5 mm and 5 $\mu$m point-to-point positioning tests, the stage with SAI (and the two-step switching error mitigation scheme) achieves similar levels of settling time reductions as the FI method without sacrificing in-position stability relative to a conventional mechanical-bearing-guided NP stage. Circular tracking tests reveal that switching the SAI from stiff to compliant mode also introduces large position errors, as a result of the stored elastic energy inside the designed flexure, severely jeopardizing the tracking accuracy of the stage with SAI. Moreover, it is very hard to effectively and robustly compensate this switching-induced error without an accurate knowledge about the deformation (or stored elastic energy) of the flexure at the switching instant.

The three proposed mechatronics methods are compared with respect to their performance and practicality, and the FI approach rises on the top in almost every criterion with the only exception being in-position stability. Therefore, the influence of design parameters on the effectiveness of FI, which is critical for applying the method and leveraging its benefits on the settling time and tracking accuracy without overly compromising in-position stability, are investigated. Point-to-point positioning tests and circular tracking tests are conducted on the in-house built NP stage with a FI prototype whose stiffness and damping coefficient are varied by adding rubber sheets of different sizes and hardness. During point-to-point positioning, the stage with a lower stiffness and damping FI design achieves faster settling time at the cost of increased in-position error. Frequency domain analysis using a simple model of the friction-isolated NP stage under the influence of pre-motion friction confirms this design tradeoff. Therefore, when using FI for point-to-point positioning applications, it should be designed to meet the in-position stability requirement with the smallest stiffness and damping coefficient. During circular tracking motions, it is observed that the accuracy and robustness of FF friction compensation improve when the stiffness of FI reduces. However, it must be noted that the FF compensation remains accurate and

robust so long as the stiffness of FI is an order of magnitude smaller than the initially large value of pre-motion frictional stiffness. Thus, when using FI for tracking applications, its stiffness should be designed as small as possible with a large enough damping coefficient to avoid potential side effects. Other design requirements should also be considered in practice, such as the off-axis rigidity of the stage.

The works presented in this dissertation have been published in the following journal articles and patents:

- Dong X, Yoon D, Okwudire CE. *A novel approach for mitigating the effects of pre-rolling/pre-sliding friction on the settling time of rolling bearing nanopositioning stages using high frequency vibration*. Precision Engineering. 2017; 47:375–388.
- Dong X, Liu X, Yoon D, Okwudire CE. *Simple and robust feedforward compensation of quadrant glitches using a compliant joint*. CIRP Annals-Manufacturing Technology. 2017; 66(1):353–356.
- Dong X, Okwudire CE. *Detailed experimental evaluation of the compliant joint method for feedforward compensation of pre-motion friction*. 32rd Annual Meeting of American Society for Precision Engineering. 2017.
- Dong X, Okwudire CE. An experimental investigation of the effects of the compliant joint method on feedback compensation of pre-sliding/pre-rolling friction. Precision Engineering. 2018; 54:81–90.
- Dong X, Okwudire CE. *Semi-active joint for ultra-precision positioning using sliding/rolling bearings*. CIRP Annals-Manufacturing Technology.2019; 68(1):385–388.
- Dong X, Okwudire CE. *Influence of design parameters on the effectiveness of friction isolators in mitigating pre-motion friction in mechanical bearings*. Submitted to Mechatronics.
- Dong X, Yoon D, Okwudire, CE. *Axially compliant bearing for precision positioning*. Patent Filing # PCT/US2016/060033. Filed November 2, 2016. (Pending)
- Okwudire CE, Dong X. *Vibration Assisted Nanopositioning Stage*. US Patent. 2019; 10281829.

## 7.2 Future work

The vibration assisted nanopositioning (VAN) stage from Chapter 3 has relatively poor performance during circular tracking motions, with merely 5%-15% reductions in terms of the peak and RMS tracking errors. This may due to the fact that high frequency vibration (i.e., dither) is applied for the entire duration of circular motion [127]. By modulating the amplitude and oscillation pattern (e.g., waveform and duty cycle) of the applied dithering signal, up to 30% improvements in the tracking accuracy can be achieved, according to Syamsul et al. [127]. However, the results largely depend on the specific experimental setup and therefore, cannot be easily generalized to other systems with dither. Moreover, a large number of experimental trials are needed for each circular command to obtain the optimal dithering parameters, making it tedious and most importantly impractical. Therefore, rigorous theoretical analysis and experimental investigation are needed to optimize the amplitude, frequency and oscillation pattern of the dithering force in a systematic manner.

In addition, the proof-of-concept prototype VAN stage involves a lot of mechanical modifications on the existing nanopositioning (NP) stage, unnecessarily increasing the cost and complexity of the method. Other design ideas should be considered such as integrating the piezo actuators to the designed flexure that connects each bearing to the moving table of the stage. By doing so, the cost and complexity of the VAN approach can be greatly reduced. On the other hand, the additional actuators enable higher level control of the system. For instance, fine adjustments of stage's position can be carried out using the piezo actuators, leading to a multi-input-single-output control strategy that potentially reduces the settling time of the VAN stage.

As discussed in Appendix C.1, the stage with friction isolator (FI) settles slower than the stage without it during 50 $\mu$m point-to-point positioning tests, in the presence of a PID controller. By measuring both the table and bearing displacements of the friction-isolated NP stage, it is observed that this sluggish settling behavior is due to the bearing motion during settling, which poses significant difficulties for the PID controller to compensate the resultant disturbance force from the bearing motion. Therefore, an inverse-model-based disturbance (DOB) combined with the PID controller is used as a possible approach for addressing the adverse effects of bearing motion on the settling time of the friction-isolated (NP) stage in Appendix C.2. With the help of DOB, the stage with FI outperforms the stage without it (also controlled using a PID controller plus DOB) in point-to-point positioning tests with different step sizes ranging from 50 nm to 5

mm. Theoretical analysis using a model of the mechanical-bearing-guided NP stage with pre-motion friction dynamics is needed to complement the experimental studies presented in Appendix C, and to gain deeper insights into the dynamics of the FI as it interacts with friction. This will, for instance, help explain why the bearing motion is significant for the 50 $\mu$m step size compared to other step sizes evaluated in the experiments.

Although the benefits of FI are discussed in the context of linear NP stages, it has great potential of being widely applied in different precision motion applications due to its low cost, simplicity, excellent and robust performance. For example, a rotary version of FI has been designed and built to mitigate the undesirable effects of friction in high precision roll-to-roll machine. As seen from the preliminary simulation results in Appendix D, the friction-isolated rotary system, combined with a disturbance observer, achieves significantly improved tracking accuracy during constant velocity motions [141]. Future experiments are needed to validate the performance of FI using the prototype system. Other potential applications of the proposed methods should also be explored.

In addition, benefits and potential side effects due to the interactions of stage (servo) dynamics, friction dynamics and FI dynamics should be investigated through theoretical analysis. For instance, preliminary linear analysis has been carried out to study the dynamical phenomena of FI on a PID-controlled NP stage under LuGre friction dynamics [142]. It is shown that the addition of a FI shrinks the range of controller gains that can stabilize the NP stage [142]. Nonlinear analysis is also needed to understand the effects of FI on complex nonlinear phenomena such as limit cycles and chaotic oscillations.

A rudimental switching method is used during point-to-point positioning tests on the stage with semi-active isolator (SAI) in Chapter 5. Experimental and theoretical analyses are necessary to optimize the switching time for further reducing the settling time of the stage with SAI. In addition, Step II (i.e., Compensation) of the proposed two-step error mitigation scheme is developed based on the dynamics when the stage is at rest (i.e., no relative motion between the bearing and table). This leads to imperfect cancellation of the switching-induced error when the stage is moving during point-to-point motions, causing increases in settling times relative to the FI case. Therefore, a more robust method for generating the correction signal in Step II should be considered.

On the other hand, the switching-induced error during circular motions makes the proposed SAI unsuitable for tracking applications. Moreover, it is very hard to compensate this error without knowing the current states (e.g., deformation) of the flexure. A low cost sensor (e.g., strain gauge) can be integrated into the SAI prototype to measure the relative displacement between the bearing and table. Using this information, more effective algorithm can be developed for accurate and robust compensation of the switching-induced positioning errors during both point-to-point positioning and tracking motions.

Finally, due to the nonlinear transitions of friction between pre-motion and gross motion regimes, the frequency domain analysis from Section 6.3.2 is not capable of describing the settling behavior of the stage with FI during 5 mm point-to-point positioning motions. Nonlinear analysis is needed to understand the complex interactions between friction dynamics and servo dynamics, thus predicting the settling time during long range positioning. On the practical side, a systematic framework can be developed for optimal design of the FI, based on different performance metrics (e.g., settling time, in-position stability and tracking accuracy) as well as design constraints (e.g., dimension and off-axis stiffness).

# APPENDICES

# Appendix A

## Challenges with Control-based Feedback Compensation Approaches

### A.1 Challenges of model-free feedback controller in addressing slow settling problem

To illustrate the challenges of high gain controllers in addressing the undesirable effects of pre-motion friction, consider a servo-controlled mechanical-bearing-guided nanopositioning (NP) stage of mass $m$, depicted in Figure A.1. Suppose that a point-to-point positioning command, $x_r$, is given to the servo controller, the actual position, $x$, of the stage must reach $x_r$ as quickly as possible. However, the stage suffers from friction force $F_f$, which is represented by the Dahl model in Eq. (1.1). According to the Dahl model, there are two key problems associated with pre-motion friction which cause the slow settling problem in point-to-point motion, and create challenges for addressing it using model-free feedback compensation techniques:

- Problem I: when the displacement magnitude, $|x|$, is very small (<~100 nm), friction behaves like a quasilinear spring with a very large stiffness, $k_f = k_\sigma$ [48][50][51]. This stiff spring makes it difficult and slow for a controller with conservative gains to push the stage into its target position [13][53][54].
- Problem II: as $|x|$ increases, the spring stiffness of pre-motion friction decreases nonlinearly and drastically from $k_\sigma$ to a value of zero as $F_f$ approaches $F_C$, implying a nonlinear time-varying system, which is hard to control [48][49][62]-[65].

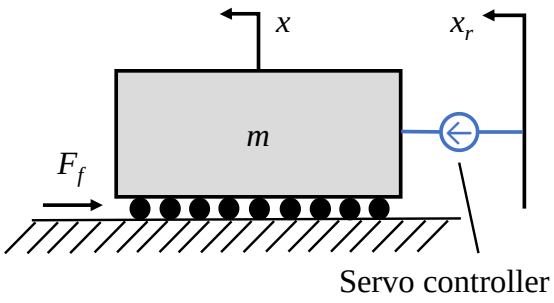


Figure A.1 Model of a servo-controlled NP stage under the influence of friction.

Table A.1 Parameters of an Aerotech ALS-130H NP stage used in simulation, obtained from Bucci et al. [54].

| Parameter | Value |
|---|---|
| $m$ | 1.5 kg |
| $K_P$ | 0.8 N/$\mu$m |
| $K_D$ | $8.5 \times 10^{-4}$ N·s/$\mu$m |
| $k_\sigma$ | 8 N/$\mu$m |
| $F_C$ | 1 N |

Assume the NP stage shown in Figure A.1 is controlled using the most basic and industry-standard PID-type controller (e.g., PID, P-PI and PI-P) [48][54]. It is preferable to keep the gains of the controller fixed, to maintain a linear time-invariant (LTI) structure. To deal with Problem I, such a controller must have high integral gain to enable it to quickly overcome the large stiffness of pre-motion friction and drive the stage to its target position, resulting in a high gain feedback controller [48][62][63][65]. Problem II exacerbates the issues introduced by using high integral gain to address Problem I (e.g., overshoots and limit cycles), because of the rapid and nonlinear changes in frictional stiffness (i.e., system parameter variations) [63][64].

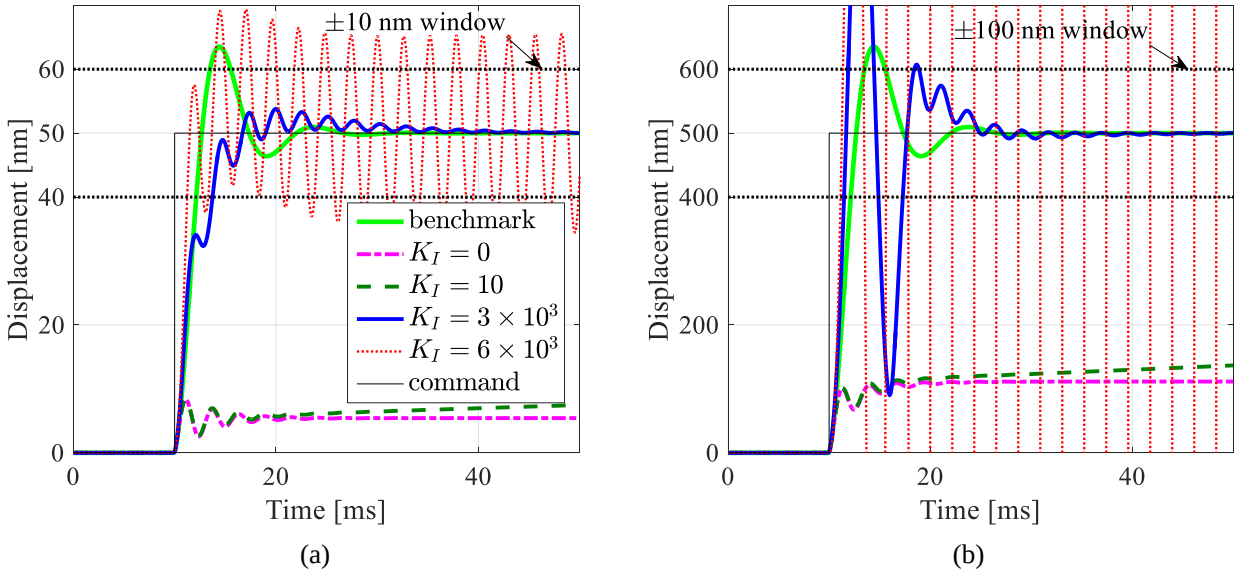


Figure A.2 Settling results with a PID-type LTI controller in response to (a) 50 nm, and (b) 500 nm step commands using different integral gains. In benchmark cases, no friction is considered and $K_I$ = 0. Unit of $K_I$ is N/($\mu$m·s).

Simulations are conducted using the PID-controlled stage model of Figure A.1, with proportional ($K_P$), integral ($K_I$) and derivative ($K_D$) gains. The parameters used for the simulation are those of an Aerotech ALS-130H NP stage, reported in a recent paper by Bucci et al. [54] and summarized in Table A.1. Two step commands with magnitudes 50 nm and 500 nm are used to simulate the settling performance of the stage in the quasilinear and nonlinear regions of pre-motion friction, respectively. In each case, a ±20% settling window is used, to facilitate easy comparison. The benchmark settling behavior of the stage to the desired positions is taken as the case where $F_f$ = 0 and $K_I$ = 0, because integral action is not needed for settling in the absence of friction. Notice that when $F_f$ (given by the parameters of the Dahl model in Table A.1) is applied, the stage cannot settle into the desired windows with $K_I$ = 0 in both cases due to the very large initial contact stiffness ($k_\sigma$ = 8 N/$\mu$m) of friction. The overall settling performance can be improved by increasing $K_I$, as evidenced by the fact that the best settling time (in response to the 50 nm step command) for $K_I$ values ranging from 0 to $10^4$ N/($\mu$m·s), which occurs at $3 \times 10^3$ N/($\mu$m·s), is 33% shorter than that of the benchmark case. However, using such a high value of $K_I$ to reduce settling time adversely affects the stability margins of the control system, as indicated by the oscillations

of the displacement signal when $K_I = 3 \times 10^3$ N/($\mu$m·s) in Figure A.2(a). This loss of stability margins could easily lead to performance degradation or instability if friction behavior varies or a larger magnitude reference signal is used, as can be seen from Figure A.2(b). In response to the 500 nm step command, the stage suffers from a very large overshoot when using $K_I = 3 \times 10^3$ N/($\mu$m·s) (which worked very well for the 50 nm step), resulting 31% longer settling time than the benchmark case. For both step commands, increasing $K_I$ to $6 \times 10^3$ N/($\mu$m·s) causes stability issues, as indicated by the limit cycle in Figure A.2(a), and unstable response in Figure A.2(b). Therefore, in practice, when using a PID controller, $K_I$ is often tuned conservatively to prevent the issues associated with high gain feedback.

## A.2 Model-based feedback friction compensating controller and its challenges

To exemplify some of the robustness and stability issues of feedback friction compensation approaches due to their implicit or explicit dependence on a model of friction (i.e., model-based feedback compensation), let us consider the Nonlinear Integral Action Settling Algorithm (or NIASA for short), recently proposed by Bucci et al. [54][61]. NIASA is a controller that replaces the fixed integral gain, $K_I$, of a regular PID controller with a nonlinear function, $K_I(x)$, given by

$$K_I(x) = \frac{1}{\tau_d}\left[ k_\sigma \left( 1 - \frac{F_f}{F_c} \operatorname{sgn} \dot{x} \right) + K_P \right] \tag{A.1}$$

where $\underline{\tau_d}$ is a design time constant. Notice that $K_I(x)$ includes a nonlinear portion that varies in proportion to the effective spring stiffness of the Dahl friction model in Eq. (1.1). Thus, NIASA is a representative of feedback friction compensating controllers in which the integral gain is continuously switched, following the Dahl friction model.

Figure A.3 shows the simulated settling responses of NIASA to the same 50 nm and 500 nm step commands considered in Figure A.2, using all the parameters given in Table A.1 with $\tau_d$ = 4 ms [61]. A multiplicative uncertainty parameter $\delta \in [-1, \infty)$ is introduced by Bucci et al. into the initial contact stiffness, $k_\sigma$, of the Dahl model described in Eq. (1.1) to help demonstrate the robustness of NIASA to changing friction; i.e., $k_\sigma = k_{\sigma,n}(1 + \delta)$, where $k_{\sigma,n} = 8$ N/$\mu$m is the nominal value of $k_\sigma$. It is observed that NIASA is indeed stable within the uncertainty parameter band $\delta \in$

[–0.5, 1] that is tested by Bucci et al. [61]. However, observe from Figure A.3 that its settling performance varies significantly as $\delta$ deviates from its nominal value of zero. Notice also that the system with NIASA experiences severe oscillations for $\delta$ = –0.5, and suffers from a limit cycle with large amplitude for $\delta$ = –0.65, causing it to not settle within the desired ±10 nm window, as shown in Figure A.3(a). Similarly, the responses of the system in Figure A.3(b) (e.g., its overshoot and settling time) are also highly affected by changes in $\delta$.

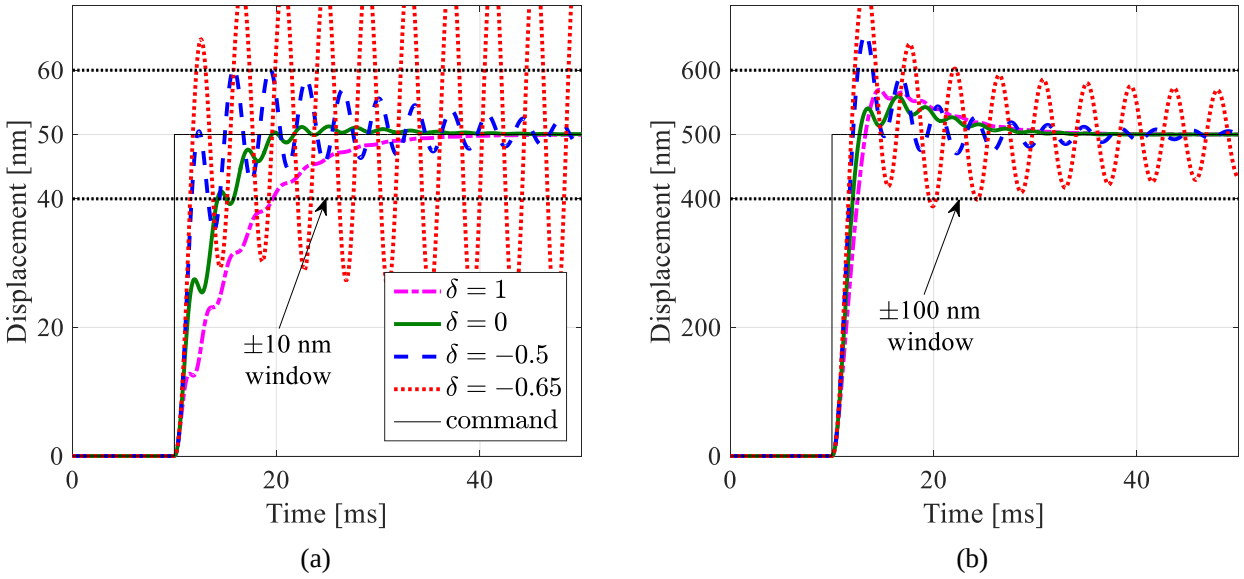


Figure A.3 Settling results with NIASA in response to (a) 50 nm, and (b) 500 nm step commands using different values of uncertainty $\delta$ in the initial contact stiffness of the Dahl model. Note that $k_\sigma = k_{\sigma,n}(1 + \delta)$, where $k_{\sigma,n}$ = 8 N/$\mu$m is the nominal value of $k_\sigma$.

## Appendix B

## Effects of Dither on Mitigating Pre-motion Friction

Consider the mechanical-bearing-guided nanopositioning (NP) stage of Figure A.1, controlled by a PID-type controller with $K_I = 0$, making it a PD-controlled stage. A sinusoidal dithering force ($F_d$) of amplitude $a\omega^2$ and circular frequency $\omega$ is applied to the stage in order to mitigate the friction force, $F_f$, which is dominated by pre-motion friction. The equation of motion of the error dynamics ($e = x_r - x$) during settling (over which time $\dot{x}_r = \ddot{x}_r = 0$) can be expressed as

$$m\ddot{e} + K_D\dot{e} + K_P e = F_f - a\omega^2 \sin\omega t \Rightarrow \ddot{E} + 2\zeta\dot{E} + E = f_f - \bar{a}\Omega^2 \sin\Omega\tau \tag{B.1}$$

The equation written in terms of $E$ is in non-dimensional form based on the following definitions

$$\begin{aligned} &E = \frac{e}{L};\ \dot{E} = \frac{dE}{d\tau} = \frac{1}{\omega_n L}\frac{de}{dt};\ \ddot{E} = \frac{d^2E}{d\tau^2} = \frac{1}{\omega_n^2 L}\frac{d^2e}{dt^2};\ \omega_n = \sqrt{\frac{K_P}{m}};\ \zeta = \frac{K_D}{2m\omega_n};\\ &\bar{a} = \frac{a}{mL};\ \Omega = \frac{\omega}{\omega_n};\ f_f = \frac{F_f}{m\omega_n^2 L} \end{aligned} \tag{B.2}$$

where $L$ is an arbitrary length quantity used to make $e$ dimensionless and $\tau = \omega_n t$ is non-dimensional time.

One powerful tool that is often used to study the effects of dither on dynamical systems is called the Method of Direct Partition of Motion (MDPM) [121][122]. It assumes that, under the influence of dither, the system dynamics can be partitioned into two components – the slow and the fast dynamics. The slow dynamics, which pertains to the actual stage motion, is assumed to have a much larger time constant than the fast dynamics occurring due to dither. The implication is that the dithering frequency, $\omega$, is much higher than the equivalent bandwidth, $\omega_n$, of the PD-controlled stage (i.e., $\Omega >> 1$). Accordingly, the error dynamics can be split as follows

$$E(\tau) = E_s(\tau) + \Omega^{-1}\phi(\tau, T) \tag{B.3}$$

where $T = \Omega\tau$ represents the non-dimensional fast time (note that $\tau$ is called the slow time); $E_s$ describes the slow motions – i.e., the motions of primary interest; $\phi$ represents the zero-mean fast motions occurring due to dither; i.e.

$$\langle \phi(\tau, T) \rangle = \frac{1}{2\pi}\int_0^{2\pi} \phi(\tau, T)\, dT = 0 \tag{B.4}$$

where the operator <·> averages its argument over one period $T$ of fast excitations, with the slow time $\tau$ assumed to be fixed. If $\dot{E}$, $\dot{\phi}$ and $E'$, $\phi'$ are used to denote derivatives of $E$ and $\phi$ with respect to $\tau$ and $T$, respectively, Eq. (B.1) can be written as

$$\left(\ddot{E}_s + \Omega^{-1}\ddot{\phi} + 2\dot{\phi}' + \Omega\phi''\right) + 2\zeta\left(\dot{E}_s + \Omega^{-1}\dot{\phi} + \phi'\right) + \left(E_s + \Omega^{-1}\phi\right) = f_f - \bar{a}\Omega^2 \sin\Omega\tau \tag{B.5}$$

The average operator is then applied to both sides of Eq. (B.5) to determine the slow dynamics, $E_s$, as

$$\ddot{E}_s + 2\zeta\dot{E}_s + E_s = \langle f_f \rangle \tag{B.6}$$

Note that all the terms involving $\phi$ and its derivatives do not show up in the averaged equation because they have zero mean. The force of friction can be described by the Dahl model of Eq. (1.1), given in non-dimensional form as

$$\dot{f}_f = \bar{k}_\sigma\left(1 - \frac{f_f}{f_c}\operatorname{sgn}\left(-\dot{E}\right)\right)\left(-\dot{E}\right) = \bar{k}_\sigma\left(-\dot{E} - \frac{f_f}{f_c}\left|\dot{E}\right|\right) \tag{B.7}$$

where

$$\bar{k}_\sigma = \frac{k_\sigma}{m\omega_n^2};\;\; f_c = \frac{F_c}{m\omega_n^2 L} \tag{B.8}$$

Applying the average operator to $\dot{f}_f$ yields

$$\left\langle \dot{f}_f \right\rangle = \bar{k}_\sigma \left( -\left\langle \dot{E} \right\rangle - \frac{1}{f_c} \left\langle f_f \left| \dot{E} \right| \right\rangle \right) \tag{B.9}$$

The fast motion $\phi$ can be solved by rearranging Eq. (B.5) as

$$\phi'' = -\Omega \bar{a} \sin \Omega\tau - \underbrace{\Omega^{-1} \left\{ \left[ \left( \ddot{E}_s + 2\dot{\phi}' \right) + \left( 2\zeta \dot{E}_s + 2\zeta\phi' \right) + E_s - f_f \right] + \Omega^{-1} \left( \ddot{\phi} + 2\zeta\dot{\phi} + \phi \right) \right\}}_{\approx 0} \tag{B.10}$$

Note that the term in the curly bracket is negligible because it is pre-multiplied by $\Omega^{-1}$, which is a small number. Therefore, the stationary solution for $\phi$ is obtained from Eq. (B.10) as

$$\phi \approx \bar{a}\Omega \sin \Omega\tau \tag{B.11}$$

Hence the solution of the error dynamics (given by Eq. (B.3)) is

$$E = E_s + \bar{a} \sin \Omega\tau \tag{B.12}$$

Substituting Eq. (B.12) into Eq. (B.9), the averaged friction dynamics is then given by

$$\left\langle \dot{f}_f \right\rangle = \bar{k}_\sigma \left( -\dot{E}_s - \frac{1}{f_C} \left\langle f_f \left| \dot{E}_s + \bar{a}\Omega \cos \Omega\tau \right| \right\rangle \right) \tag{B.13}$$

During settling, the velocity of the stage is close to zero. Therefore, $|\dot{E}_s - \bar{a}\Omega\cos\Omega\tau| \approx |\bar{a}\Omega\cos\Omega\tau|$, assuming that $\bar{a}$ and $\Omega$ are high enough such that $|\bar{a}\Omega\cos\Omega\tau| >> |\dot{E}_s|$. Moreover, the force of friction can also be partitioned into two components

$$f_f = f_{fs} + f_{fd} \tag{B.14}$$

where $f_{fs}$ is the slow portion related to $E_s$ and $f_{fd}$ is the fast zero-mean sinusoidal portion related to $\bar{a}\Omega\cos\Omega\tau$. Since $|\bar{a}\Omega\cos\Omega\tau| >> |\dot{E}_s|$

$$\left\langle \dot{f}_f \right\rangle \approx \left\langle \dot{f}_{fd} \right\rangle = 0 \Rightarrow \left\langle f_f \right\rangle = \left\langle f_{fs} \right\rangle = -\frac{f_c}{\left\langle \left|\bar{a}\Omega\cos\Omega\tau\right| \right\rangle}\dot{E}_s = -\frac{\pi f_c}{2\bar{a}\Omega}\dot{E}_s \tag{B.15}$$

Substituting $< f_f >$ from Eq. (B.15) into Eq. (B.6) gives the slow (or averaged) dynamics of the stage under dither as

$$\ddot{E}_s + 2\zeta_{eq}\dot{E}_s + E_s = 0; \quad \text{where } \zeta_{eq} = \zeta + \frac{\pi f_c}{4\bar{a}\Omega} \tag{B.16}$$

The implication of Eq. (B.16) is that the averaged dynamics of the PD-controlled NP stage is linear second order and does not contain any stiffness terms due to friction. As the amplitude and frequency of dither increase, the equivalent damping $\zeta_{eq}$ approaches to the damping ratio of the frictionless stage (i.e., $\zeta$). It can be shown that this change of damping ratio is the reason for the presence of a canyon in the 3D plots of Figure 3.4; essentially, lower damping ratio eliminates sluggishness in response and facilitates quick settling up to a point, after which it starts to hurt settling performance due to increased oscillations.

The above analysis is validated by comparing settling results of the PD-controlled NP stage using direct simulations of the full dynamics (Eq. (B.1)) and averaged dynamics (Eq. (B.16)), respectively, see Figure B.1; note that a sinusoidal dithering force with amplitude $a\omega^2$ = 2 N and frequency $\omega$ = $10^4$ rad/s is applied. It is observed that the response of the full dynamics is a superposition of the fast oscillation on the slow dynamics, and the response of the averaged dynamics is in good agreement with the slow portion of the total response, when extracted using a $4^{th}$ order Butterworth filter with cutoff frequency of 500 Hz. However, the excessive vibration (or fast oscillation) severely jeopardizes the positioning performance of the NP stage as discussed in Section 3.1.

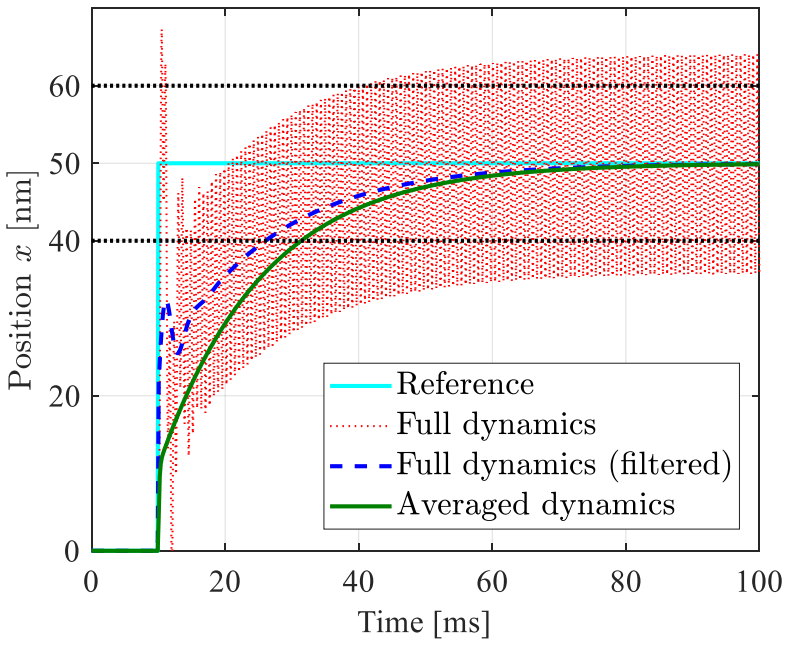


Figure B.1 Settling results of a PD-controlled NP stage using direct simulations of full dynamics and averaged dynamics. Note that $a\omega^2 = 2$ N and $\omega = 10^4$ rad/s are used.

# Appendix C

## Effects of Friction Isolator on Feedback Compensation of Pre-motion Friction

### C.1 Sluggish settling of friction-isolated nanopositioning stage during 50 $\mu$m point-to-point motions

In Chapter 4, the settling performance of the proposed friction isolator (FI) is experimentally evaluated using point-to-point positioning tests with 5 mm and 5 $\mu$m step sizes. It is also of interest to investigate how FI performs for a wide range of step sizes. Therefore, point-to-point motion profiles of various step sizes ranging from 50 nm to 5 mm are tested. The time taken for each step to settle into a ±25 nm window is evaluated using the following cases:

- No FI: in-house built mechanical-bearing-guided nanopositioning (NP) stage of Figure 4.2; note that fixtures are implemented to de-active the FIs.
- FI: in-house built mechanical-bearing-guided NP stage of Figure 4.2 equipped with the designed FI prototypes.

Figure C.1 summarizes the mean settling times, together with the corresponding one-standard-deviation band, of the stage with and without FI into the ±25 nm window during point-to-point motions of different step sizes (50 trials for each step size). For all but one of the step sizes evaluated, the FI case exhibits much faster and robust settling than the No FI case. The exception is the 50 $\mu$m step size for which the stage with FI settles much slower and is much less robust than the stage without FI.

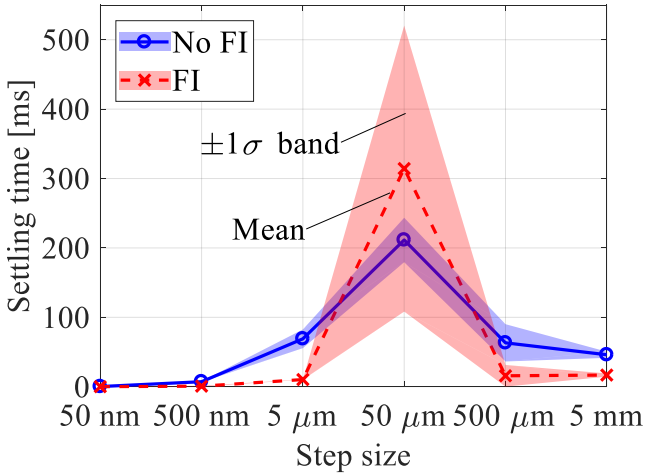


Figure C.1 Settling times of the No FI case and FI case into the ±25 nm window during point-to-point motions of varying step sizes. The lines represent mean settling time values during 50 trials of each step size and the shaded bands indicate ±1$\sigma$ (standard deviation).

To illustrate the reason behind this discrepancy, Figure C.2 and Figure C.3 compare the typical settling performance of the stage with and without FI during point-to-point motions with 5 $\mu$m and 50 $\mu$m step sizes. During the first step of the 5 $\mu$m case (as highlighted in the subplot), the No FI case takes 47.8 ms to settle, which is very long relative to the duration of the step command (i.e., 17.7 ms); however, the FI case settles within 10.5 ms (i.e., 78% faster). Similarly, during the eighth step, the FI case takes 10.2 ms to settle, i.e., 88% faster than the No FI case (which takes 85 ms to settle). Similar improvements in settling time are seen for all 16 steps (8 steps forward and 8 steps backward) such that the mean settling time of the stage with FI (i.e., 10.3 ms) is 85.1% faster than that of the stage without FI (i.e., 69.1 ms). Figure C.3 compares the settling response of the stage with and without FI for the problematic 50 $\mu$m step size. During the first step, the No FI case takes 237 ms to settle, while the FI case only takes 43.6 ms to settle, leading to 81.6% reduction in settling time. However, it is observed that the settling time of the FI case gradually increases as the stage steps in the same direction. By the eighth step (as highlighted in the subplot), the settling time of the FI case has increased to 453 ms, which is even longer than that of the No FI case (i.e., 214 ms). This drastic change leads to the overall longer mean settling time and larger one-standard-deviation band during the 50 $\mu$m step size for the stage with FI, compared to the stage without it.

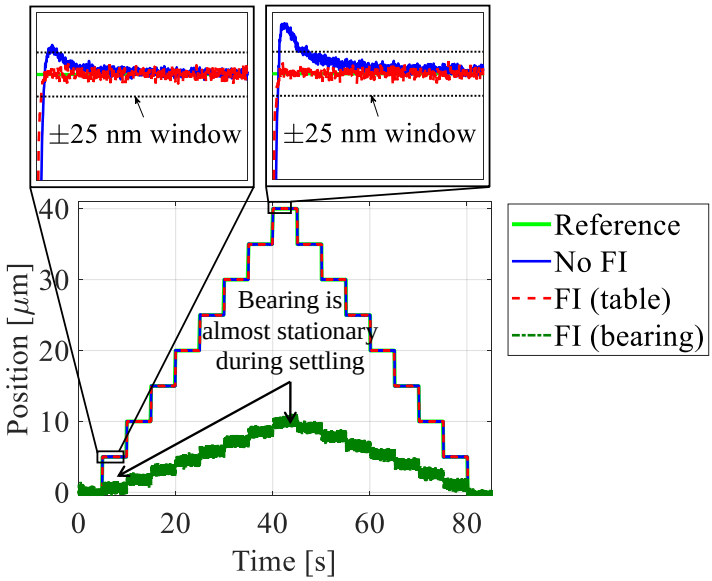


Figure C.2 Typical settling performance of the stage with and without FI into the ±25 nm window during 5 $\mu$m point-to-point motion. The bearing motion of the FI case is also plotted in addition to its table motion. Note that the bearing and table motions of the No FI case are identical.

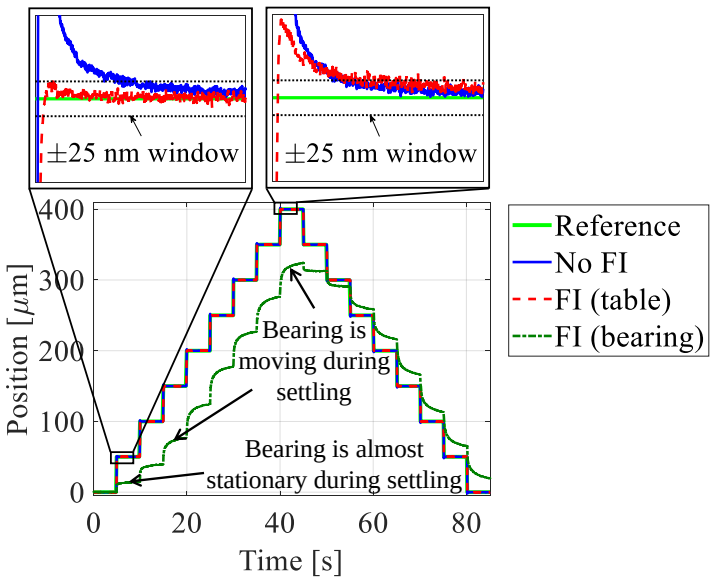


Figure C.3 Typical settling performance of the stage with and without FI into the ±25 nm window during 50 $\mu$m point-to-point motion. The bearing motion of the FI case is also plotted in addition to its table motion. Note that the bearing and table motions of the No FI case are identical.

In addition to the position measurement of the table (from the linear encoder), a laser displacement sensor (Keyence, LA-G10) is used to measure the absolute position of one of the bearings of the stage with FI, see Figure C.4. As shown in Figure C.2 and Figure C.3, the bearing is assumed to be at the same position as the table at the start of the point-to-point motion such that the FI does not experience any tension/compression. It is observed that the motion of the bearing always lags behind that of the table for both the 5 $\mu$m and 50 $\mu$m step sizes. Observe that, during all the 5 $\mu$m steps, the bearing is more or less stationary during settling. However, with the problematic 50 $\mu$m steps, the bearing is almost stationary during settling for steps 1 and 2, but it begins to move significantly during settling for subsequent steps. A similar pattern is repeated during the backward motion.

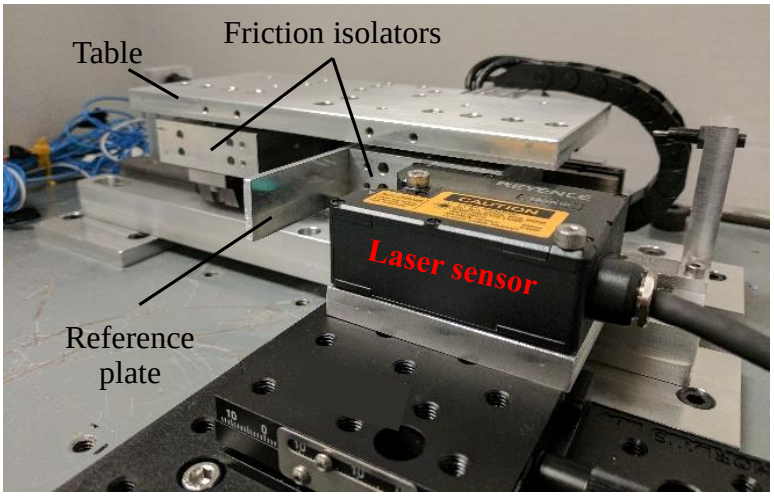


Figure C.4 Experimental setup for measuring bearing motion of the in-house built NP stage equipped with FIs.

To illustrate how the motion of the bearing affects the settling time of the stage with FI, Figure C.5 shows a schematic of its table and bearing motions during settling. As is typical (see Figure C.2 and Figure C.3), the table of position $x_t$ overshoots its target position ($x_r$), indicating that the servo force $F_a$, is larger than the tension force $F_{fi}$ from the FI (of stiffness $k_{fi}$). In order to bring the table back to the target position, the PID controller works on reducing $F_a$ to a similar or smaller level as $F_{fi}$. If the velocity ($dx_b/dt$) of the bearing is close to zero, $F_{fi}$ remains almost unchanged as the PID controller reduces $F_a$ (where $t$ represents time). However, if the bearing is

moving towards the table (i.e., $dx_b/dt > 0$), $F_{fi}$ decreases as the PID controller is reducing $F_a$, i.e., $F_{fi}$ becomes a moving target. Consequently, the task of the PID controller to bring $F_a$ to similar or smaller levels as $F_{fi}$ becomes more difficult with $dx_b/dt > 0$ compared to $dx_b/dt \approx 0$, resulting in elongated settling time.

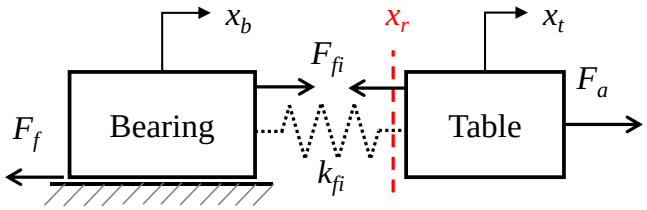


Figure C.5 Schematic of table and bearing motions of the stage with FI during settling, explaining the reason for long settling time when $dx_b/dt > 0$ compared to when $dx_b/dt \approx 0$.

## C.2 Experimental evaluation of friction isolator on PID controller combined with disturbance observer

### C.2.1 Inverse-model-based disturbance observer

From the experimental results in Section C.1, it is found that the relatively poor settling performance of the 50 $\mu$m steps using the PID controller alone on the stage with FI is due to the disturbance force created by the bearing motion. Consequently, it is hypothesized that adding a disturbance observer (DOB) to the PID controller will improve the settling time of the stage with FI compared to the stage without it, including the 50 $\mu$m case. The rationale is that the DOB makes the PID controller aware of the disturbance forces created by the bearing motion; therefore, it enables the PID controller to counteract the disturbance faster, thus resulting quicker settling.

Figure C.6 shows the block diagram of the control scheme with an inverse-model-based DOB [66][75][143]-[145], where $C$ and $G$ represents the PID controller and measured open loop plant dynamics, respectively. The DOB estimates the disturbance forces by subtracting the control command from the estimated input command obtained by the inverse of a nominal plant model, $G_n$. A low pass filter, known as the $Q$ filter, is added to guarantee stability [66][75][143]-[145].

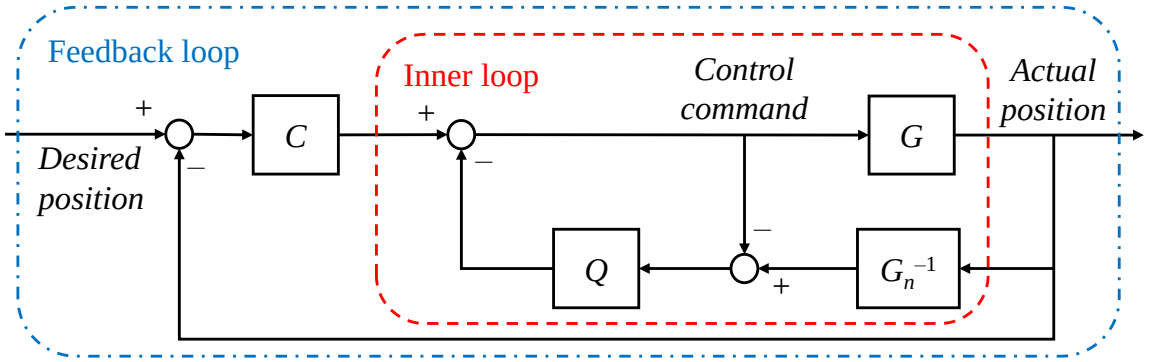


Figure C.6 Block diagram of the control scheme with PID controller (*C*) and an inverse-model-based disturbance observer (DOB).

The nominal plant model of the stage with and without FI is chosen as a standard second order model [66][75][144], describing the low frequency characteristics of most nanopositioning (NP) stages which is dominated by rigid body dynamics

$$G_n(s) = \frac{Z}{s(s+P)} \tag{C.1}$$

The parameters *P* and *Z* of the nominal models are obtained through least-squares-fitting of the low frequency portion of the measured plant dynamics in the gross motion regime. Specifically, frequencies below 100 Hz of the 1.5A-input FRFs of the stage with and without FI (see Figure 4.4) are used to obtain *P* and *Z*, as summarized in Table C.1. Due to the dynamics of the FI, the low frequency portion of the measured FRF of the FI case has some differences compared to that of the No FI case. Therefore, different parameters are obtained for the stage with and without FI; however, they both represent the best fit under the same nominal plant structure given by Eq. (C.1). A second order low pass filter is adopted for *Q*; it is given by

$$Q(s) = \frac{(2\pi f_Q)^2}{(s+2\pi f_Q)^2} \tag{C.2}$$

with its cutoff frequency (i.e., bandwidth) tuned to $f_Q$ = 200 Hz for both the stage with and without FI.

Table C.1 Identified parameters of the nominal plant models of the stage with and without FI.

| | No FI | FI |
|---|---|---|
| $P$ [1/s] | 120 | 244 |
| $Z$ [N/(A·kg)] | 7.9 | 13.8 |

### C.2.2 Frequency domain evaluation

To understand the effects of DOB on the feedback system, an equivalent block diagram of it is often adopted [144][145]. As shown in Figure C.7, the equivalent controller form of the DOB is given by

$$C_{DOB}(s) = (1-Q)^{-1} Q G_n^{-1} \tag{C.3}$$

Substituting Eq. (C.1) and Eq. (C.2) into Eq. (C.3)

$$C_{DOB}(s) = \frac{(2\pi f_Q)^2}{Z} \cdot \left( \frac{s+P}{s+4\pi f_Q} \right) \tag{C.4}$$

The resulting feedback controller form of the DOB is equivalent to a lead compensator (since $P << 4\pi f_Q$ for both the stage with and without FI) whose gain is dominated by $f_Q$. A larger $f_Q$ leads to higher bandwidth of the DOB; however, $f_Q$ is often limited in practice by the un-modeled dynamics of the nominal model $G_n$, compared to the actual plant dynamics $G$, especially at high frequencies.

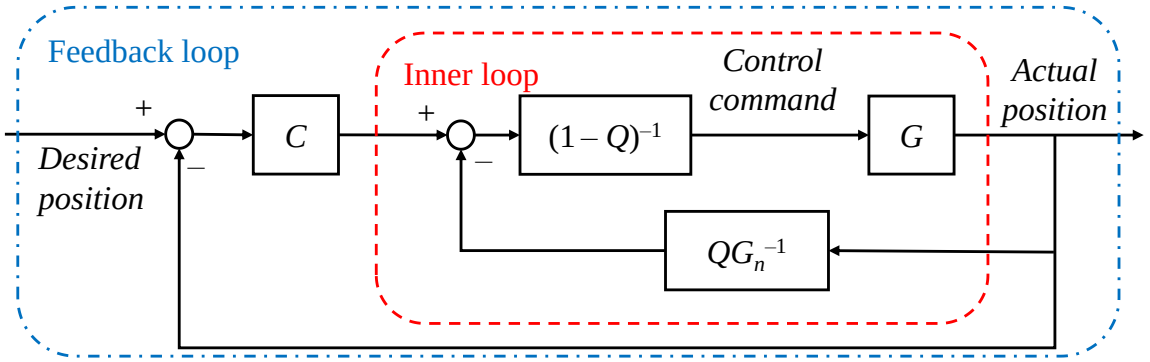


Figure C.7 Block diagram of the control scheme with a PID controller ($C$) and the equivalent form of DOB.

To analyze the tradeoff between performance and stability when designing the $Q$ filter, the augmented plant dynamics (i.e., closed loop dynamics of the inner loop shown using dashed lines in Figure C.6 and Figure C.7) can be obtained as

$$G_{aug}(s) = \frac{G(s)G_n(s)}{G_n(s) + \big(G(s) - G_n(s)\big)Q(s)} \tag{C.5}$$

Figure C.8 and Figure C.9 show the measured FRFs of the augmented plant and closed loop dynamics for different input amplitudes using the DOB together with the PID controller discussed in Section 4.3 for the stage with and without FI. At frequencies below the $Q$ filter's cutoff frequency, the effects of the friction-induced resonance become less dominant for the No FI case. This is because the augmented plant dynamics approaches to the nominal model (which only experiences gross motion friction) below the $Q$ filter's cutoff frequency of 200 Hz (i.e., $G_{aug}(s) \rightarrow G_n(s)$ as $|Q(s)| \rightarrow 1$). As a result, the closed loop bandwidth at medium-to-low input amplitudes is improved as shown in Figure C.10(a). However, the friction-induced resonance of the stage without FI at very small input amplitude remains largely unchanged in the augmented plant dynamics because its frequency is higher than the bandwidth of the $Q$ filter (i.e., $G_{aug}(s) \rightarrow G(s)$ as $|Q(s)| \rightarrow 0$). This eventually leads to significant drops (below 0 dB) of the closed loop FRF magnitudes when the input amplitude is very small (less than 0.1 A) and pre-motion friction dominates. As a result, the −3 dB closed loop bandwidth of the No FI case is reduced from its original value of 200 Hz in the gross motion regime to less than 50 Hz in the pre-motion regime

as shown in Figure C.10(a). To further improve the bandwidth, the cutoff frequency of the $Q$ filter must be increased such that the friction-induced resonance at very small input amplitudes can be effectively attenuated. However, such a high bandwidth $Q$ filter could easily cause stability issues due to the fact that non-rigid-body dynamics (at high frequencies) are not included in the nominal model; hence the modeling errors at high frequencies are large [66].

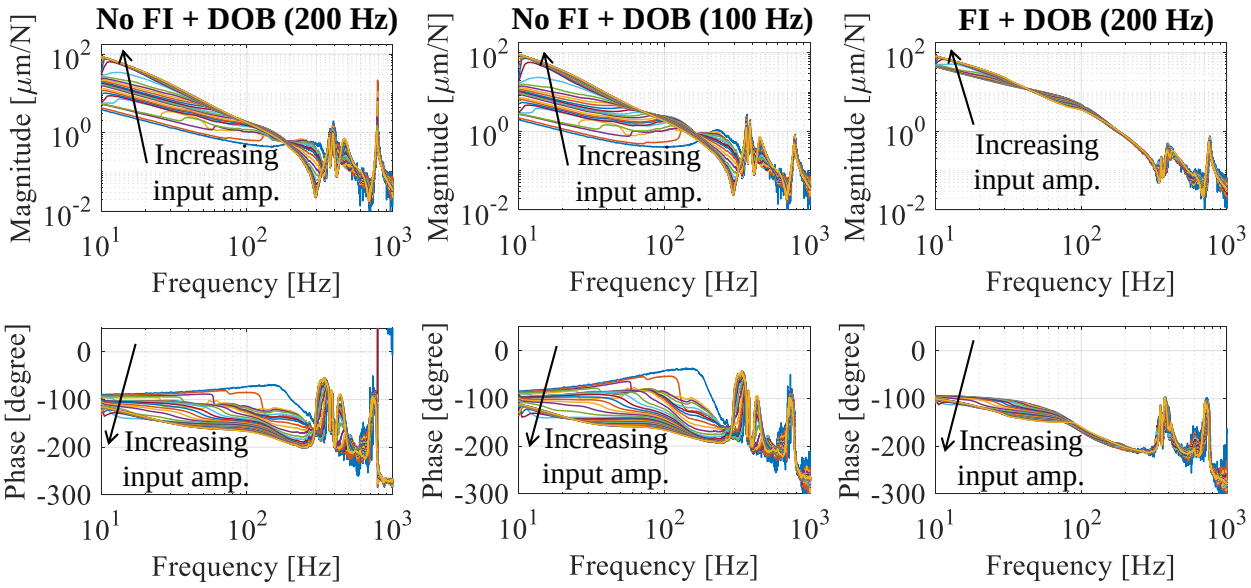


Figure C.8 Frequency response functions (FRFs) of augmented plant dynamics for the stage with and without FI using different input amplitudes. The control scheme shown in Figure C.6 and Figure C.7 are used. The bandwidth of the DOB for the No FI case is reduced to 100 Hz to guarantee stability (as discussed in Section C.2.3).

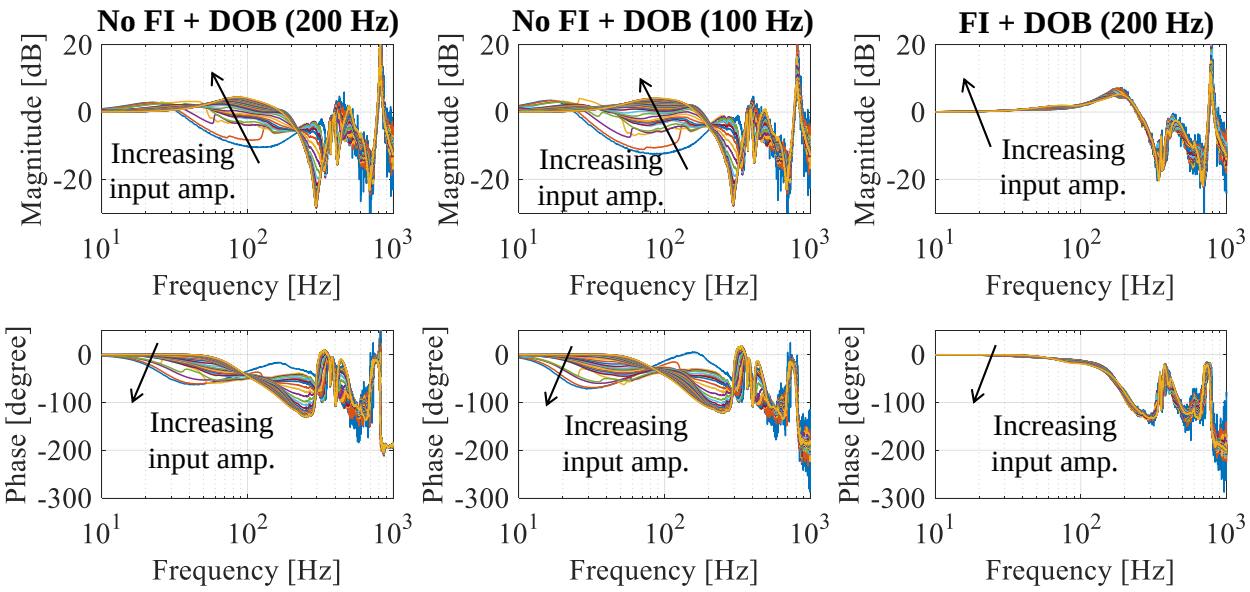


Figure C.9 Frequency response functions (FRFs) of closed loop dynamics for the stage with and without FI using different input amplitudes. The control scheme shown in Figure C.6 and Figure C.7 are used. The bandwidth of the DOB for the No FI case is reduced to 100 Hz to guarantee stability (as discussed in Section C.2.3).

For the stage with FI, the friction-induced resonance is effectively mitigated for all input amplitudes, since its frequency is always well below the 200 Hz cutoff frequency of the $Q$ filter. As a result, the augmented plant's FRFs exhibit much less variations (nonlinearity) as shown in Figure C.10(b). This makes it very easy for the PID controller to control the augmented plant of the FI case, leading to much more linear closed loop dynamics and uniformly higher bandwidth, compared to the No FI case.

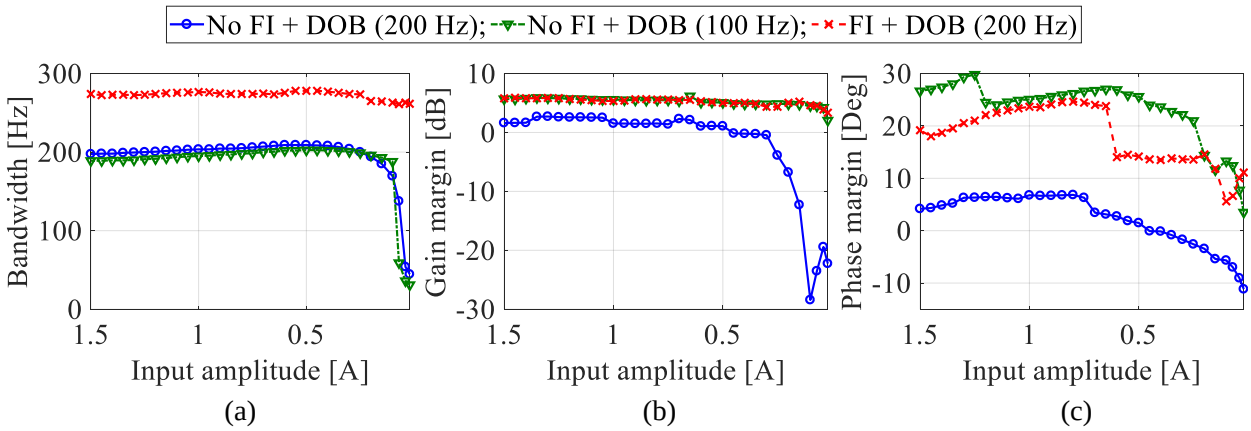


Figure C.10 Calculated (a) closed loop bandwidth (based on –3 dB criterion), (b) gain, and (c) phase margins of the stage with and without FI using PID controller combined with DOB. The DOB of 200 Hz bandwidth is stable on the FI case but unstable on the No FI case. The bandwidth of the No FI case's DOB is reduced to 100 Hz to guarantee stability (as discussed in Section C.2.3).

To compare the stability of the stage with and without FI in the presence of DOB, Figure C.10 shows the calculated gain and phase margins of both cases with different input amplitudes. When the DOB is implemented with a cutoff frequency of 200 Hz, the stability margins of the No FI case at gross motion regime become very small, indicating that the closed loop system is very sensitive to any un-modeled dynamics or variations in parameters (i.e., poor robustness). Moreover, as the input amplitude reduces (and pre-motion friction becomes more dominant), the stability margins of the No FI case drop significantly and eventually become less than zero. This leads to an unstable LTI system when the stage without FI operates in the pre-motion regime, implying that the original nonlinear system also suffers from stability issues. However, the stability margins of the stage with FI are uniformly larger than that of the stage without FI and always stay above zero, showing that the closed loop system is much more robust. Moreover, the gain margin remains almost unchanged as the input amplitude varies, thanks to the reduced nonlinearity and more consistent augmented plant dynamics of the FI case for both pre-motion and gross motion regimes of friction.

### C.2.3 Point-to-point positioning tests

Point-to-point positioning tests are carried out on the stage with and without FI using the same motion profiles discussed in Section C.1. The same PID controller as Section C.1 is used on both cases. However, while the DOB tuned in Section C.2.1 works for the FI case, it leads to instability when used on the No FI case, as predicted by the stability margin plots of Figure C.10. Figure C.11 shows an example of the instability of the stage without FI during point-to-point motions of 5 mm step size using the 200 Hz bandwidth DOB. During settling, the stage suffers from severe oscillations such that it is not able to settle within the desired ±25 nm window. Reducing the bandwidth of the *Q* filter to 150 Hz reduces but does not fully mitigate the oscillations. Therefore, the cutoff frequency of the *Q* filter is further reduced to 100 Hz, which is stable from the frequency domain standpoint (see Figure C.10), as well as in time domain (for all the step sizes tested). Therefore, for all the point-to-point positioning tests conducted in the rest of this section, a 100 Hz bandwidth DOB is used for the stage without FI, while a 200 Hz bandwidth DOB is used for the friction-isolated NP stage (because it is stable for all the step sizes tested).

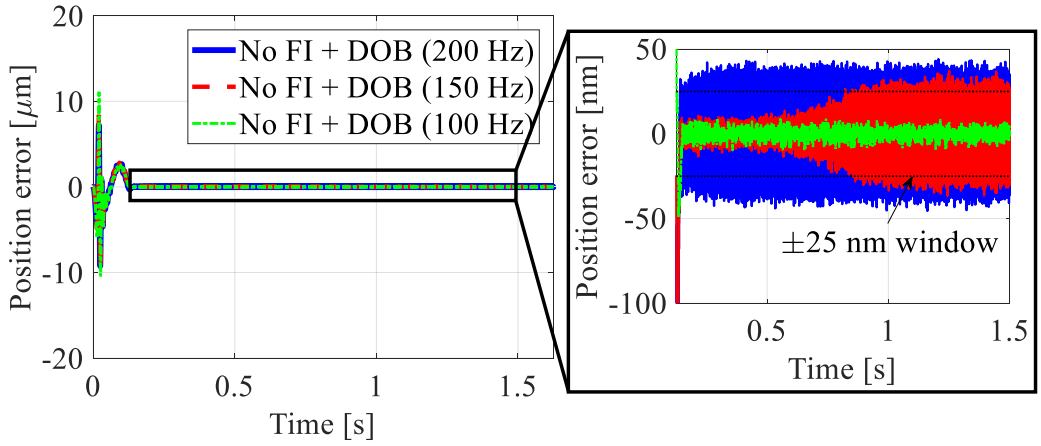


Figure C.11 Typical positioning performance of the No FI case with DOB during 5 mm point-to-point motion. The stage suffers from severe oscillations during settling when the cutoff frequency of the DOB is set to 150 Hz and 200 Hz.

Figure C.12 summarizes the mean settling times, together with the corresponding one-standard-deviation band, of the stage with and without FI into a ±25 nm window during point-to-point motions of different step sizes (50 trials for each step size). It is observed that the settling

time of the No FI case varies a lot within the same step size, and as the step size changes. The performance variations within the same step size are due to the changes in friction dynamics from position to position along the travel range of the stage. On the other hand, the FI case achieves uniformly much better settling performance with superior robustness compared to the No FI case, resulting no less than 48% and up to 98% reductions of the mean settling time. Moreover, the much slower and less robust settling performance of the stage with FI during point-to-point motions with 50 $\mu$m step size is eliminated.

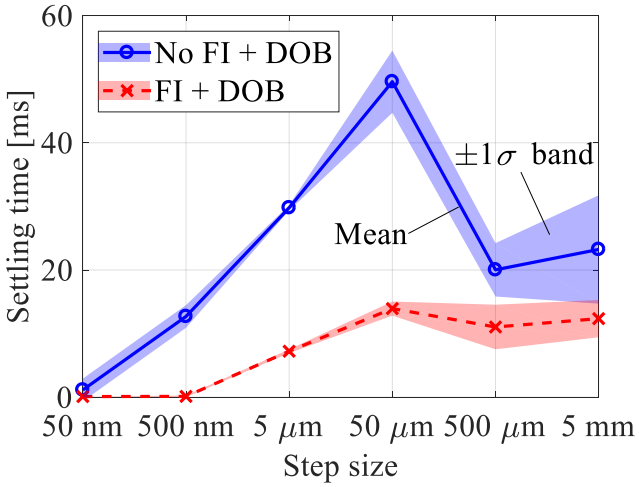


Figure C.12 Settling times of the No FI case and FI case with DOB into the ±25 nm window during point-to-point motions of varying step sizes. The lines represent mean settling time values during 50 trials of each step size and the shaded bands indicate ±1$\sigma$ (standard deviation).

Figure C.13 and Figure C.14 compare the typical settling performance of the stage with and without FI in the presence of DOB during point-to-point motions with 5 $\mu$m and 50 $\mu$m step sizes. During the 5 $\mu$m step, the No FI case takes 30.5 ms and 29.5 ms to settle in the first and eighth steps while the FI case settles within 7 ms and 6.7 ms, respectively. During point-to-point motions with the 50 $\mu$m step size, the stage without FI takes 39.5 ms and 56.1 ms to settle in the first and eighth steps, respectively, while the stage with FI takes 13.5 ms and 13.3 ms to settle in the first and eight steps. This shows that the undesirable effects of the bearing motion during settling is effectively attenuated when the DOB is implemented in the control scheme. Although the bearing still moves significantly during settling for the 50 $\mu$m case, the DOB can effectively

estimate and cancel out the associated disturbance force. This significantly reduces the workload of the PID controller such that it can quickly move the friction-isolated NP stage to the target position.

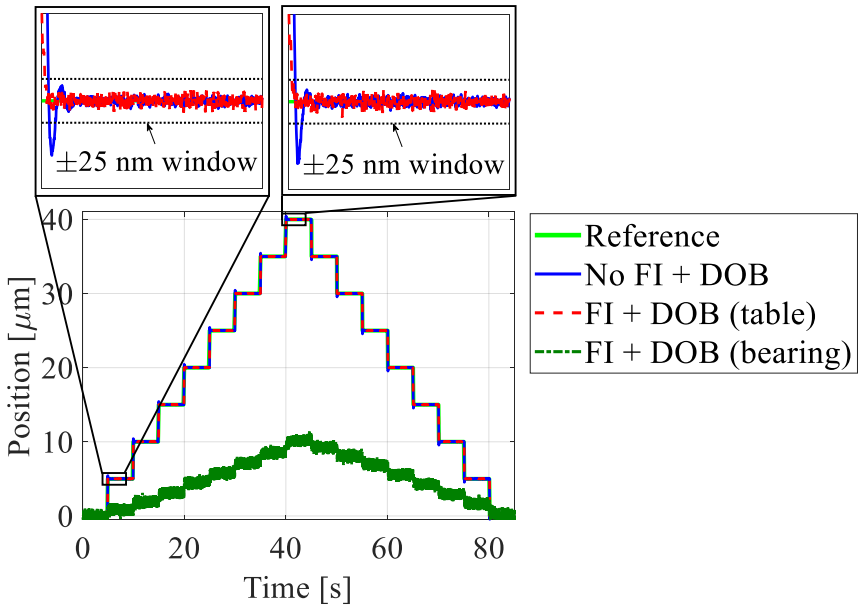


Figure C.13 Typical setting performance of the No FI case and FI case with DOB into the ±25 nm window during 5 $\mu$m point-to-point motion. The bearing motion of the FI case is also plotted in addition to its table motion. Note that the bearing and table motions of the No FI case are identical.

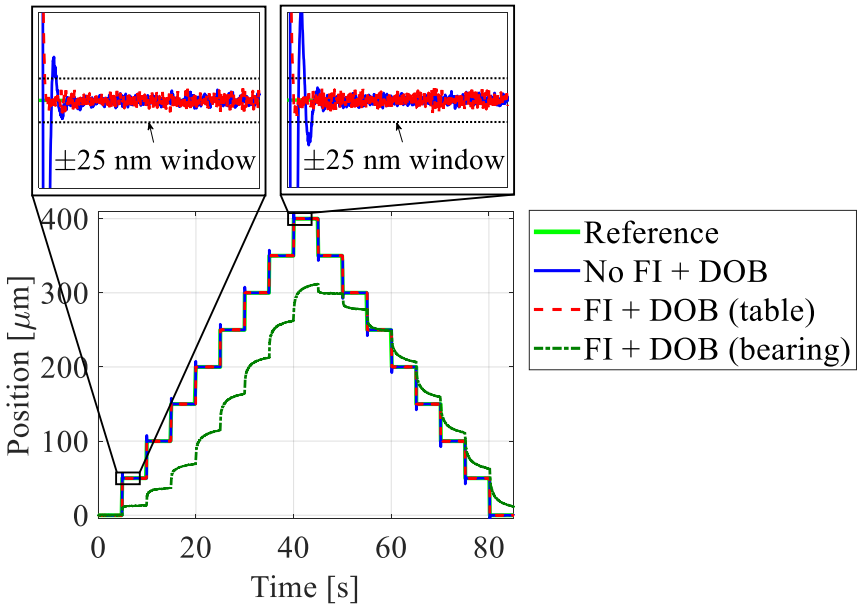


Figure C.14 Typical setting performance of the No FI case and FI case with DOB into the ±25 nm window during 50 $\mu$m point-to-point motion. The bearing motion of the FI case is also plotted in addition to its table motion. Note that the bearing and table motions of the No FI case are identical.

## C.3 Summary

Point-to-point positioning tests with step sizes from 50 nm to 5 mm are conducted on the stage with and without friction isolator (FI). The FI case achieves much faster and robust settling than the No FI case for most step motions tested. However, during point-to-point motions with the 50 $\mu$m step size, it settles much slower than the conventional mechanical-bearing-guided nanopositioning (NP) stage with significantly increased variations in settling time. By measuring both the table and bearing displacements, it is observed that the sluggish settling behavior of the friction-isolated NP stage is due to the bearing motion during settling, which poses significant difficulties for the PID controller to compensate the resulting disturbance force.

An inverse-model-based disturbance observer (DOB) combined with the PID controller is proposed as a possible approach to address the effects of bearing motion on the settling performance of the stage with FI. It is experimentally demonstrated that with the addition of DOB to the PID controller, the bandwidth and robustness of the FI case relative to the No FI case is further improved. Moreover, it is able to mitigate the undesirable effects of the bearing motion

during point-to-point motions with the 50 $\mu$m step size, because of the ability of the DOB to observe and cancel out the disturbances emanating from the motion of the bearing. As a result, the stage with FI outperforms the stage without it (also controlled using a PID controller plus DOB) and settles within the desired ±25 nm window in less than 20 ms for all the step sizes tested.

# Appendix D

## Rotary Friction Isolator for High Precision Roll-to-roll Manufacturing

A rotary system, which utilizes the friction isolator (FI) proposed in Chapter 4, for high precision roll-to-roll manufacturing is discussed. The problem of friction in continuous roll-to-roll manufacturing is illustrated in Section D.1. In Section D.2, the concept of the friction-isolated rotary system is proposed. The design of a rotary FI that minimizes the adverse effects of bearing friction without overly sacrificing high rigidity of the machine is discussed in Section D.3. In Section D.4, numerical simulation demonstrates that the rotary system with FI achieves significantly improved attenuation of frictional disturbance, compared to the case without it.

### D.1 Background and motivation

Roll-to-roll manufacturing processes, that pattern and coat electronic functional materials on plastic films, are considered as low cost and high throughput technologies to manufacture flexible and large-area thin film electronics, such as organic photovoltaics, thin film transistors, light-emitting diodes and fuel cells [146]. In a typical roll-to-roll manufacturing system (see Figure D.1), processes are carried out by transporting the plastic film continuously from unwinder to winder. For this purpose, the processing roller is generally controlled to move at constant velocity (CV) while tension of the plastic film is controlled by the unwinder and winder. Therefore, tracking accuracy of the processing roller during CV motion is crucial to the performance of roll-to-roll system because the resulting position error directly affects the quality of the manufactured products. For example, the directional coating uniformity and patterning error of the machine will be degraded by the velocity ripple and position error of the processing roller during coating processes [147] and patterning processes [148], respectively.

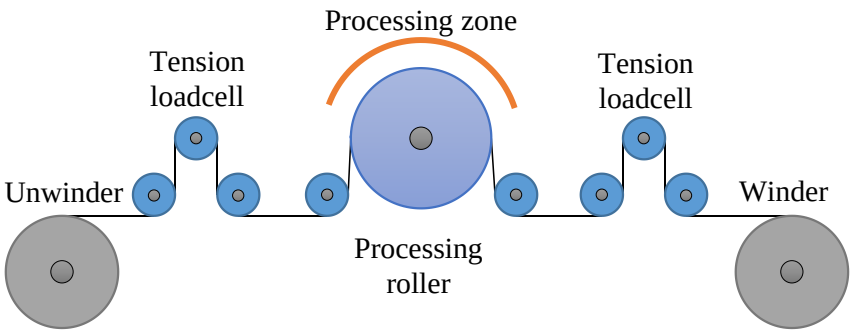


Figure D.1 Schematic of a typical roll-to-roll manufacturing system.

Friction forces due to the guiding ball bearings are major disturbances that affect the precision of the processing roller [59]. During CV motions, variation of friction occurs as the balls roll inside the bearing groove [59], severely hampering the tracking accuracy of the system. Figure D.2(a) shows the typical motion errors of the processing roller while it is stationary (i.e., in-position) and moving at a CV of 12 rpm. The feedback controller is tuned to have a closed loop bandwidth of 100 Hz which is much higher than the dominant frequency of the rotary motion (0.2 Hz). As shown in the frequency spectra of the position error signals (see Figure D.2(b)), the dominant peaks at low frequency region (< 10 Hz) are caused by the force ripple of the motor [149], which can be compensated by repetitive control; the remaining broad band frequency components (10 – 100 Hz) with large amplitudes are mainly due to frictional disturbance from the rotary ball bearings.

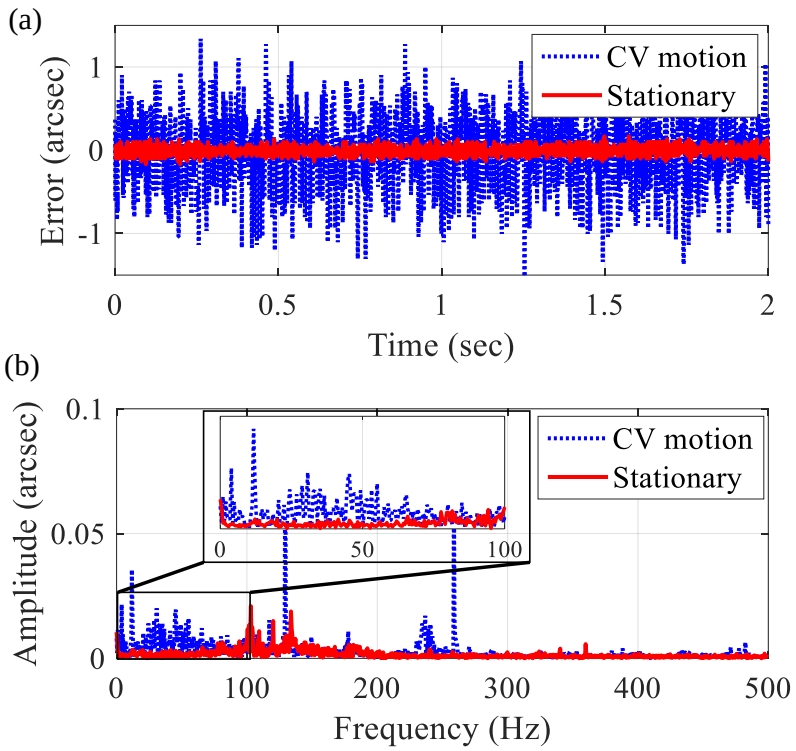


Figure D.2 (a) Typical position errors of the rotary system guided by ball bearings, and (b) frequency spectra of the position error signals.

## D.2 Friction-isolated rotary system

Figure D.3 shows the schematic of the proposed rotary system with friction isolator (FI). The processing roller, of inertia $I_p$ is connected to the rotary bearings of inertia $I_a$ using two FIs with rotational stiffness $k_{fi}$ and damping $c_{fi}$. The inner rings of the ball bearings are connected to the FIs and the outer rings are fixed to the ground. The viscous friction coefficient between sliding surfaces of the bearings is denoted by $c_f$. $T_a$, $T_p$ and $T_f$ are respectively the driving torque of the motor, process-induced disturbance torque and frictional disturbance torque of the ball bearing.

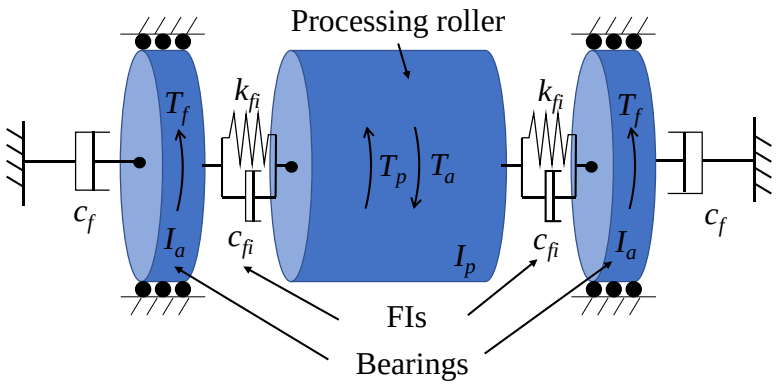


Figure D.3 Schematic of a rotary system equipped with FIs.

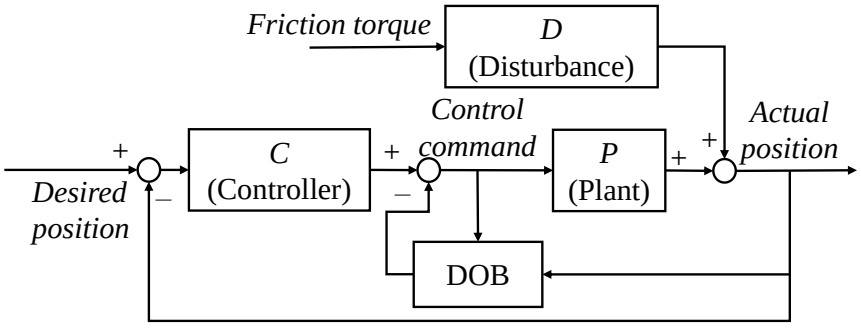


Figure D.4 Control block diagram with feedback controller and DOB.

An industry-standard PID controller is used to control the motion of the processing roller; it is tuned to 100 Hz closed loop bandwidth. Since the feedback controller has limited ability in rejecting disturbances, an inverse-model-based disturbance observer (DOB) [145] is implemented to further attenuate the low frequency disturbances due to frictional variations as shown in Figure D.4; it is tuned to 80 Hz bandwidth. The effectiveness of FI can be shown by calculating the open loop disturbance transfer function, *D*, as

$$D_{NoFI}(s) = 2G_{p,NoFI}(s);\ D_{FI}(s) = G_{p,FI}(s)\frac{2(c_{fi}s + k_{fi})}{I_a s^2 + (c_{fi} + c_f)s + k_{fi}} \tag{D.1}$$

where *s* is the Laplace variable, $G_p$ is the plant dynamics and subscripts *NoFI* and *FI* denote the cases without and with FI. They are given by

$$G_{p,NoFI}(s)=\frac{1}{\left(I_p+2I_a\right)s^2+2c_f s};$$
$$G_{p,FI}(s)=\frac{I_a s^2+\left(c_{fi}+c_f\right)s+k_{fi}}{I_p I_a s^4+\left[c_{fi}\left(I_p+\ 2I_a\right)+c_f I_p\right]s^3+\left[k_{fi}\left(I_p+2I_a\right)+2c_{fi}c_f\right]s^2+2k_{fi}c_f s} \quad \text{(D.2)}$$

Note that in the No FI case, the processing roller is rigidly connected to the bearings. It is clearly shown that the undesirable effects of frictional disturbances are low pass filtered by the dynamics of FI. To further illustrate the effects of stiffness and damping parameters on the performance of FI, the closed loop transfer function from frictional disturbance to roller position (including the DOB) is obtained as [145]

$$G_d(s)=\frac{D(s)G_n(s)\left(1-Q(s)\right)}{Q(s)\left(G_p(s)-G_n(s)\right)\ +G_n(s)\left(1\ +C(s)G_p(s)\right)} \quad \text{(D.3)}$$

where $C$ is the feedback (PID) controller, $Q$ is a low pass filter to guarantee stability and $G_n$ is the nominal plant model that describes the low frequency characteristics of the conventional rotary system (dominated by rigid body dynamics)

$$C(s)=K_p+\frac{K_d s}{T_f s+1}+\frac{K_i}{s};\ Q(s)=\ \frac{\left(2\pi f_Q\right)^2}{\left(s+2\pi f_Q\right)^2};G_n(s)=\ \frac{1}{\left(I_p+2I_a\right)s^2+2c_f s} \quad \text{(D.4)}$$

Figure D.5 compares the magnitudes of $G_{d,NoFI}$ and $G_{d,FI}$ using different stiffness $k_{fi}$ for FI. Note that a modal damping of 0.1% is introduced to account for the damping of FI (i.e., $c_{fi}$) and the remaining parameters are summarized in Table D.1. Observe that the frictional disturbance in the high frequency region is effectively suppressed by the FI, thanks to its low pass filtering effects. The benefits of FI become more dominant when the stiffness is reduced since the magnitude of $G_{d,FI}$ quickly rolls off after the resonance peak. In other words, a lower stiffness FI leads to better suppression of frictional disturbance.

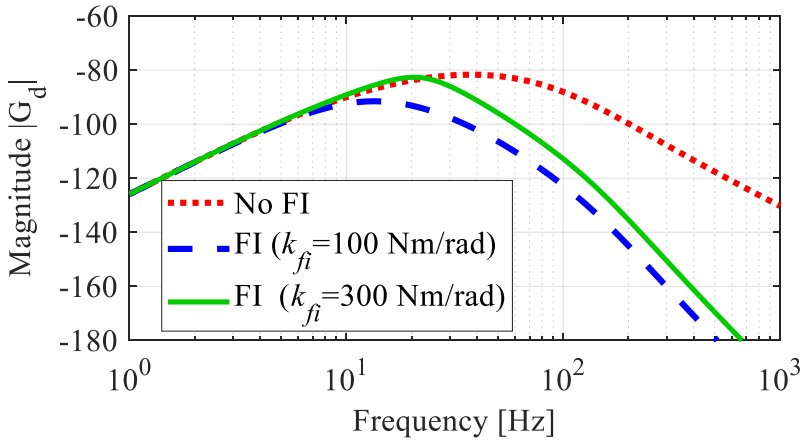


Figure D.5 Magnitudes of $G_{d,NoFI}$ and $G_{d,FI}$ with different stiffness values for FI. Note that $c_f$ = 2 Nms/rad is used.

Table D.1 Parameters of the rotary system.

| Parameter | Value |
|---|---|
| $I_p$ | 0.15 kgm$^2$ |
| $I_a$ | 0.015 kgm$^2$ |
| $K_p$ | 1.54 × 10$^4$ N$_{rms}$/rad |
| $K_d$ | 81.62 N$_{rms}$s/rad |
| $K_i$ | 6.16 × 10$^5$ N$_{rms}$/rads |
| $T_f$ | 0.0005884 s |
| $f_Q$ | 80 Hz |

Figure D.6 shows the effects of viscous friction on the performance of FI. Since the FI design often has limited damping, the resonance peak has very large amplitude if the frictional damping is small. This poses significant challenge since the dominant resonance can be easily excited (e.g., by frictional variation), generating large position errors. Therefore, a high viscous damping coefficient of the bearing is needed in order to attenuate the resonance peak and achieve the desired performance of FI.

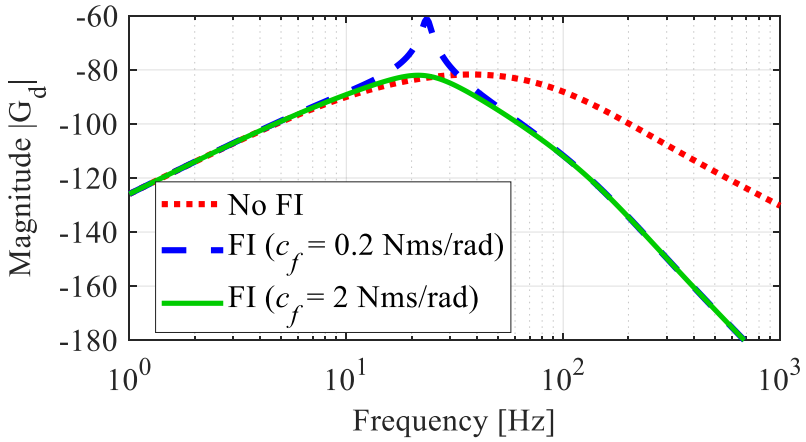


Figure D.6 Effects of viscous damping coefficient $c_f$ on the performance of FI. Note that $k_{fi}$ = 300 Nm/rad is used.

## D.3 Design of a rotary system with friction isolator

Figure D.7 shows the CAD model of the proposed friction-isolated rotary system. The processing roller is guided by two angular contact ball bearings (NSK, 7013A). It is driven by a direct drive motor (Kollmorgen, C042A). To augment the bearing friction, $c_f$, an eddy current damper is implemented at the interface between the ball bearings and the ground.

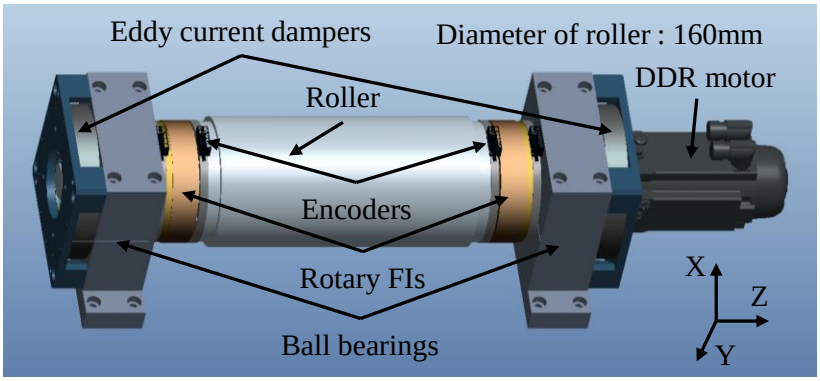


(a)

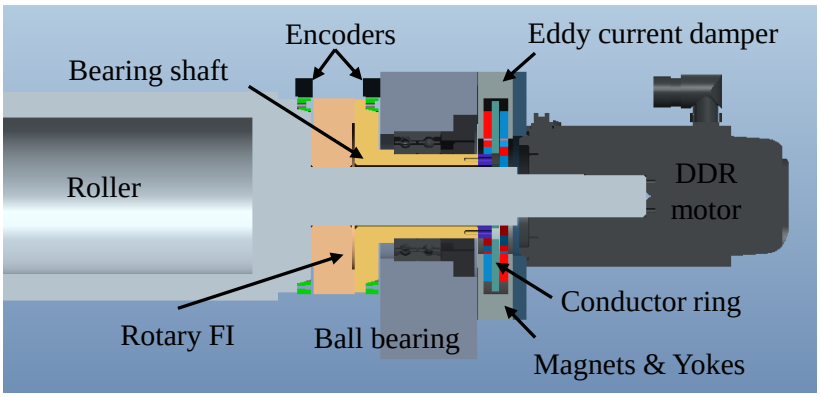


(b)

Figure D.7 (a) CAD model, and (b) cross-section view of the friction-isolated rotary system.

The FIs are used to connect the processing roller to the rotary bearings. Figure D.8 shows the schematics of the proposed FI design. Symmetric cartwheel flexure (SCF) mechanism [150][151] with four leaf springs are adopted in the design; the center platform of the flexure is connected to the ball bearing and the outer platform is connected to the processing roller. To achieve the desired attenuation of frictional disturbance, the FI should have minimal stiffness $k_{fi}$ in the motion direction; in the meantime, the FI must maintain high stiffness in the off-motion directions (e.g., radial directions), so as not to overly sacrifice the rigidity of the ball bearing. Therefore, parameters of the SCF mechanism, specifically, leaf length $l$, leaf thickness $t$, leaf width $b$, inner platform radius $r_i$ and viscous damping coefficient $c_f$, are optimized to maximize the stiffness ratios between off-motion directions and motion direction while satisfying other design constraints (e.g., maximum stress and dimension).

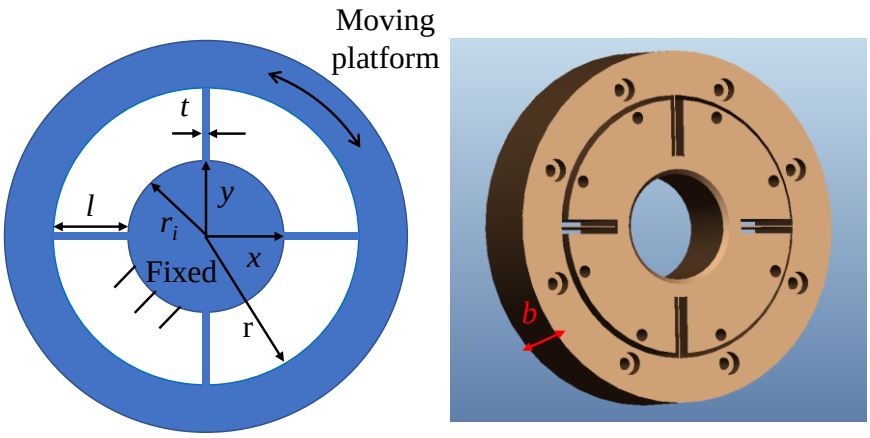


Figure D.8 (a) Schematic, and (b) CAD drawing of symmetric cartwheel flexure (SCF) design [150].

To achieve the desired viscous damping, a rotary eddy current mechanism is designed. The permanent magnets of the proposed eddy current damper are arranged in circumferential direction, which is similar to that of a doubled-sided linear motor. The rotating disc is placed between the upper and lower magnetic arrays and viscous damping torque is achieved due to the interaction of eddy current and magnetic field. Figure D.9 shows an example of the simulated eddy current density and magnetic field (using ANSYS®) when the disc is rotating at 1 rpm. The resulting damping torque can be calculated by volume integration of the rotating disc as

$$T_{damp} = \int r_v \times \left(J \times B\right) d\tau \tag{D.5}$$

where $r_v$ is the radial location of the infinitesimal element used in volume integration, $J$ is the current density, $B$ is the magnetic field, and $d\tau$ is the volume of the infinitesimal element. With an outer radius of 95 mm and a thickness of 27 mm, the desired viscous damping coefficient of 1.2 Nms/rad is achieved.

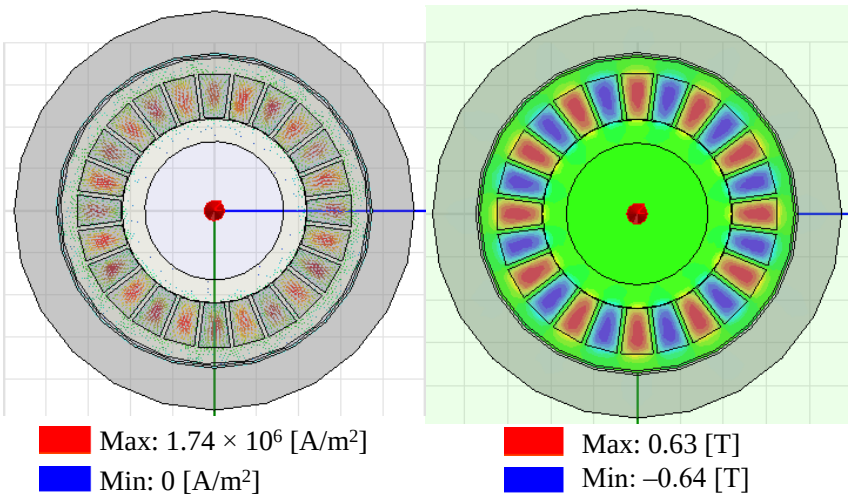


Figure D.9 Simulated eddy current density (left) and magnetic field (right) using ANSYS®.

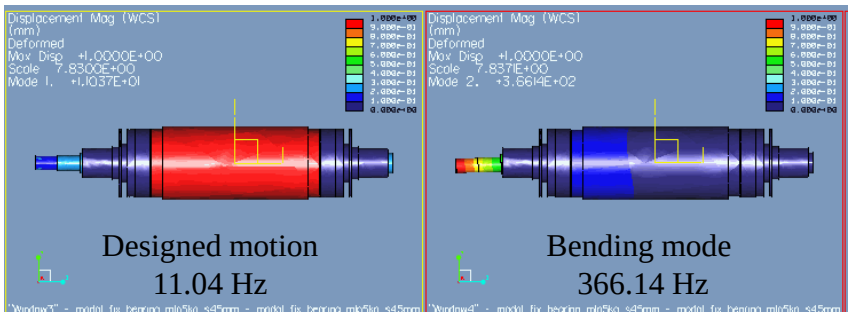


Figure D.10 Simulated resonance modes of the designed rotary system with FI.

Figure D.10 shows the simulated resonance modes of the rotary system assembly with FI. Note that the lowest uncontrollable mode is 366.14 Hz which is much higher than our desired closed loop bandwidth, i.e., 100 Hz. Figure D.11 shows the manufactured friction-isolated rotary system. The direct drive motor is powered using a PWM amplifier (Kollmorgen, AKD-B00606). The angular position of the processing roller is measured using a ring encoder (Renishaw, Encoder head – RGH20Y, Ring scale – PESR20USA150) that is mounted on the side surface of the roller; it has an angular resolution of 1.33 $\mu$rad. The feedback controller is implemented using a real-time control board (dSPACE, DS1005).

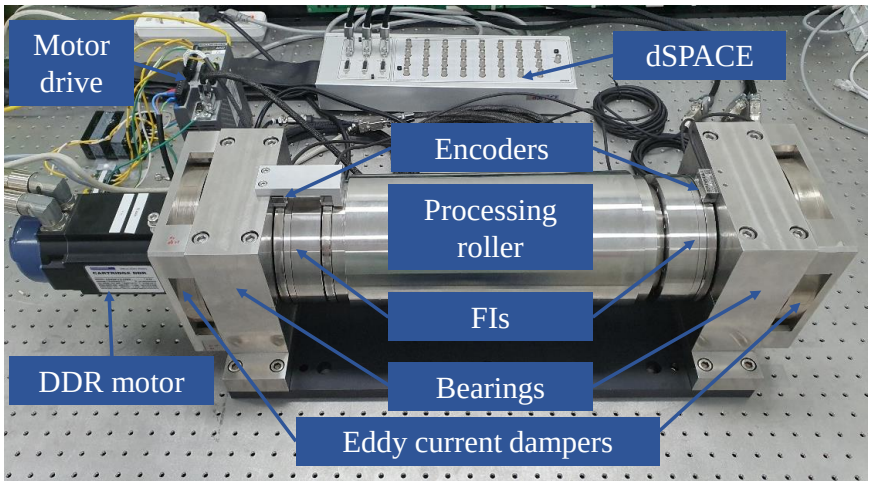


Figure D.11 In-house built prototype rotary system equipped with the designed FIs.

## D.4 Numerical Simulation

The performance of the proposed rotary system with FI is compared with the conventional system (i.e., No FI) in simulation. Table D.2 summarizes the parameters obtained from the designed SCF; note that viscous coefficient (i.e., $c_f$) of the case without eddy current damper is contributed by the viscous friction from the ball bearing. Figure D.12 shows the simulated tracking performance of the designed rotary system when the processing roller is moving at 10 rpm CV. To replicate the practical scenario when friction variations occur, normally distributed disturbance force with 0.15 Nm standard deviation (i.e., RMS value) is introduced in the simulation. The case without FI has an RMS error of 1.41 $\mu$rad during the CV motion. In the absence of the eddy current damper, the system with FI suffers from significant vibrations around the resonance frequency, leading to an increased RMS error to 2.62 $\mu$rad. Using the FI with the designed eddy current damper, the system achieves 36% reduction of the RMS error (0.91 $\mu$rad), when compared to the No FI case.

Table D.2 Parameters used in simulations.

| Parameters | Value |
|---|---|
| $I_p$ | 0.1401 kgm$^2$ |
| $I_a$ | 0.01491 kgm$^2$ |
| $k_{fi}$ | 324.85 Nm/rad |
| $c_{fi}$ | 0 Nms/rad |
| $c_f$ (w/o damper) | 0.2 Nms/rad |
| $c_f$ (w/ damper) | 1.4 Nms/rad |

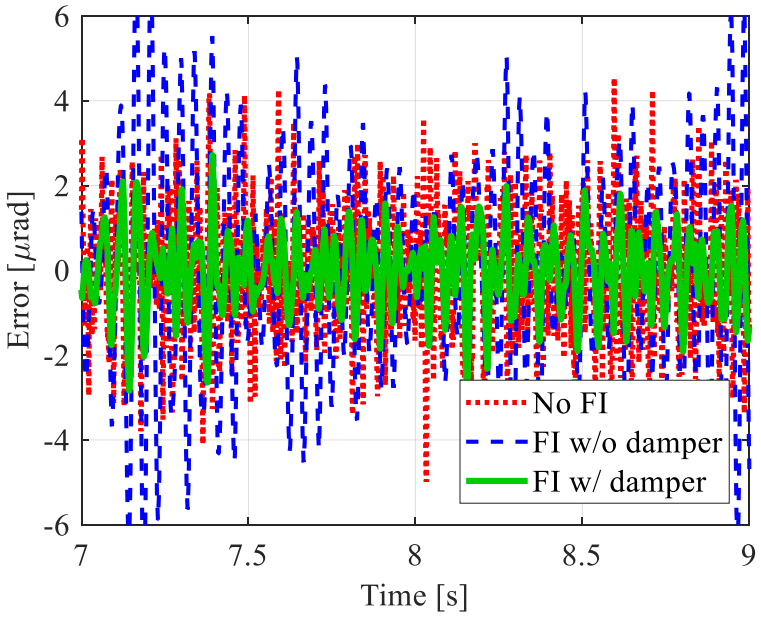


Figure D.12 Simulated tracking error of the proposed rotary system during 10 rpm CV motion.

## D.5 Summary

A novel rotary system for achieving high precision continuous roll-to-roll manufacturing is presented. The proposed system integrates the friction isolator (FI) from Chapter 4 to mitigate the undesirable effects of friction on the tracking accuracy of the processing roller. It is demonstrated through frequency domain analysis that FI improves the disturbance rejection ability of the system by low pass filtering the frictional disturbance from the supporting bearings. A rotary FI prototype is then designed with symmetric cartwheel flexure mechanism; its parameters are

optimized to achieve lowest stiffness in the motion direction (for better disturbance suppression) while maintaining high stiffness in off-motion directions so as not to unduly sacrifice the rigidity of the machine. An eddy current damper is designed to provide additional viscous damping that is critical for attenuating the resonance mode due to FI. It is demonstrated in simulation that the proposed FI achieves 36% reductions in RMS tracking error during CV test of 10 rpm, compared to the case without it. Ongoing work focuses on experimentally validating the performance of the proposed friction-isolated rotary system.

## BIBLIOGRAPHY


[1] National Nanotechnology Initiative. *What is nanotechnology*. (https://www.nano.gov/nanotech-101/what/definition; accessed on Dec. 17th, 2019)

[2] McWilliams A. *The maturing nanotechnology market: products and application*. BCC Research. 2016.

[3] Sargent JF. *Nanotechnology and US competitiveness: issues and options*. Library of Congress Washington DC Congressional Research Service. 2008.

[4] Fleming AJ, Leang KK. *Design, modeling and control of nanopositioning systems*. Switzerland: Springer International Publishing. 2014.

[5] McWilliams A. *Nanodevices and nanomachines: the global market*. BCC Research. 2018.

[6] Chou PB, Rao AR, Sturzenbecker MC, Wu FY, Brecher VH. *Automatic defect classification for semiconductor manufacturing.* Machine Vision and Applications. 1997; 9(4):201-214.

[7] Kim WJ, Trumper DL. *High-precision magnetic levitation stage for photolithography*. Precision Engineering. 1998; 22:66-77.

[8] Stokowski S, Vaez-Iravani M. *Wafer inspection technology challenges for ULSI manufacturing*. AIP Conference Proceedings. 1998; 449(1):405-415.

[9] Chen L, Rong W, Sun L, Xie H. *Micromanipulation robot for automatic fiber alignm*ent. IEEE International Conference Mechatronics and Automation. 2005; 4:1756-1759.

[10] del Campo A, Greiner C, Álvarez I, Arzt E. *Patterned surfaces with pillars with controlled 3D tip geometry mimicking bioattachment devices*. Advanced Materials. 2007; 19(15):1973-1977.

[11] Altintas Y, Verl A, Brecher C, Uriarte L, Pritschow G. *Machine tool feed drives*. CIRP Annals-Manufacturing Technology. 2011; 60(2):779-796.

[12] Schmidt RM. *Ultra-precision engineering in lithographic exposure equipment for the semiconductor industry*. Philosophical Transactions of the Royal Society A: Mathematical, Physical and Engineering Sciences. 2012; 370(1973):3950-3972.

[13] Maeda Y, Iwasaki M. *Initial friction compensation using rheology-based rolling friction model in fast and precise positioning*. IEEE Transactions on Industrial Electronics. 2012; 60(9):3865-3876.

[14] Bucci BA. *A practical method for friction compensation in rapid point-to-point motion*. Doctoral Dissertation, University of Pittsburgh. 2011.

[15] Hitachi. *Wafer defect inspection system*. (https://www.hitachi-hightech.com/global/products/device/semiconductor/inspection.html; accessed on Dec 17th, 2019)

[16] ISO. *Test code for machine tools – Part 1: geometric accuracy of machines operating under no-load or quasi-static conditions (ISO 230-1:2012)*. (https://www.iso.org/standard/46449.html; accessed on Nov. 24th, 2019)

[17] Yong YK, Aphale SS, Moheimani SR. *Design, identification, and control of a flexure-based xy stage for fast nanoscale positioning*. IEEE Transactions on Nanotechnology. 2008; 8(1):46-54.

[18] Nikon. *Semiconductor lithography systems*. (https://www.nikon.com/about/technology/product/semiconductor/index.htm; accessed on Nov. 21st, 2019)

[19] Schmidt RM, Schitter G, Rankers A, van Eijk J. *The design of high performance mechatronics: high-tech functionality by multidisciplinary system integration*. IOS Press; 2014.

[20] Butler H. *Position control in lithographic equipment*. IEEE Control Systems Magazine. 2011; 31(5):28-47.

[21] Liu X, Tong J, Sun Y. *A millimeter-sized nanomanipulator with sub-nanometer positioning resolution and large force output*. Smart Materials and Structures. 2007; 16(5):1742-1750.

[22] Scientific American. *The next 20 years of microchips: pushing performance boundaries*. (https://www.scientificamerican.com/article/the-next-20-years-of-microchips/; accessed on Nov. 24th, 2019)

[23] Culpepper ML, Anderson G. *Design of a low-cost nano-manipulator which utilizes a monolithic, spatial compliant mechanism*. Precision Engineering. 2004; 28(4):469-482.

[24] Jordan SC. *Recent advances in improving static and dynamic accuracy of nanopositioning systems*. Annual Meeting of American Society for Precision Engineering. 2006.

[25] Parmar GK. *Dynamics and control of flexure-based large range nanopositioning systems*. Doctoral Thesis, University of Michigan. 2014.

[26] Physik Instrumente (PI). *Piezo flexure nanopositioning stages: frequently asked questions*. (https://www.pi-usa.us/en/tech-blog/piezo-flexure-nanopositioning-stages-frequently-asked-questions/; accessed on Nov 24th, 2019)

[27] Awtar S, Parmar G. *Design of a large range xy nanopositioning system*. Journal of Mechanisms and Robotics. 2013; 5(2):021008.

[28] Kenton BJ, Leang KK. *Design, characterization, and control of a monolithic three-axis high-bandwidth nanopositioning stage*. Proceedings of the 2010 American Control Conference. 2010; 4949-4956.

[29] Hiemstra DB, Parmar G, Awtar S. *Performance tradeoffs posed by moving magnet actuators in flexure-based nanopositioning*. IEEE/ASME Transactions on Mechatronics. 2012; 19(1):201-212.

[30] Physik Instrumente (PI). *PIMag® 6-D magnetic levitation at six levels of freedoms*. (https://www.physikinstrumente.com/en/technology/electromagnetic-drives/pimag-6d-magnetic-levitation/; accessed on Nov 24th, 2019)

[31] Verma S, Kim WJ, Gu J. *Six-axis nanopositioning device with precision magnetic levitation technology*. IEEE/ASME Transactions on Mechatronics. 2004; 9(2):384-391.

[32] Zhang Z, Menq CH. *Six-axis magnetic levitation and motion control*. IEEE Transactions on Robotics. 2007; 23(2):196-205.

[33] Schaeffler. *Linear guides with hydrostatic compact guide*. (https://www.schaeffler.de/content.schaeffler.de/en/products-and-solutions/industrial/x_life/index.jsp; accessed on Nov 24th, 2019)

[34] Pan T, Wang W. *From cleanroom to desktop: emerging micro-nanofabrication technology for biomedical applications*. Annals of Biomedical Engineering. 2011; 39(2):600-620.

[35] Cabrini S, Kawata S (Editors). *Nanofabrication handbook*. CRC Press; 2012.

[36] Specialty Components. *Air bearing fundamentals*. (https://www.specialtycomponents.com/Resources/Technical-Articles/Air-Bearing-Fundamentals/; accessed on Nov 24th, 2019)

[37] Aerotech Inc. *ABL2000 air bearing, direct-drive linear stage*. (https://www.aerotech.com/product-catalog/stages/linear-stage/abl2000.aspx?p=%2fproduct-catalog%2fstages.aspx%3f; accessed on Nov 24th, 2019)

[38] Sitti M. *Survey of nanomanipulation systems*. Proceedings of the 1st IEEE Conference on Nanotechnology. 2001; 75-80.

[39] Satterley CJ, Perdigão LM, Saywell A, Magnano G, Rienzo A, Mayor LC, Dhanak VR, Beton PH, O'Shea JN. *Electrospray deposition of fullerenes in ultra-high vacuum: in situ scanning tunneling microscopy and photoemission spectroscopy*. Nanotechnology. 2007; 18(45):455304.

[40] Utke I, Hoffmann P, Melngailis J. *Gas-assisted focused electron beam and ion beam processing and fabrication*. Journal of Vacuum Science & Technology B: Microelectronics and Nanometer Structures Processing, Measurement, and Phenomena. 2008; 26(4):1197-1276.

[41] Aerotech Inc. *Industries & applications: vacuum*. (https://www.aerotech.com/industries-and-applications/vacuum.aspx; accessed on Nov 24th, 2019)

[42] Firgelli Automations. *FA-SGR-35 series – heavy duty linear bearing slide rails*. (https://www.firgelliauto.com/products/linear-bearings?variant=885892695&currency=USD&gclid=CjwKCAiA8ejuBRAaEiwAn-iJ3nz5rljn8I-myCXTQGYlyJnvX4eaomaqhxuNlQ69Z1jYiLPLfC6-OhoCuhYQAvD_BwE; accessed on Nov 24th, 2019)

[43] THK. *LM guide (linear motion guide)*. (https://www.thk.com/?q=in/node/3029; accessed on Nov 24th, 2019)

[44] Nippon Bearing. *Cross roller linear slide guides*. (https://www.nbcorporation.com/shop/slide-way-gonio-way/crossed-roller-slide-ways/; accessed on Nov 24th, 2019)

[45] Aerotech Inc. *PlanarDLA two axis mechanical-bearing direct-drive stage with aperture*. (https://www.aerotech.com/product-catalog/stages/linear-x-y-stages/planardla.aspx?p=%2fproduct-catalog%2fstages.aspx%3fpage%3d3; accessed on Nov 24th, 2019)

[46] Dahl PR. *A solid friction model*. Aerospace Corp El Segundo Ca. 1968.

[47] Dahl PR. *Solid friction damping of spacecraft oscillations*. Guidance and Control Conference. 1975; 1104.

[48] Futami S, Furutani A, Yoshida S. *Nanometer positioning and its micro-dynamics*. Nanotechnology. 1990; 1(1):31-37.

[49] Armstrong-Hélouvry B, Dupont P, De Wit CC. *A survey of models, analysis tools and compensation methods for the control of machines with friction*. Automatica. 1994; 30(7):1083-1138.

[50] Otsuka J, Masuda T. *The influence of nonlinear spring behavior of rolling elements on ultraprecision positioning control systems*. Nanotechnology. 1998; 9(2):85-92.

[51] Al-Bender F, Symens W. *Characterization of frictional hysteresis in ball-bearing guideways*. Wear. 2005; 258(11-12):1630-1642.

[52] Al-Bender F, Swevers J. *Characterization of friction force dynamics*. IEEE Control Systems Magazine. 2008; 28(6):64-81.

[53] Maeda Y, Iwasaki M. *Rolling friction model-based analyses and compensation for slow settling response in precise positioning*. IEEE Transactions on Industrial Electronics. 2012; 60(12):5841-5853.

[54] Bucci BA, Vipperman JS, Cole DG, Ludwick SJ. *Evaluation of a servo settling algorithm*. Precision Engineering. 2013; 37(1):10-22.

[55] Yoon JY, Trumper DL. *Friction modeling, identification, and compensation based on friction hysteresis and Dahl resonance*. Mechatronics. 2014; 24(6):734-741.

[56] Yoon JY, Trumper DL. *Friction microdynamics in the time and frequency domains: tutorial on frictional hysteresis and resonance in precision motion systems*. Precision Engineering. 2019; 55:101-109.

[57] Erkorkmaz K, Altintas Y. *High speed CNC system design. part II: modeling and identification of feed drives*. International Journal of Machine Tools and Manufacture. 2001; 41(10):1487-1509.

[58] Yeung CH. *A three-axis virtual computer numerical-controlled (CNC) system*. Master's Thesis, University of British Columbia. 2004.

[59] Fujita T, Matsubara A, Yamazaki K. *Experimental characterization of disturbance force in a linear drive system with high-precision rolling guideways*. International Journal of Machine Tools and Manufacture. 2011; 51(2):104-111.

[60] Helmick D, Messner W. *Describing function analysis of dahl model friction*. Proceedings of the 2009 American Control Conference. 2009; 0:814–819.

[61] Bucci BA, Cole DG, Ludwick SJ, Vipperman JS. *Nonlinear control algorithm for improving settling time in systems with friction*. IEEE Transactions on Control Systems Technology. 2012; 21(4):1365-1373.

[62] Chang SB, Wu SH, Hu YC. *Submicrometer overshoot control of rapid and precise positioning*. Precision Engineering. 1997; 20(3):161-170.

[63] Lin TY, Pan YC, Hsieh C. *Precision-limit positioning of direct drive systems with the existence of friction*. Control Engineering Practice. 2003; 11(3):233-244.

[64] Sato K, Nakamoto K, Shimokohbe A. *Practical control of precision positioning mechanism with friction*. Precision Engineering. 2004; 28(4):426-434.

[65] Ruderman M, Iwasaki M. *Analysis of linear feedback position control in presence of presliding friction*. IEEJ Journal of Industry Applications. 2016; 5(2):61-68.

[66] Jamaludin Z, Van Brussel H, Pipeleers G, Swevers J. *Accurate motion control of xy high-speed linear drives using friction model feedforward and cutting forces estimation*. CIRP Annals-Manufacturing Technology. 2008; 57(1):403-406.

[67] Fukada S, Fang B, Shigeno A. *Experimental analysis and simulation of nonlinear microscopic behavior of ball screw mechanism for ultra-precision positioning*. Precision Engineering. 2011; 35(4):650-668.

[68] Ruderman M. *Tracking control of motor drives using feedforward friction observer*. IEEE Transactions on Industrial Electronics. 2013; 61(7):3727-3735.

[69] Miura T, Matsubara A, Kono D, Otaka K, Hoshide K. *Design of high-precision ball screw based on small-ball concept*. Precision Engineering. 2017; 47:452-458.

[70] THK. *Caged ball LM guide*. (https://tech.thk.com/upload/catalog_claim/pdf/235E_SHS.pdf; accessed on Nov 25th, 2019)

[71] Altintas Y, Erkorkmaz K, Zhu WH. *Sliding mode controller design for high speed feed drives*. CIRP Annals-Manufacturing Technology. 2000; 49(1):265-270.

[72] Xi XC, Poo AN, Hong GS. *Tracking error-based static friction compensation for a bi-axial CNC machine*. Precision Engineering. 2010; 34(3):480-488.

[73] Matsubara A, Nagaoka K, Fujita T. *Model-reference feedforward controller design for high-accuracy contouring control of machine tool axes*. CIRP Annals-Manufacturing Technology. 2011; 60(1):415-418.

[74] Itagaki H, Tsutsumi M. *Control system design of a linear motor feed drive system using virtual friction*. Precision Engineering. 2014; 38(2):237-248.

[75] Jamaludin Z, Van Brussel H, Swevers J. *Friction compensation of an xy feed table using friction-model-based feedforward and an inverse-model-based disturbance observer*. IEEE Transactions on Industrial Electronics. 2009; 56(10):3848-3853.

[76] Swevers J, Al-Bender F, Ganseman CG, Projogo T. *An integrated friction model structure with improved presliding behavior for accurate friction compensation*. IEEE Transactions on Automatic Control. 2000; 45(4):675-686.

[77] Reuss M, Dadalau A, Verl A. *Friction variances of linear machine tool axes*. Procedia CIRP. 2012; 4:115-119.

[78] Miura T, Matsubara A, Yamaji I, Hoshide K. *Measurement and analysis of friction fluctuations in linear guideways*. CIRP Annals-Manufacturing Technology. 2018; 67(1):393-396.

[79] Altpeter F, Grunenberg M, Myszkorowski P, Longchamp R. *Auto-tuning of feedforward friction compensation based on the gradient method*. Proceedings of the 2000 American Control Conference. 2000; 4:2600-2604.

[80] Tan KK, Huang SN, Lee TH. *Robust adaptive numerical compensation for friction and force ripple in permanent-magnet linear motors*. IEEE Transactions on Magnetics. 2002; 38(1):221-228.

[81] Dumanli A, Sencer B. *Pre-compensation of servo tracking errors through data-based reference trajectory modification*. CIRP Annals-Manufacturing Technology. 2019; 68(1):397-400.

[82] Olsson H, Åström KJ, De Wit CC, Gäfvert M, Lischinsky P. *Friction models and friction compensation*. European Journal of Control. 1998; 4(3):176-195.

[83] Young KK, Kokotovic P, Utkin V. *A singular perturbation analysis of high-gain feedback systems. IEEE Transactions on Automatic Control*. 1977; 22(6):931-938.

[84] Rice JR, Ruina AL. *Stability of steady frictional slipping*. Journal of Applied Mechanics. 1983; 50(2):343-349.

[85] Armstrong-Hélouvry B. *Stick slip and control in low-speed motion*. IEEE Transactions on Automatic Control. 1993; 38(10):1483-1496.

[86] Brandenburg G, Schafer U. *Influence and compensation of Coulomb friction in industrial pointing and tracking systems*. Conference Record of the 1991 IEEE Industry Applications Society Annual Meeting. 1991; 1407-1413.

[87] Suzuki A, Tomizuka M. *Design and implementation of digital servo controller for high speed machine tools*. Proceedings of the 1991 American Control Conference. 1991; 1246-1251.

[88] Wu CH, Paul RP. *Manipulator compliance based on joint torque control*. 19th IEEE Conference on Decision and Control including the Symposium on Adaptive Processes. 1980; 88-94.

[89] Hashimoto M. *Robot motion control based on joint torque sensing*. Proceedings of 1989 International Conference on Robotics and Automation. 1989; 256-261.

[90] Vischer D, Khatib O. *Performance evaluation of force/torque feedback control methodologies*. 8th CISM-IFtoMM Symposium on Theory and Practice of Robots and Manipulators. 1990; 186-193.

[91] Chong SH, Sato K. *Practical controller design for precision positioning, independent of friction characteristic*. Precision Engineering. 2010; 34(2):286-300.

[92] Cheng G, Hu JG. *An observer-based mode switching control scheme for improved position regulation in servomotors*. IEEE Transactions on Control Systems Technology. 2013; 22(5):1883-1891.

[93] De Wit CC, Olsson H, Astrom KJ, Lischinsky P. *A new model for control of systems with friction*. IEEE Transactions on Automatic Control. 1995; 40(3):419-425.

[94] De Wit CC, Lischinsky P. *Adaptive friction compensation with partially known dynamic friction model*. International Journal of Adaptive Control and Signal Processing. 1997; 11(1):65-80.

[95] Ruderman M, Iwasaki M. *Observer of nonlinear friction dynamics for motion control*. IEEE Transactions on Industrial Electronics. 2015; 62(9):5941-5949.

[96] Maeda Y, Iwasaki M. *Mode switching feedback compensation considering rolling friction characteristics for fast and precise positioning*. IEEE Transactions on Industrial Electronics. 2013; 61(2):1123-1132.

[97] Sariyildiz E, Ohnishi K. *Stability and robustness of disturbance-observer-based motion control systems*. IEEE Transactions on Industrial Electronics. 2014; 62(1):414-422.

[98] Liberzon D, Morse AS. *Basic problems in stability and design of switched systems*. IEEE Control Systems Magazine. 1999; 19(5):59-70.

[99] Schellekens P, Rosielle N, Vermeulen H, Vermeulen M, Wetzels F, Pril W. *Design for precision: current status and trends*. CIRP Annals-Manufacturing Technology. 1998; 47(2):557-586.

[100] Numasato H, Tomizuka M. *Settling control and performance of a dual-actuator system for hard disk drives*. IEEE/ASME Transactions on Mechatronics. 2003; 8(4):431-438.

[101] Choi YM, Kim JJ, Kim J, Gweon DG. *Design and control of a nanoprecision xyθ scanner*. Review of Scientific Instruments. 2008; 79(4):045109.

[102] Zheng J, Fu M. *Nonlinear feedback control of a dual-stage actuator system for reduced settling time*. IEEE Transactions on Control Systems Technology. 2008; 16(4):717-725.

[103] Mori K, Munemoto T, Otsuki H, Yamaguchi Y, Akagi K. *A dual-stage magnetic disk drive actuator using a piezoelectric device for a high track density*. IEEE Transactions on Magnetics. 1991; 27(6):5298–5300.

[104] Takaishi K, Imamura T, Mizoshita Y, Hasegawa S, Ueno T, Yamada T. *Microactuator control for disk drive*. IEEE Transactions on Magnetics. 1996; 32(3):1863–1866.

[105] Evans RB, Griesbach JS, Messner WC. *Piezoelectric microactuator for dual stage control*. IEEE Transactions on Magnetics. 1999; 35(2):977–982.

[106] Elfizy AT, Bone GM, Elbestawi MA. *Design and control of a dual-stage feed drive*. International Journal of Machine Tools and Manufacture. 2005; 45(2):153-165.

[107] Dong W, Tang J, ElDeeb Y. *Design of a linear-motion dual-stage actuation system for precision control*. Smart Materials and Structures. 2009; 18(9):095035.

[108] Fung RF, Hsu YL, Huang MS. *System identification of a dual-stage xy precision positioning table*. Precision Engineering. 2009; 33(1):71-80.

[109] Pahk HJ, Lee DS, Park JH. *Ultra precision positioning system for servo motor-piezo actuator using the dual servo loop and digital filter implementation*. International Journal of Machine Tools and Manufacture. 2001; 41(1):51-63.

[110] Wu JW, Huang KC, Chiang ML, Chen MY, Fu LC. *Modeling and controller design of a precision hybrid scanner for application in large measurement-range atomic force microscopy*. IEEE Transactions on Industrial Electronics. 2013; 61(7):3704-3712.

[111] Lee CW, Kim SW. *An ultraprecision stage for alignment of wafers in advanced microlithography*. Precision Engineering. 1997; 21(2–3):113-122.

[112] Fujita T, Matsubara A, Kono D, Yamaji I. *Dynamic characteristics and dual control of a ball screw drive with integrated piezoelectric actuator*. Precision Engineering. 2010; 34(1):34-42.

[113] Hao G, Kong X. *Novel xy compliant parallel manipulators for large displacement translation with enhanced stiffness*. ASME 2010 International Design Engineering Technical Conferences and Computers and Information in Engineering Conference. 2010; 1037-1047.

[114] Kim KH, Choi YM, Gweon DG, Hong DP, Kim KS, Lee SW, Lee MG. *Design of decoupled dual servo stage with voice coil motor and linear motor for xy long stroke ultra-precision scanning system*. ICMIT 2005: Mechatronics, MEMS, and Smart Materials. 2006; 6040: 60401C

[115] Song Y, Wang J, Yang K, Yin W, Zhu Y. *A dual-stage control system for high-speed, ultra-precise linear motion*. The International Journal of Advanced Manufacturing Technology. 2010; 48(5-8):633-643.

[116] Xu Q. *Design and development of a flexure-based dual-stage nanopositioning system with minimum interference behavior*. IEEE Transactions on Automation Science and Engineering. 2012; 9(3):554-563.

[117] Choi YM, Gweon DG. *A high-precision dual-servo stage using Halbach linear active magnetic bearings*. IEEE/ASME Transactions on Mechatronics. 2010; 16(5):925-931.

[118] Physik Instrumente (PI). *Hybrid nanopositioning technology by PI: long travel linear slides with nanometer precision*. (https://www.pi-usa.us/fileadmin/user_upload/pi_us/files/product_datasheets/PI_Hybrid_Precision_Linear_Stage.pdf; accessed on Nov 25th, 2019)

[119] Engel T, Lechler A, Verl A. *Sliding bearing with adjustable friction properties*. CIRP Annals-Manufacturing Technology. 2016; 65(1):353-356.

[120] Zames G, Shneydor N. *Dither in nonlinear systems*. IEEE Transactions on Automatic Control. 1976; 21(5):660-667.

[121] Thomsen JJ. *Some general effects of strong high-frequency excitation: stiffening, biasing and smoothening*. Journal of Sound and Vibration. 2002; 253(4):807-831.

[122] Chatterjee S, Singha TK, Karmakar SK. *Effect of high-frequency excitation on a class of mechanical systems with dynamic friction*. Journal of Sound and Vibration. 2004; 269(1-2):61-89.

[123] Yoshida Y, Tanaka M. *Position control of a flexible arm using a dither signal*. JSME International Journal. Ser. C, Dynamics, Control, Robotics, Design and Manufacturing. 1993; 36(1):93-99.

[124] Cunefare KA, Graf AJ. *Experimental active control of automotive disc brake rotor squeal using dither*. Journal of Sound and Vibration. 2002; 250(4):579-590.

[125] Hong T, Chang TN. *Control of nonlinear piezoelectric stack using adaptive dither*. Proceedings of the 1995 American Control Conference. 1995; 1:76-80.

[126] Chen JS, Dwang IC. *A Ballscrew drive mechanism with piezo-electric nut for preload and motion control*. International Journal of Machine Tools and Manufacture. 2000; 40(4):513-526.

[127] Syamsul H, Oiwa T, Tanaka T, Asama J. *Positioning error improvement based on ultrasonic oscillation for a linear motion rolling bearing during sinusoidal motion*. Precision Engineering. 2014; 38(3):617-627.

[128] Tanaka T, Oiwa T, Syamsul H. *Positioning behavior resulting from the application of ultrasonic oscillation to a linear motion ball bearing during step motion*. Precision Engineering. 2017; 51:362-372.

[129] Yang S, Tomizuka M. *Adaptive pulse width control for precise positioning under influence of stiction and coulomb friction*. Proceedings of the 1987 American Control Conference. 1987; 188-193.

[130] Dong X, Zhang X, Okwudire CE. *A novel approach for reducing the settling time of roller bearing nanopositioning stages using high frequency vibration*. 30th Annual Meeting of American Society for Precision Engineering. 2015.

[131] Byl MF, Ludwick SJ, Trumper DL. *A loop shaping perspective for tuning controllers with adaptive feedforward cancellation*. Precision Engineering. 2005; 29(1):27-40.

[132] Francis BA, Wonham WM. *The internal model principle of control theory*. Automatica. 1976; 12(5):457-465.

[133] Physik Instrumente (PI). *Properties of piezo actuators*. (https://www.piceramic.com/en/piezo-technology/properties-piezo-actuators.html; accessed on Dec 1st, 2019)

[134] Shigley JE. *Shigley's mechanical engineering design*. Tata McGraw-Hill Education. 2011.

[135] Marin J. *Mechanical behavior of engineering materials*. Prentice-Hall. 1962.

[136] Bryan JB. *The Abbe principle revisited: an updated interpretation*. Precision Engineering. 1979; 1(3):129-132.

[137] Leang KK, Devasia S. *Feedback-linearized inverse feedforward for creep, hysteresis, and vibration compensation in AFM piezoactuators*. IEEE Transactions on Control Systems Technology. 2007; 15(5):927-935.

[138] Piatkowski T. *Dahl and LuGre dynamic friction models—the analysis of selected properties*. Mechanism and Machine Theory. 2014; 73:91-100.

[139] Hensen RH, van de Molengraft MJ, Steinbuch M. *Frequency domain identification of dynamic friction model parameters*. IEEE Transactions on Control Systems Technology. 2002; 10(2):191-196.

[140] Saab SS. *On the P-type learning control*. IEEE Transactions on Automatic Control. 1994; 39(11): 2298-2302.

[141] Kang D, Dong X, Kim H, Park P, Chinedum CE. *Friction isolated rotary system for high-precision roll-to-roll manufacturing*. 34th Annual Meeting of American Society for Precision Engineering. 2019.

[142] Wang J, Dong X, Barry O, Okwudire CE. *Dynamical analysis of friction induced vibration in a precision motion stage with a friction isolator*. arXiv preprint. 2019.

[143] Umeno T, Hori Y. *Robust speed control of DC servomotors using modern two degrees-of-freedom controller design*. IEEE Transactions on Industrial Electronics. 1991; 38(5):363-368.

[144] Kempf CJ, Kobayashi S. *Disturbance observer and feedforward design for a high-speed direct-drive positioning table*. IEEE Transactions on Control Systems Technology. 1999; 7(5):513-526.

[145] Schrijver E, Van Dijk J. *Disturbance observers for rigid mechanical systems: equivalence, stability, and design*. Journal of Dynamics System, Measurement, and Control. 2002; 124(4):539-548.

[146] Søndergaard RR, Hösel M, Krebs FC. *Roll-to-Roll fabrication of large area functional organic materials*. Journal of Polymer Science Part B: Polymer Physics. 2013; 51(1):16-34.

[147] Choi YM, Lee SH, Jo J. *High-precision slot-die coating machine for thin films of flexible display*. Journal of the Korean Society for Precision Engineering. 2014; 31(6):491-495.

[148] Kim H, Lee E, Choi YM, Kwon S, Lee S, Jo J, Lee TM, Kang D. *Development of a precision reverse offset printing system*. Review of Scientific Instruments. 2016; 87(1):015102.

[149] Bascetta L, Rocco P, Magnani G. *Force ripple compensation in linear motors based on closed-loop position-dependent identification*. IEEE/ASME Transactions on Mechatronics. 2009; 15(3):349-359.

[150] Kim K, Ahn D, Gweon D. *Optimal design of a 1-rotational DOF flexure joint for a 3-DOF H-type stage*. Mechatronics. 2012; 22(1):24-32.

[151] Kang D, Gweon D. *Analysis and design of a cartwheel-type flexure hinge*. Precision Engineering. 2013; 37(1):33-43.